



Electrical interactions in the HL-1 cardiomyocyte culture: An experimental and computational study

Author:

Bradd, Adrian

Publication Date:

2014

DOI:

<https://doi.org/10.26190/unsworks/18235>

License:

<https://creativecommons.org/licenses/by-nc-nd/3.0/au/>

Link to license to see what you are allowed to do with this resource.

Downloaded from <http://hdl.handle.net/1959.4/54551> in <https://unsworks.unsw.edu.au> on 2024-04-30



UNIVERSITY OF NEW SOUTH WALES

**Electrical interactions in the
HL-1 cardiomyocyte culture: An
experimental and computational
study**

by

Adrian Bradd

A thesis submitted in partial fulfillment for the
degree of Master of Biomedical Engineering

in the

Faculty of Engineering

Graduate School of Biomedical Engineering

April 2014

“The progressive development of man is vitally dependent on invention. It is the most important product of his creative brain. Its ultimate purpose is the complete mastery of mind over the material world, the harnessing of the forces of nature to human needs. This is the difficult task of the inventor who is often misunderstood and unrewarded. But he finds ample compensation in the pleasing exercises of his powers and in the knowledge of being one of that exceptionally privileged class without whom the race would have long ago perished in the bitter struggle against pitiless elements. Speaking for myself, I have already had more than my full measure of this exquisite enjoyment; so much, that for many years my life was little short of continuous rapture.”

Nikola Tesla

‘My Inventions: The Autobiography of Nikola Tesla’

Abstract

A simplified computational model of mouse atrial cardiomyocyte electrical activity was developed, based on the HL-1 cardiomyocyte cell line. HL-1 myocytes were characterised electrically and optically: the emission spectra of di-4-ANEPPS in HL-1 cultures, the cell type and distribution, and the optical-electrical equivalence of the potentiometric probe were all examined. Two major cell types were determined: pacemaking and non-pacemaking, with a distribution of 70%/30% respectively. Optical mapping of the HL-1 monolayer revealed linear wavefronts and re-entrant rotor activity. Rotors were shown to be the dominant source of spontaneous activity in the HL-1 cultures.

To reproduce experimentally observed electrical behaviour, a three-current generic ionic model was employed. Sharp electrode recordings of single cells were used to fit model parameters using a custom optimisation routine. An electrical cellular network model was created to replicate electrical interactions in the HL-1 monolayer. The action potential waveshape and conduction velocity of the network model were optimised to accurately reproduce experimental data. The model was able to faithfully reproduce linear wave fronts and re-entrant rotor activity seen in the HL-1 monolayer. The radius-angle rotor relationship of the model was within one standard deviation of that observed in the HL-1 monolayer.

Acknowledgements

First, I would like to begin by thanking my advisors, Professor Nigel Lovell and Associate Professor Socrates Dokos, for their insight and assistance throughout the project. I truly appreciate all your efforts and patience. It was a tortuous journey for certain, but I have learnt more during its course than I could have imagined at the outset. Thanks also go to Dr. Patsie Polly for the HL-1 cells and hearty discussions.

Second, I would like to thank my family for their support. Although Mum was aghast at my decision to leave employment in industry to move into research, and Anela is still hoping I will go back and make decent money. Further complicating matters, at one time Mum was under the impression that my work involved jabbing raspberries with electrodes. Alas, I love them all the same.

Third, I thank my friends and colleagues: James D. for putting up with my absence, Ernesto L. for the dinners, Chris K. for the random messages, Khoon Slim for the insightful conversations, Sally T. for not infecting my cells, Tianruo G. for subjecting me to the pain that is optimisation, Amr A.A. for his knowledge and patience, Khalid and Siwei for their neighbourly banter, Sinisa's words of wisdom, CG's comic relief, David T.'s conversations on all things science and engineering, James V.'s news reports, Ryan P.'s can-do attitude and talks about his as-yet unreleased autobiography, Steve P.'s knowledge of all things relating to the gym, Depanky's laughter and ability to organise events and turn up on time, Romana's patience and cell culture know-how, Liyuan and Jane's forums on culture coating protocols, Aaron G. for being a Kiwi, Brooke F. for being a good kid, and Ryan F. for proving that not all honour students are hopeless.

Last, I want to thank my partner Anela for her patience and love. I am not certain how you put up with me, but you do and for that I am grateful.

Adrian Bradd.

Contents

Abstract	ii
Acknowledgements	iii
List of Figures	vii
List of Tables	ix
Acronyms	x
1 Introduction	1
1.1 Background	1
1.2 Aims	3
1.3 Outline	4
2 Physiological and modelling principles	6
2.1 Gross structure of the heart	6
2.1.1 Cardiac electrical activity	7
2.1.2 Electrotonic interactions	9
2.2 Traditional electrophysiological recording	11
2.3 Optical techniques	13
2.3.1 Voltage sensitive dyes	13
2.4 The HL-1 cell line	16
2.5 Imaging	17
2.5.1 Fluorescent imaging	17
2.5.2 Microscopes	18
2.5.3 Light based microscopy	18
2.5.4 Fluorescent microscopy	19
2.6 Computational modelling of electrophysiology	22
2.6.1 A generic ionic model	23
2.6.2 Cable and network models	25
3 Existing single-cell models of cardiac electrical activity	28

3.1	Simplified computational models	28
3.1.1	FitzHugh-Nagumo based models	28
3.1.2	Fenton-Karma based models	31
3.1.3	A simplified generic ionic model	34
3.2	Biophysically-accurate models of mouse myocytes	37
3.3	Optimisation of a computational model of mouse cardiac electrical activity	38
4	Methods	40
4.1	HL-1 culture	40
4.1.1	Experimental preparation	41
4.2	Experimental setup	42
4.2.1	Correlating electrical and optical activity	44
4.3	Spectral analysis	45
4.4	Post-processing of experimental data	45
4.5	Optimisation of the cardiomyocyte action potential	47
4.5.1	Initialisation	47
4.5.2	Minimum searching and curvilinear gradient optimisation	51
4.5.3	Weighted residuals	51
4.5.4	Parameter randomisation	51
4.5.5	Condition of termination	51
4.6	Network modelling	52
4.6.1	Optimisation of tissue-based model	54
4.7	Programming	56
5	HL-1 monolayer results	57
5.1	HL-1 cell line characteristics	57
5.2	Optical analysis	58
5.2.1	Optical properties of di-4-ANEPPS in HL-1 cells	58
5.2.2	Optical-electrical equivalence of di-4-ANEPPS	60
5.3	Electrical action potential data	61
5.3.1	Cell types in the HL-1 cell line	61
5.3.2	Cell distribution in the HL-1 cell line	62
5.4	Optical action potential propagation	63
5.4.1	HL-1 OAP characteristics	65
5.4.2	Optically recorded wavefronts	65
5.4.3	Optically recorded rotors in HL-1 monolayers	65
5.5	Discussion	73
5.5.1	Analysis of the emission spectra	73
5.5.2	Limitations of the optical recording system	75
5.5.3	Cell types and distributions in the HL-1 cell line	76
5.5.4	Optical imaging of electrical activity	77
5.6	Conclusion	80
6	Modelling electrical activity in the HL-1 cell line	81

6.1	Single cell modelling	81
6.1.1	Single cell AP fitting	81
6.1.2	The generic ionic model structure	83
6.1.3	The optimisation routine	83
6.1.4	Single cell model parameters	84
6.2	Network model of the HL-1 monolayer	86
6.2.1	Tissue-based optimisation	86
6.2.2	Self-maintaining AP rotors	91
6.3	Discussion	98
6.3.1	Cell selection for modelling	98
6.3.2	Single cell and tissue-based modelling	99
6.3.3	Radius-angle relationship	100
6.3.4	Waveshape characteristics of experimental and modelled activation	103
6.3.5	Justification for the generic ionic model	103
6.3.6	An analysis of the rotor	104
6.4	Conclusion	104
7	Conclusions and future work	105
7.1	Concluding remarks	105
7.2	Future work	107
	Appendices	108
A	On the culture of the HL-1 cell line	109
A.1	Introduction	109
A.2	Reagents	109
A.3	Culture	113
A.4	End of life	116
	Bibliography	119

List of Figures

2.1	Sinoatrial node and ventricular action potentials	8
2.2	Types of electrodes used in electrophysiology	12
2.3	ON-OFF fluorescence mechanism	14
2.4	Redistribution fluorescence mechanism	15
2.5	Reorientation fluorescence mechanism	15
2.6	Electrochromic fluorescence mechanism	16
2.7	Diagram of molecular photon excitation	18
2.8	Basis for the generic ionic model	24
2.9	The transition from a single cell to a network model	27
4.1	Experimental optical setup	44
4.2	Flow chart for non-linear least squares optimisation.	49
4.3	Simplified cable formulation for computational model	53
4.4	Two-dimensional cellular interconnections in model	54
4.5	The monodomain representation of the network model	55
5.1	Emission spectra of di-4-ANEPPS in HL-1 cells	59
5.2	Brightfield and fluorescent image of impaled cell.	60
5.3	Optical and electrical AP comparison	61
5.4	Cell types in HL-1 cultures.	63
5.5	Spatial averaging illustration.	64
5.6	A linear propagation OAP wavefront	66
5.7	Optical mapping of an arrhythmia-like rotor in a HL-1 culture . . .	67
5.8	Contour map of arrhythmia-like rotor system in HL-1 monolayer . .	68
5.9	OAPs at the rotor origin	69
5.10	OAPs in the wings of a rotor	70
5.11	Spiral activation wavefront overlaid on optical rotor	71
5.12	Radius-angle relationship in optically mapped rotors	72
6.1	Membrane potential and ionic currents of the single cell generic ionic model	82
6.2	Membrane potential and ionic currents in the network model	90
6.3	Linear wavefront propagation	91
6.4	Underlying APs of planar propagating wavefront	92
6.5	An electrical rotor in the network model	93
6.6	Contour map of the rotor system given in Figure 6.5	94

6.7	A comparison between modelled (rotor) and recorded electrical activity	95
6.8	Action potentials at the core of the simulated rotor in the network model	96
6.9	Action potentials in the exterior of the rotor in the network model	97
6.10	Comparing ionic currents in the single cell and network models	101
6.11	Comparison of rotor radius-angle relationship between simulation and experiment.	102
A.1	Healthy HL-1 cells	117
A.2	Unhealthy HL-1 cells	117

List of Tables

3.1	Complexity of simplified models	35
3.2	The development of simplified/generic computational models	36
4.1	Upper and lower limits for model parameters	50
5.1	Linear wavefront 50% wave-width	64
5.2	Spiral 50% wave-width	65
5.3	Table of beat rate in the literature	76
6.1	Single cell optimised parameters	85
6.2	Initial values for parameter-optimised single cell model	86
6.3	Network model parameters	88
6.4	Initial values for parameter-optimised tissue-based model	89
6.5	Conductivity and scale values for MATLAB-based 2D finite difference approximation	89
6.6	Comparison between single cell and tissue-based model ionic currents	100
6.7	Half-amplitude OAP width comparison	102
A.1	Reagents for HL-1 culture	110
A.2	Supplemented Claycomb's media	111
A.3	Formulation for wash medium	111

Acronyms

Ag/AgCl silver/silver chloride

AP action potential

APD action potential duration

AVN atrioventricular node

BPS beats per second

CCD charge-coupled device

CMOS complimentary metal-oxide-semiconductor

CV conduction velocity

DIC differential interference contrast

DMSO dimethyl-sulfoxide

EDTA Ethylenediaminetetraacetic acid

FBS fetal bovine serum

FHN FitzHugh-Nagumo

FPS frames per second

GFP green fluorescent protein

HH Hodgkin-Huxley

KCl potassium chloride

LED light emitting diode

OAP optical action potential

ODE ordinary differential equation

PBS phosphate-buffered saline

PMT photomultiplier tube

RMS root mean square

SAN sinoatrial node

Dedicated to my grandmother...
For a life of love and care...

Chapter 1

Introduction

1.1 Background

Electrical activity underlying the function and malfunction of the mammalian heart has been the topic of much investigation. Numerous studies of cardiac electrophysiology have uncovered a great deal of information on the basic physiology of the mammalian heart, providing insights into the source of various pathophysiological conditions such as arrhythmias (Nattel, 2002, Pandit and Jalife, 2013, Smaill et al., 2013).

Traditional electrophysiological experiments have been limited to single cell or low spatial resolution multicellular investigations. Recent advances have led to the development of potentiometric dyes capable of high spatial resolution tracking of changes in membrane potential, establishing an entirely new domain under which examination of the electrophysiology of the heart can be performed (Rosenbaum and Jalife, 2001, Shenasa et al., 2009, Zecevic and Canepari, 2010).

With the advent of computers, researchers were given the ability to develop complex computational models of biological systems. The first biophysically-accurate model of excitable tissues was the Hodgkin-Huxley (HH) model of the squid giant axon (Hodgkin and Huxley, 1952). The first ionic model of cardiac electrical activity was the Noble (1962) model which was a modified HH model of Purkinje cells.

Since the Noble model, dozens of computational models of electrical activity in the heart have been formulated. As computers have continued to grow more powerful, they have enabled more complex systems to be modelled. This led to the development of complex biophysically-accurate models of cardiac electrical activity. Modelling has now become an integral tool for electrophysiological studies, and in continued combination with experimental data has successfully provided insights into underlying mechanisms of the cardiac electrical activity (Hunter et al., 2003, Lines and Nielsen, 2007, Nattel and Li, 2000).

Existing computational models of cardiac electrical activity have mostly focused on improving the accuracy of electrophysiological simulation using biophysically-accurate models of the cardiac action potential (AP). Even with the continued improvement of computational processing power, biophysically-accurate models remain computationally expensive to simulate. In this thesis, we attempt to address this issue by employing a simplified generic ionic model which is computationally simple, but extendible via the arbitrary addition of membrane currents to enable the reproduction of complex datasets (Al Abed et al., 2011, 2013, Guo et al., 2010, 2011, 2013). The complexity of the generic ionic model lies between that of a simple phenomenological model, such as the FitzHugh-Nagumo (FHN) model, and a biophysically accurate model, such as the Courtemanche et al. (1998) model of human atrial myocytes.

In this thesis we present a simplified ionic model of electrical activity in the mouse atrial cardiomyocyte. To the best of our knowledge, there has not yet been a computational model specific to the mouse atrial cardiomyocyte. For experimentation we used the HL-1 cell line, a derivative of the mouse AT-1 subcutaneous tumour that can be serially passaged and retains a contractile phenotype (Claycomb et al., 1998). We employ techniques, such as sharp glass microelectrode recording and optical mapping of tissue-level electrical activity with potentiometric dyes, revealing useful information on electrical activity at both the single cell and the tissue scale. The result is a multi-scale characterisation of the electrical activity of HL-1 atrial cells connected in an active syncytium.

The computational model is based on a three-current generic ionic model which uses HH dynamics to describe ionic behaviour (Guo et al., 2013). The model was fitted to experimental data under two scenarios: a single cell formulation and a network configuration. In both scenarios, we optimised model parameters to fit characteristics found experimentally. AP waveshape was an important indicator of the accuracy of the model when compared to experimental data. The network model simulated the interconnected nature of cardiac myocytes in a functional syncytium, to enable the study of electrotonic interactions in physiological and pathophysiological conditions.

The work outlined in this thesis represents the basis for future studies of electrical interactions of cardiac cells connected in a syncytium. The HL-1 cell line, formed from mouse adult cardiomyocytes, enables strict control over culture conditions, such as patterned cultures (Claycomb et al., 1998). In combination with the robustness of the generic ionic model, this thesis presents a tool to further investigate electrical mechanisms underlying physiological and pathophysiological conditions in the mammalian heart.

1.2 Aims

The primary aim of this thesis is to formulate a simplified computational model of mouse atrial cardiomyocytes in isolation and connected monolayers that can faithfully reproduce electrical activity at the single cell and tissue scale. This will necessitate us to detail the relevant characteristics of the potentiometric dye, di-4-ANEPPS, as well as the HL-1 cell line. Finally, parameters of the computational ionic models will be optimised to enable accurate fitting of our experimental data. The specific objectives of this thesis are as follows:

1. Optically characterise di-4-ANEPPS in HL-1 cells.
2. Electrically characterise the AP waveshapes of the HL-1 cell line.

3. Optically record whole-tissue electrical activity in the HL-1 cell line.
4. Formulate and optimise a single-cell generic ionic model to fit AP waveshape recorded in HL-1 cells.
5. Implement the generic ionic model in a network architecture, optimising parameters to fit AP waveshape and conduction velocity.
6. Simulate rotor activity in the network model, and compare with recorded rotors in HL-1 atrial cardiomyocyte cultures.

1.3 Outline

An outline of each chapter in the thesis is as follows:

Chapter 2 provides a general background for cardiac electrophysiology, membrane sensitive dyes, the HL-1 cell line, fluorescent imaging and computational modelling of electrophysiological phenomena.

Chapter 3 reviews existing models of excitable cells, with a focus on the mammalian cardiomyocyte. We survey the progression of generic and simplified models of excitable media and mammalian cardiac preparations and investigate mouse specific biophysically-accurate ionic models.

Chapter 4 presents the methodology for the techniques used in this thesis. This chapter provides detailed information about our cell culture, electrical and optical recordings, and computational modelling.

Chapter 5 presents the experimental results. Here we characterise both our potentiometric dye, di-4-ANEPPS, and the HL-1 culture. Further, we optically record from several HL-1 preparations to visualise electrical activity on the tissue-scale. Finally, we analyse our findings and discuss their relevance with respect to formulation of a computational model. This chapter establishes fundamental properties of the cell culture and optical imaging system required to formulate our computational model.

Chapter 6 presents the simplified mouse atrial model. We fit our electrophysiological data to both a single cell and network model and successfully replicate single cell and tissue-scale electrical activity. Lastly, we discuss the limitations and relevance of the model as a platform for electrophysiological investigations of the mouse atrial cardiomyocyte.

Chapter 7 concludes the thesis summarising the work completed and a proposal for future work.

Appendix A presents detailed information regarding culture of the HL-1 cell line.

Chapter 2

Physiological and modelling principles

2.1 Gross structure of the heart

The heart is a muscular organ that circulates blood around the body by contracting, delivering oxygen and nutrients to various tissues, and removing metabolic waste products. It consists of four chambers: the right and left atria, and the right and left ventricles. The heart initiates and conducts electrical signals, known as action potentials, autorhythmically to stimulate contraction.

Blood returning from the systemic circulation enters the right atrium via the superior and inferior venae cavae. The blood is then pumped by the right atrium through the tricuspid valve into the right ventricle. From there blood flows through the pulmonary valve, via the pulmonary arteries, into the lungs for oxygenation. Blood returns to the left atrium via the pulmonary veins. Blood is forced into the left ventricle through the mitral valve and is finally pumped through the aortic valve into the aorta on its way to all systemic organs in the body (Netter and Colacino, 1989).

2.1.1 Cardiac electrical activity

Spontaneous cardiac electrical activity derives from a specialised piece of tissue located in the right atrium, between the superior and inferior venae cavae, known as the sinoatrial node (SAN). From the SAN the AP propagates through the left and right atria. APs from the right atrium arrive at another specialised piece of tissue, known as the atrioventricular node (AVN), lying at the junction between the right atrial appendage and the interventricular septum. The AVN serves as the sole connection between the atria and the ventricles. Beyond the AVN lies the Bundle of His which connects to a group of specialised fibres, the bundle branches and Purkinje fibres, that allow rapid conduction down the interventricular septum and into the right and left ventricular walls (Sperelakis et al., 2000).

The various landmarks in the heart exhibit APs with varying characteristics. These are typically separated into the different cell types found in the heart. Further, each AP can be divided into phases, illustrated in Figure 2.1 for typical SAN and ventricular APs. Phase 4 denotes the resting membrane potential of the cardiomyocyte. Typically in cardiac cells, the resting membrane potential will be stable, as represented in Figure 2.1b). This stable level is mainly maintained by ion channel pumps and exchangers i_{Na-Ca} and i_{Na-K} and an outward potassium current i_{K1} . A select group of specialised pacemaker cells exhibit unstable resting potentials such as those found in the SAN (Figure 2.1a)). This results in a slow phase 4 depolarisation to a membrane voltage of approximately -40 mV which is facilitated by inward calcium currents, $i_{Ca(T)}$ and $i_{Ca(L)}$, and the hyperpolarisation-activated inward sodium-potassium current known as the ‘funny current’, i_f (Carmeliet and Vereecke, 2002).

Phase 0 denotes the rapid depolarisation phase which signifies electrical activation of the cell. This phase is typically associated with the opening of Na^+ channels, producing inward i_{Na} . Once again, the exception is pacemaking cells which exhibit a shallower slope for the rapid depolarisation phase dictated by L-type calcium channels, eliciting $i_{Ca(L)}$ (Carmeliet and Vereecke, 2002).

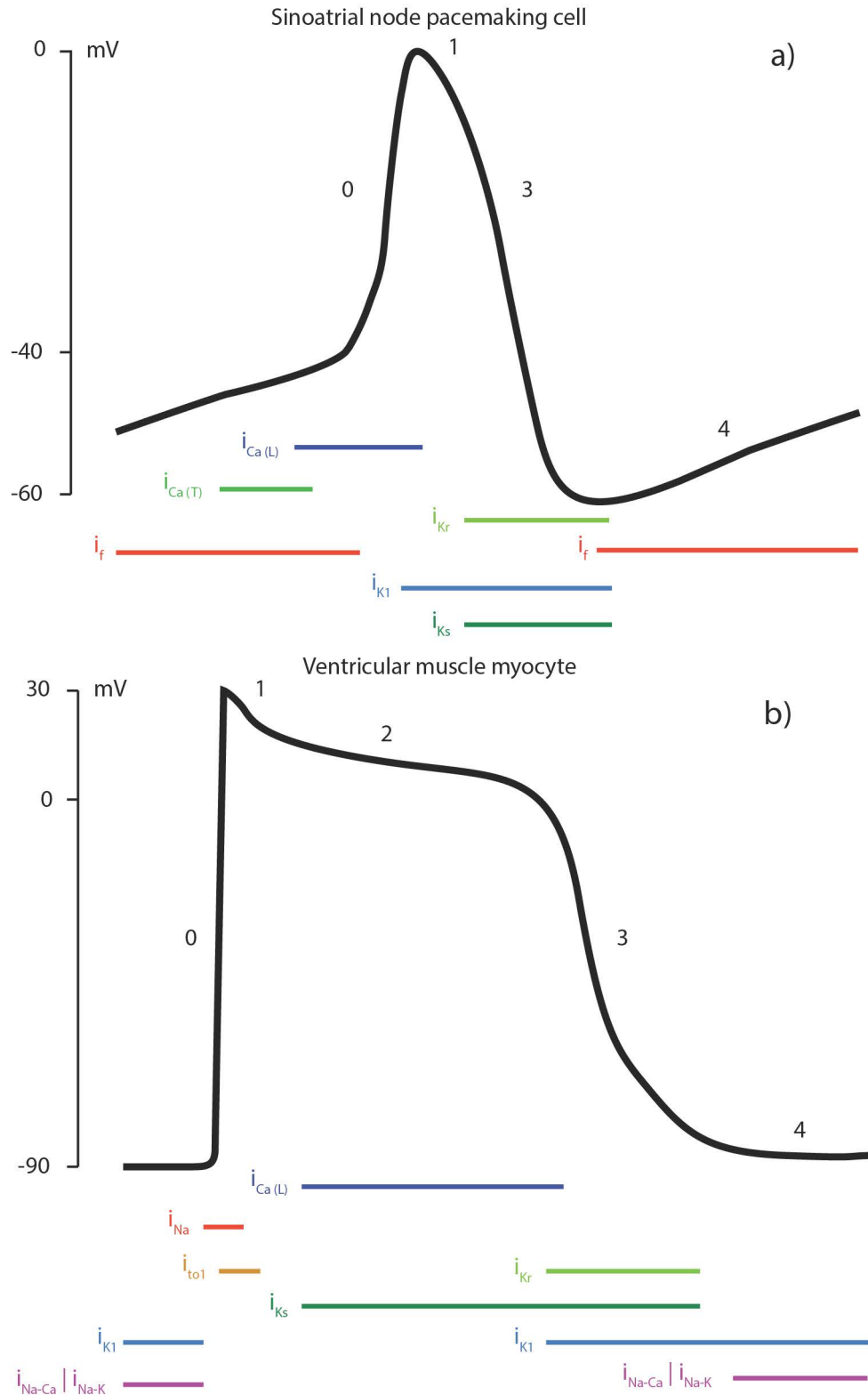


FIGURE 2.1: Sinoatrial node and ventricular action potentials with underlying AP currents responsible for membrane potential activity. a) presents the AP of the SAN with major currents. b) illustrates the AP of the ventricular cardiomyocyte. The currents include: the hyperpolarisation-activated inward current (i_f), the T-Type Ca^{2+} current ($i_{Ca(T)}$), the L-Type Ca^{2+} current ($i_{Ca(L)}$), the rapid delayed rectifier K^+ current (i_{Kr}), the inwardly rectifying K^+ current (i_{K1}), the slow delayed rectifier K^+ current (i_{Ks}), the inward fast Na^+ current (i_{Na}), the transient outward K^+ current (i_{to1}), the Na-Ca exchanger and Na-K pump.

Phase 1 represents the initial rapid repolarisation resulting from inactivation of Na^+ channels and the contribution of K^+ and Cl^- outward currents, mainly the transient outward K^+ current (i_{to1}), causing a net outward current. In pacemaker cells, the initial rapid repolarisation is rounded due to the outward K^+ current, i_K (Burns, 2013, Carmeliet and Vereecke, 2002).

Phase 2 is the ‘plateau’ phase, a region where the action potential is held stable for the majority of the AP duration. The plateau is sustained by the combination of inward L-type calcium $i_{Ca(L)}$ and outward slow rectified K^+ membrane current (i_{Ks}). Pacemaker cells do not exhibit a plateau phase (Carmeliet and Vereecke, 2002).

Phase 3 refers to the repolarisation phase in which the membrane potential returns to its resting value. In most cardiac cell types, it is the result of the continued contribution of the slow delayed rectifier K^+ current (i_{Ks}) as well as the rapid delayed rectifier current (i_{Kr}) and inward rectified potassium current (i_{K1}) (Carmeliet and Vereecke, 2002).

There are a number of pacemaking cell types in the heart, chiefly: the SAN, the AVN, the Bundle of His and the Purkinje fibres. Each of these have their own intrinsic pacemaking rate, but most cells do not self-activate in-situ, as they are activated by the SAN before their natural spontaneous activation occurs. The SAN elicits the fastest pacing rate followed by the AVN. As a result, activation of the SAN entrains the rest of the heart. Should the SAN fail, the AV node will take over as the primary pacemaker for the heart (Burns, 2013).

2.1.2 Electrotonic interactions

The structures underlying intercellular electrical conduction in cardiac networks are known as gap junctions. Gap junctions allow for the passage of ions between neighbouring cells through a region of interconnection known as the intercalated disc. They enable the rapid transmission of APs through the cardiac syncytium (Dhein, 2006).

Electrotonic interactions are a well known property of cardiomyocytes forming a functional syncytia. Electrotonic loading stems from gap-junction interconnections between cardiac cells and can result in sink effects where inactive cardiomyocytes draw current from activating cells. This also leads to the concept of the length or space constant, that is the distance at which sub-threshold perturbations in membrane potential will extend to in a syncytium. Traditional electrophysiology is limited to monitoring a few cells at a given time. As a result, many studies have focused on single cell behaviour of isolated cardiomyocytes. Potentiometric dyes and wide-field optical mapping enable a closer discrimination of the effect electrotonic coupling has on electrical activity in cardiac tissue (DeMello, 1977, Jalife et al., 2011).

Another property of excitable cells is the refractory period, a time in which the cell has limited capabilities to evoke APs. The refractory period in cardiomyocytes consists of:

- the absolute refractory period, here an AP cannot be initiated in the cell,
- and the relative refractory period, where APs are inhibited but not completely blocked.

The absolute refractory period precedes the relative refractory period. The refractory period and electrotonic interactions play a major role in the in normal and abnormal physiological function Podrid and Kowey (2001). Refractoriness has been directly linked to re-entrant spiral behaviour in cardiac tissue (Qu et al., 2000, Weiss et al., 2000, Xie et al., 2002). Further, sites such as the SAN introduce a paradoxical electrotonic behaviour. The smaller pacemaking site of the SAN is surrounded by the more negative resting membrane potential of the atria, but the atria does not hyperpolarise or suppress autorhythmic activation of the SAN. This behaviour suggests that electrotonic interactions and gap junction distributions play a vital role in nominal cardiac function and should be treated as such during investigations (Boyett et al., 2006, van Rijen et al., 2006).

Historically, experimental and computational studies of cardiac electrophysiology have focused on single cellular activity (Noble, 1984). With the advent of newer technology, such as optical imaging, researchers have begun to focus on the electrical interactions of cells at the tissue level. Studies have shown variations in electrophysiological behaviour between isolated and in-tact tissue (Elshrif and Cherry, 2014).

2.2 Traditional electrophysiological recording

Traditional electrophysiological recording uses electrodes such as: 1) solid conductors, like tungsten, in the shapes of discs or needles or on a printed circuit board or other structure; and 2) hollow glass electrodes filled with an electrolyte, such as potassium chloride (KCl), fed through a silver/silver chloride (Ag/AgCl) wire to the acquisition hardware (Sigg et al., 2010). Methods utilising solid conductors have found application in intracellular and extracellular recording and can take many forms. Two of the most popular are singular tip or ball electrodes and multi-electrode arrays (Windhorst and Johansson, 1999). Glass electrode methods can be loosely classed as either sharp or patch electrodes. Sharp electrodes have found popularity in intracellular studies, since their pointed tip allows them to penetrate the membrane of a cell with relative ease. Sharp electrodes have a large resistance in the range of 50 – 100M Ω , and must be filled with a highly conductive electrolyte solution, typically highly concentrated KCl. KCl is a popular choice with Ag/AgCl electrodes since it is through a non-polarising exchange of chloride ions that the electrode is able to detect changes in potential. Patch electrodes come in a variety of shapes and sizes and are able to measure intracellular, extracellular and ion channel activity. Patch electrodes have a blunt, relatively wide tip and are also filled with an electrolyte solution, but the type of solution is highly application specific (Windhorst and Johansson, 1999). For example, electrolyte solution for intracellular work is formulated to mimic intracellular conditions to ensure the integrity of the cell for the maximum amount of time (Sigg et al., 2010). An overview of the traditional methods is presented in Figure 2.2.

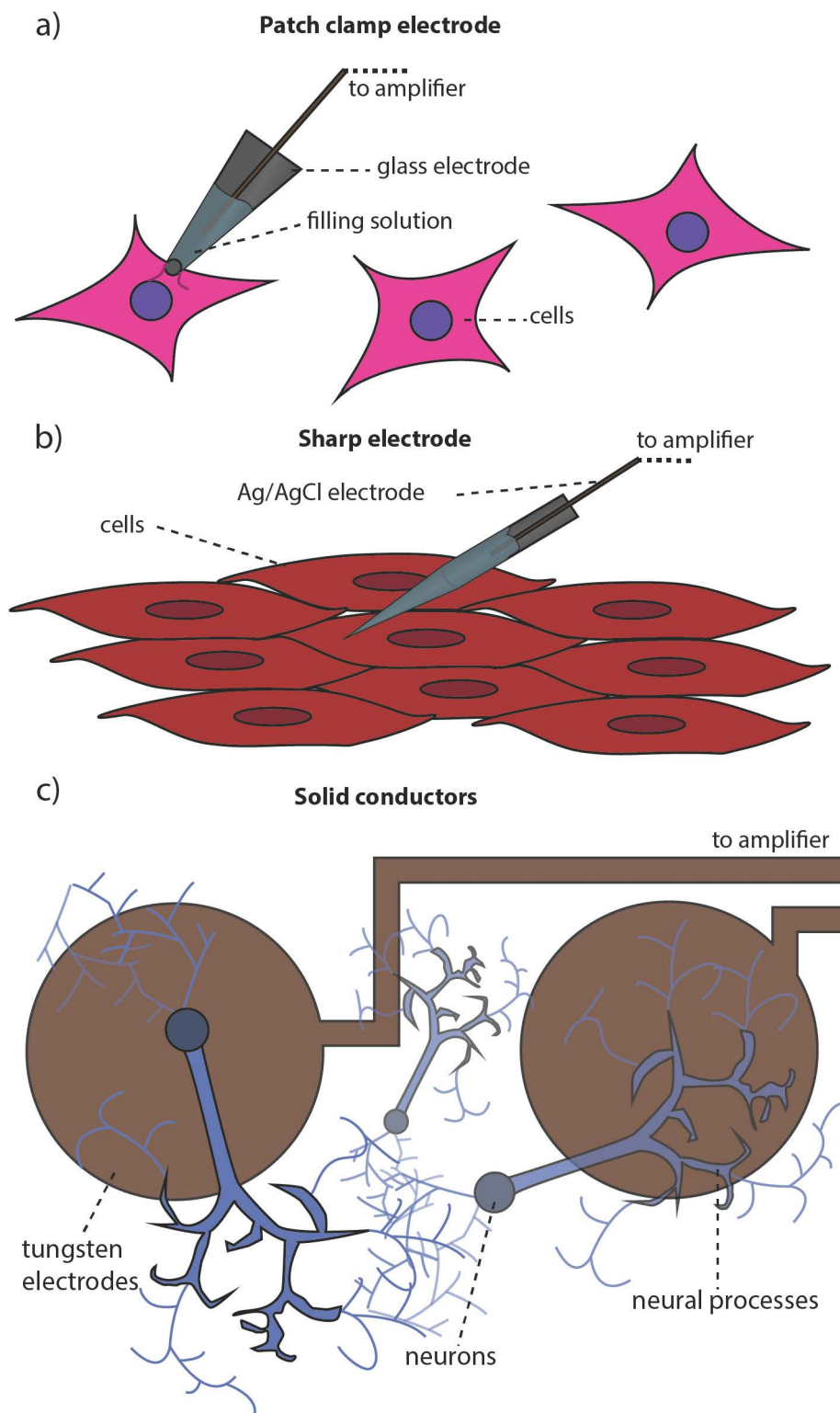


FIGURE 2.2: Various electrodes used in electrophysiology. a) presents a patch electrode attached to a cell. Patch electrodes can be used for intracellular and extracellular recordings. b) illustrates a sharp electrode that is impaling a single cell to recording intracellular activity. c) exhibits solid conductors used for extracellular recording of electrical activity.

2.3 Optical techniques

Recently, optical electrophysiological techniques have increased in popularity because of their ability to track electrical activity on a macro scale. There are indicator probes capable of monitoring any ion involved in the activity of excitable cells. One of the most popular indicators are the calcium specific probes, such as the Fura Red and Green BAPTA (1,2-bis(*o*-aminophenoxy)ethane-*N,N,N',N'*-tetraacetic acid) variants (Williams et al., 1999). More recently, probes known as the ANEP (aminonaphthylethylenylpyridinium) dyes, which are capable of sub-millisecond tracking of membrane potential, were developed by (Loew, 1996). The ANEP dyes were not the first to monitor membrane potentials in excitable cells but they are among the fastest, most sensitive (10% per 100mV) and commercially available. Of these, di-4-ANEPPS is one of the most robust ANEP dyes and is frequently used in cardiac optical imaging (Efimov et al., 2004). It is capable of sub-millisecond resolution and ratiometric excitation or emission recording. The ANEP dyes lodge in the outer leaflet of the plasma membrane and undergo changes in their emission profile with changes in membrane potential.

2.3.1 Voltage sensitive dyes

ON-OFF dyes

The ON-OFF mechanism relies on probes moving from the hydrophobic environment of the lipid bilayer to the aqueous environment surrounding the cell when exposed to the transmembrane electric field of the excitable cell (Figure 2.3). Fluorescence of the probes increases dramatically upon entering the lipid phase. Localization of the probes, that is whether the probe lies inside the membrane or in the extracellular solution, is affected by the membrane potential. The ON-OFF mechanism has a time constant on the order of seconds, and is therefore not used for visualisation of rapid electrical activity in excitable cells (Rosenbaum and Jalife, 2001).

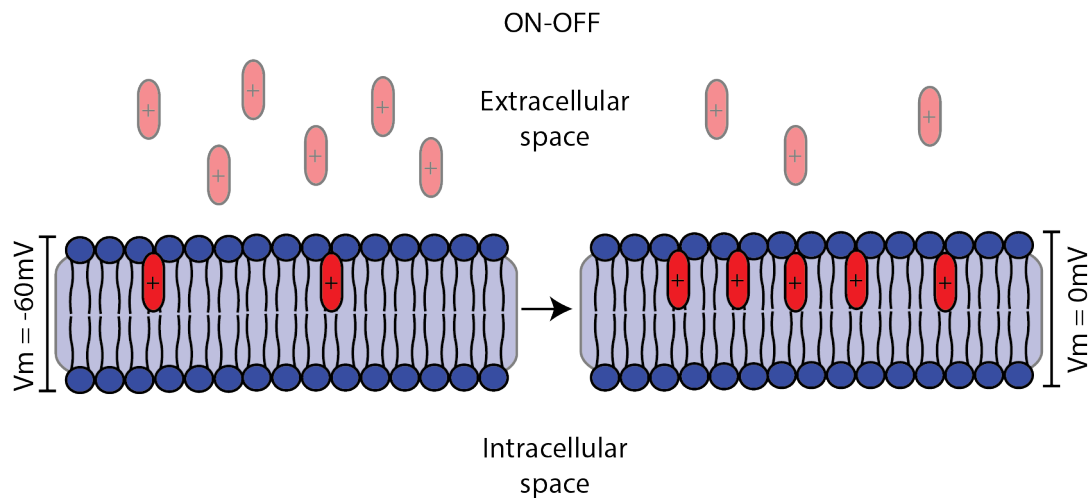


FIGURE 2.3: ON-OFF fluorophores increase their fluorescence on entering the lipid membrane. The left panel illustrates resting membrane potential levels (-60 mV), and the right panel shows depolarized levels (0 mV).

Redistribution

This mechanism results from the membrane dependant redistribution of membrane-permeant cations (Figure 2.4). Unlike the ON-OFF mechanism, the fluorescence of the probe does not change with localisation. As a result of its action, it cannot be used for tissue scale imaging of membrane potential changes, as there is no way to discriminate between intracellular and extracellular fluorescence. For example, if two or three cells lie within a single image pixel, it would be impossible to distinguish extracellular and intracellular concentrations of the dye for any of the cells, since the fluorescence intensity will not change upon crossing the membrane. Redistribution can be used in combination with aggregation methods, but the time course is still on the order of seconds, and is unsuitable for tracking action potentials of excitable cells (Rosenbaum and Jalife, 2001).

Reorientation

Probes utilising the reorientation mechanism will undergo physical rotation under the influence of a varying electric field (Figure 2.5). Fluorescence is dependent upon the probe's orientation with respect to the propagating light wave. In this

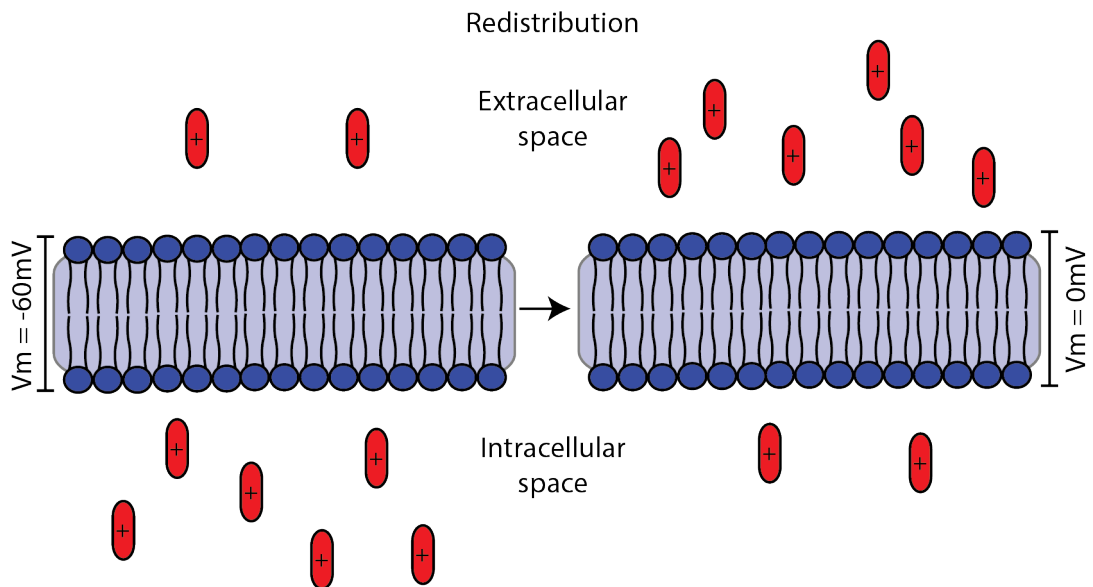


FIGURE 2.4: Redistribution relies on localisation of the fluorophore either in the extra- or intracellular space.

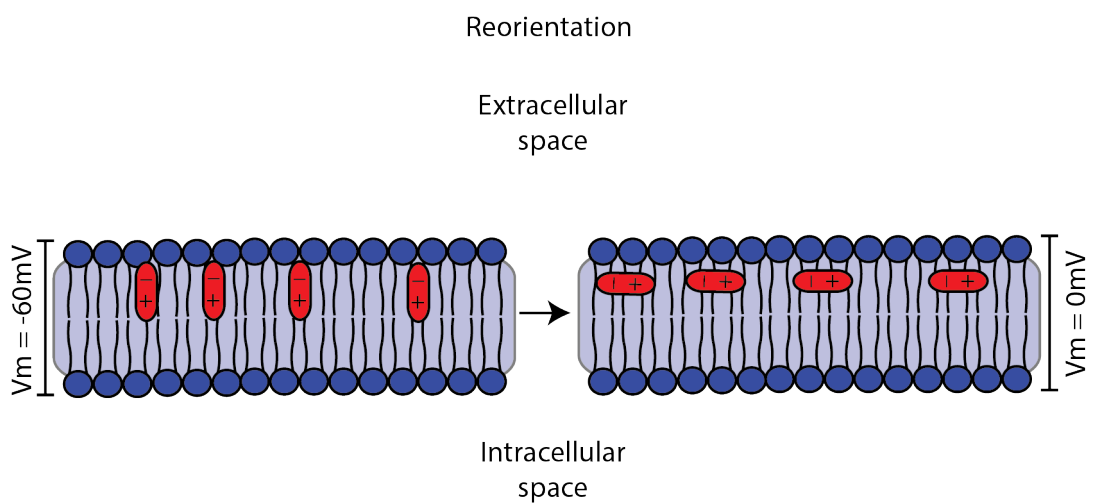


FIGURE 2.5: In the mechanism of Reorientation, the fluorophore changes its orientation with membrane potential.

way, the fluorescence is proportional to the membrane potential. Dyes using the reorientation mechanism are capable of sub-millisecond responses and can accurately track a cardiac AP, but exhibit low potential dependent fluorescence (Rosenbaum and Jalife, 2001).

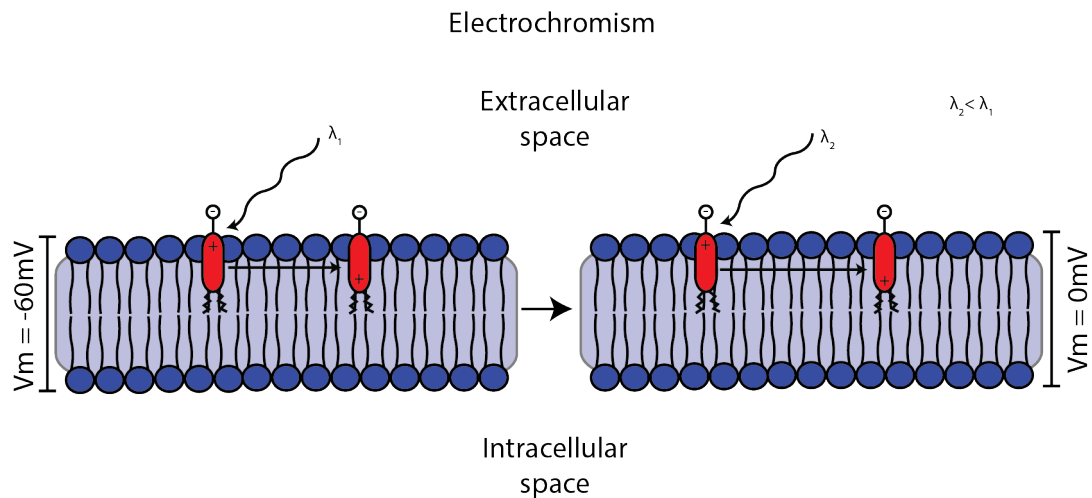


FIGURE 2.6: Electrochromism employs a charge-shift mechanism to alter fluorescence with membrane potential.

Electrochromism

Electrochromic dyes are the fastest of all potential sensitive dyes. Electrochromism utilises large charge redistribution in the electronic structure of the probe upon light based excitation of a fluorescent probe (Figure 2.6). The dyes contain a polar head with a non-polar tail to allow the molecular probe to enter the outer leaflet of the lipid membrane and orient itself perpendicular to the membrane, which is parallel to the electric field created by the ionic gradient of the cell. Changes in membrane potential assist or impede transitions of the fluorescent molecule into its excited state. These dyes are capable of sub-millisecond response resolution and are very suitable for visualising changes in membrane potential of excitable cells. Further, many of the electrochromic dyes, such as di-4-ANEPPS, are capable of ratiometric analysis through use of the emission and excitation spectra (Rosenbaum and Jalife, 2001). They are the major focus of the thesis.

2.4 The HL-1 cell line

The HL-1 cell line is derived from an AT-1 subcutaneous atrial tumour removed from a C57BL/6J laboratory mouse: the cells have adult cardiomyocyte morphological, biochemical and electrophysiological characteristics (Claycomb et al.,

1998). HL-1s can be serially passaged while maintaining their contractile phenotype, and have proven useful as a model cell for cardiac studies (White et al., 2004). This thesis is concerned with the electrophysiological characteristics of HL-1s but their similarity to adult cardiomyocytes in-situ exposes opportunities for further study. The HL-1 culture was found to contain two major cell types seen in atrial tissue, pacemaking and non-pacemaking myocytes (Sartiani et al., 2002). The pacemaking cells exhibit slow phase 4 depolarisation, typically seen in the SAN. HL-1 cells are spontaneously active both electrically and mechanically, with HL-1 pacemaking cells possessing an outward delayed rectifier current i_{K_r} as well as hyperpolarisation-activated "funny" current i_f . They exhibit maximum diastolic potentials of around -69 mV and spontaneous activation frequency of 1-5 Hz, all characteristics of mouse adult cardiomyocytes (Sartiani et al., 2002).

HL-1 cells can be cultured to confluence and form a monolayer of gap junction connected cardiomyocytes. They are a suitable model for both single-cell and multi-cellular studies of adult mouse cardiomyocytes. Unlike tissue extracted from an animal, HL-1 cultures do not have gross structural anomalies and can be maintained for extended periods with relative ease. Further, they can be serially passaged over months and years without the need to euthanase animals.

2.5 Imaging

2.5.1 Fluorescent imaging

Fluorescence is the emission of light by an object which has absorbed some form of electromagnetic radiation. Typically, the emitted radiation is of a longer wavelength (lower energy) than the absorbed radiation. Fluorescence is used in fluorescent microscopy to investigate specific properties of objects or substances. In the life sciences, fluorescence microscopy has a plethora of applications, from imaging cell nuclei to tracking membrane potentials of excitable cells (Cox, 2012).

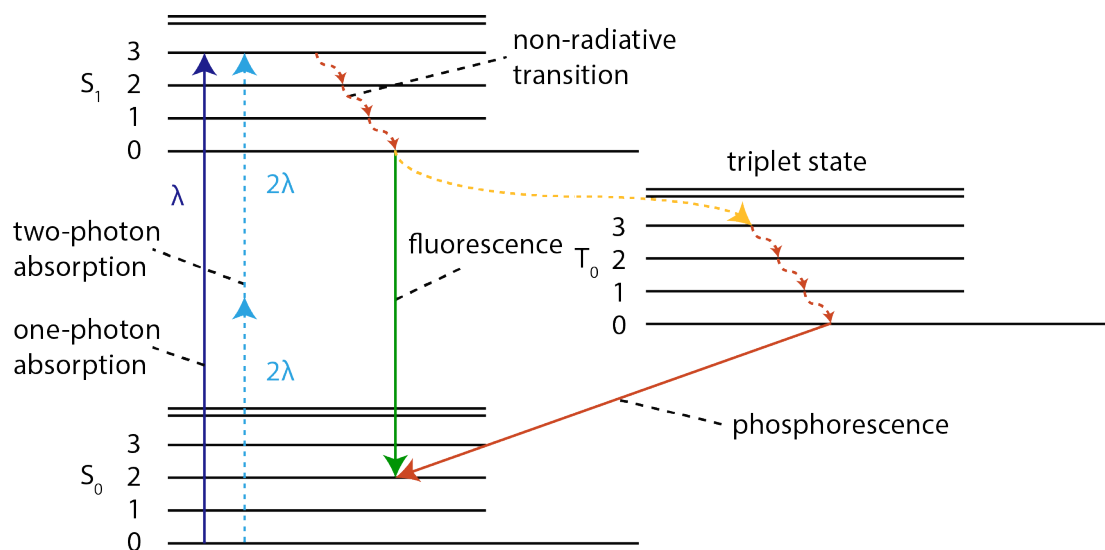


FIGURE 2.7: Jablonski diagram of fluorescence excitation and emission cycle.

The property of fluorescence is well-described with a Jablonski diagram (Figure 2.7). When a photon strikes a fluorescent molecule or structure, an orbital electron moves from the ground state, S_0 , to a higher quantum state S_1 . After a time, the electron begins to relax which can be expressed in a number of forms. Figure 2.7 illustrates relaxation by non-radiative transition (heat) and fluorescence, which occurs when the electron moves from the excited state, S_1 , to the ground state, S_0 , emitting a photon. Molecules can also shift from S_1 into a triplet state which leads to a further decay to the ground state (Lakowicz, 2007). Relaxation by fluorescent emission is the focus of this thesis.

2.5.2 Microscopes

Microscopes can be separated into one of two broad categories: light or electron based; and point scanning or whole sample illumination. Our concern is whole sample illumination with light based sources.

2.5.3 Light based microscopy

A standard optical microscope consists a source of illumination, a condenser to focus the light onto the sample, an objective to capture the transmitted/emitted

light, and finally a camera or oculars for visualisation. Scanning point microscopes require more hardware in the form of scanning mirrors and photomultiplier tubes.

Non-fluorescent visualisation of samples is accomplished usually in one of two ways: brightfield or contrast methods. Typically, these methods utilise halogen lamps but can also be applied using laser sources. Brightfield is the simplest illumination technique, relying on variations in absorption in the structure of the sample to provide contrast. The two most popular contrast methods are phase contrast and differential interference contrast (DIC). Contrast methods use small changes in phase of the illuminating light as it encounters structures in the sample, converting these into amplitude to better visualise the sample. Phase contrast and DIC each require modification of the light prior to or after contact with the sample, and so are more complex than bright field (Cox, 2012).

2.5.4 Fluorescent microscopy

Light based microscopy can be separated into two fields: wide field and scanning point. This thesis utilises wide-field microscopy, but we cover both methods for completeness.

Fluorescent imaging is accomplished by natural fluorescence, such as the green fluorescent protein (GFP), or by the introduction of a fluorescent probe, such as di-4-ANEPPS. The fluorescent molecule is stimulated by an excitation source such as a laser or a lamp, and the emission is captured by a camera or photomultiplier tube (PMT) (Cox, 2012).

Wide-field microscopy

Wide-field fluorescent or epifluorescent imaging typically uses a lamp for excitation, such as a xenon-arc, mercury-vapour lamp or light emitting diode (LED). The term wide-field is derived from the fact that the source illuminates a large portion

of the sample. Typically the sources are wide-band, emitting electromagnetic radiation across a large spectrum. As a result, this technique requires excitation filters to limit the wavelength of the light the sample is exposed to. LEDs are capable of both emitting a light within a specified bandwidth and wide-band emission.

Typically, an epifluorescent optical setup employs a filter cube for isolating excitation and emission wavelengths. The filter cube consists of an excitation filter, a dichroic and an emission filter. The excitation spectra isolates the desired wavelengths from the broadband light source and the dichroic reflects the excitation light onto the sample. Light emitted from the sample is of a longer wavelength than the excitation light, and is allowed to pass through the dichroic before being further isolated by the emission filter and presented to the camera (Liang, 2013).

Charge-coupled device (CCD) and complimentary metal-oxide-semiconductor (CMOS) cameras are popular devices for capturing wide-field fluorescent data. These cameras usually contain high-density light sensitive pixels optimised to capture electromagnetic radiation in the 400 - 800nm range.

Point scanning microscopy

The term laser stands for Light Amplification by Stimulated Emission of Radiation. Lasers emit a collimated, spatially and temporally coherent beam of light that allows it to be focused to a tight spot at a single wavelength. Lasing can be achieved by a number of methods and lasers have many applications, such as laser cutting, photolithography and optical imaging (Liang, 2013).

Laser sources typically produce electromagnetic radiation at specific wavelengths. Most point scanning systems do not require excitation filters, but do require emission filters.

A PMT is a vacuum phototube with high enough sensitivity to record the occurrence of single photon events. It uses the photoemission and secondary emission phenomena to amplify the signal produced by incident light. PMTs are capable of

detecting ultraviolet, visible and infrared light. They are popular in point-scanning applications (Cox, 2012).

Photo diodes are light-sensitive diodes designed for the transduction of light into electrical signals. Photo diodes fill a functional gap somewhere between PMTs and camera: they have higher sensitivity than cameras but a reduced number of sensors, or pixels. They are often used in an array format similar to that seen in cameras. Depending on the number of photo diodes available, they can be used for either wide-field or scanning-point imaging.

Confocal microscopy uses a laser source, like an Argon-ion, which is raster scanned across a sample using two scanning mirrors. A PMT is used to capture the emitted light through an aperture called the pinhole. The pinhole is designed to restrict out-of-plane light from reaching the image sensor, in essence providing imaging at a single point with x, y and z isolation (Liang, 2013).

Two-photon microscopes are very similar to confocal microscopes in that they are laser scanning microscopes. They take advantage of a phenomenon known as two-photon absorption whereby two photons of half the necessary energy (twice the desired wavelength) arrive at a fluorescent molecule at virtually the same time, creating excitation at the desired energy and wavelength. This non-linear phenomenon requires a large number of photons in a very small volume. It was made possible with the invention of femtosecond pulsed lasers, such as the titanium-sapphire laser. One major advantage over confocal microscopes is that the requirement of a critical mass of photons limits the excitation to a small volume around the focus of the objective, which can be raster-scanned by the scanning mirrors (Cox, 2012).

2.6 Computational modelling of electrophysiology

Mathematical modelling of electrical activity of excitable cells was pioneered by Alan Hodgkin and Andrew Huxley in their 1952 paper, describing the non-linear equations to replicate action potentials in the squid giant axon (Hodgkin and Huxley, 1952). Many mathematical and computational models of excitable cell electrical activity use at least part of the Hodgkin-Huxley formalism.

The HH model describes the cell membrane with an electric circuit analogue (Figure 2.8). The lipid bilayer is represented by a capacitance C_m , parallel conductances represent the ion channels, g_j where j is the membrane current type or number. The electrochemical gradient is represented by batteries, $E_{rev,i}$ and pump or exchangers are represented by current sources (not shown).

The membrane in Figure 2.8 can be described by a space-clamped ordinary differential equation (ODE):

$$\frac{dE_m}{dt} = -\frac{1}{C_m} \left(i_L + \sum_{j=1}^N i_j \right) \quad (2.1)$$

where i_L is the time-independent leakage current and i_j is the j -th time-dependent ionic current and N is the total number of time-dependent currents.

In the HH formulation, time-dependent membrane conductance g_j are calculated by the product of the maximum number of membrane channels for each ion type:

$$g_j(E_m, t) = \bar{g}_j \prod_j x_j(E_m, t)^{n_j} \quad (2.2)$$

where $x_j(E_m, t)$ represents the gating variables, \bar{g}_j is the maximum conductance for the j -th channel, and the power n_j depends on the kinetics of the j -th ionic current. Gating variables are given as n , m or h and each plays a role for specific

ionic currents. Each gating variable can be represented as a first order differential equation,

$$\frac{dx(E_m, t)}{dt} = \alpha(1 - x) - \beta x \quad (2.3)$$

where $\alpha(E_m)$ and $\beta(E_m)$ are the opening and closing rates for their corresponding gating variable x , and are functions of the membrane potential, E_m . Each ionic current takes on the following form:

$$i_j(E_m, t) = g_j(E_m, t) \cdot (E_m - E_{rev,j}), \quad (2.4)$$

where E_m is the membrane potential, i_j is the j -th ionic current, and $E_{rev,j}$ is the j -th ionic current reversal potential.

Mathematical models of excitable cell electrical activity can be divided into two categories: biophysically-realistic and phenomenological models. Biophysically-accurate models attempt to take into account all cellular biological activity leading to electrical excitation. They often contain a large number of variables due to their large number of membrane currents, and are computationally expensive to simulate. Phenomenological models attempt to replicate AP characteristics with more simplified formulations. Many of these simplified models are derived from biophysically-accurate models by making certain assumptions in order to reduce mathematical complexity.

2.6.1 A generic ionic model

An expandable and robust computational model which employs simple Hodgkin-Huxley type dynamics to simulate electrical activity in excitable cells is the generic ionic model of Guo et al. (2010). In its simplest form, this generic ionic model consists of three currents: a time-dependent outward current, i_1 ; a time-dependent

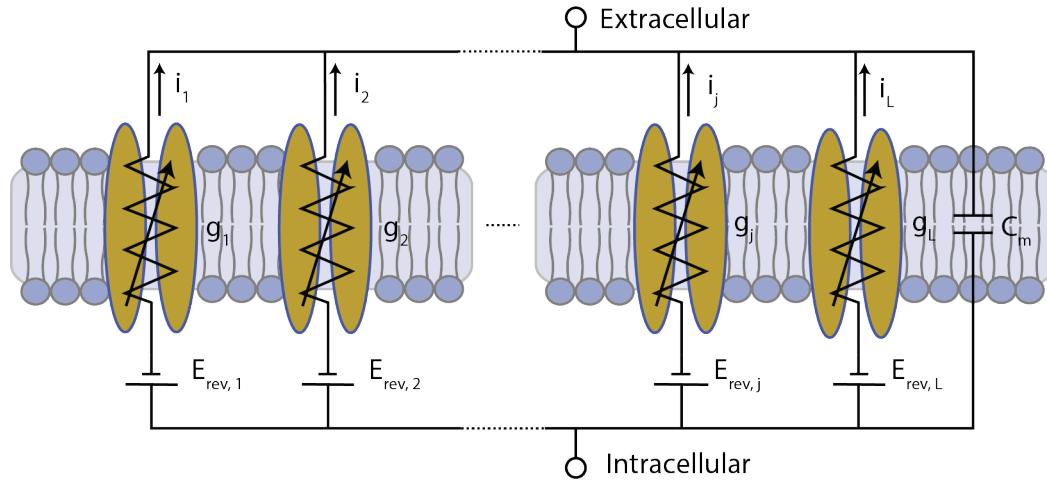


FIGURE 2.8: Basis for the generic ionic model

inward current, i_2 ; and a leakage current i_L . The standard space-clamped ODE is:

$$\frac{dE_m}{dt} = -\frac{1}{C_m} (i_1 + i_2 + i_L) \quad (2.5)$$

where E_m is the transmembrane potential, C_m is the membrane capacitance, i_1 is a generic time-dependent outward current, i_2 a time-dependent inward current and i_L a leakage component. The generic ionic model is arbitrarily extendible in that currents can be added to fit more complex datasets, such as cells undergoing pharmacological treatment (Guo et al., 2013). The generic form of the ODE is given by:

$$\frac{dE_m}{dt} = -\frac{1}{C_m} \left(i_L + \sum_{j=1}^N i_j \right) \quad (2.6)$$

where i_j signifies the j -th time-dependent ionic current and N is the total number of such currents.

Each time-dependent ionic current is represented by a two-state Hodgkin-Huxley gating variable scheme as:

$$i_j = \bar{g}_j p_j q_j (E_m - E_{rev,j}) \quad (2.7)$$

where \bar{g}_j is the maximum membrane conductance, p_j and q_j are dimensionless Hodgkin-Huxley gating variables, and $E_{rev,j}$ is the reversal potential of the j -th ionic current.

The leakage current, varies slightly from the time-dependent ionic currents in Equation 2.7 in that there are no p and q gating variables. The leakage current is given as:

$$i_L = \bar{g}_L (E_m - E_{rev,L}), \quad (2.8)$$

where \bar{g}_L is the maximum channel conductance and $E_{rev,L}$ is the leakage current reversal potential. The gating variables p and q of Equation 2.7 are governed by:

$$\frac{dp_j}{dt} = \alpha_{p,j} (1 - p_j) - \beta_{p,j} p_j, \quad (2.9a)$$

$$\frac{dq_j}{dt} = \alpha_{q,j} (1 - q_j) - \beta_{q,j} q_j, \quad (2.9b)$$

where $\alpha_{p,j}$, $\alpha_{q,j}$, $\beta_{p,j}$, $\beta_{q,j}$ are the opening and closing rates of their respective gating variables for the j -th current. The opening and closing rates are empirical functions of the membrane potential:

$$\alpha, \beta = \frac{k}{1 + \exp[s(E_m - E_{50})]}, \quad (2.10)$$

where k , s and E_{50} are parameters specific to each rate, with each E_{50} parameter value shared between the α and β pair for each gating variable.

2.6.2 Cable and network models

Single cell models, such as the generic ionic model, can be implemented in more complex geometries such as multi-compartmental cables and networks. The latter

is accomplished by connecting each cell to a neighbouring cell via a resistance representing a gap-junction connection (McCulloch et al., 1998). In this thesis, a monodomain implementation of a network model will be used, so the extracellular space is considered to be at iso-potential, in this case ground. Figure 2.9 illustrates the transition from single cell to cable and finally network model. The derivation for the multi-compartmental cable and network models is covered in detail in Section 4.6.

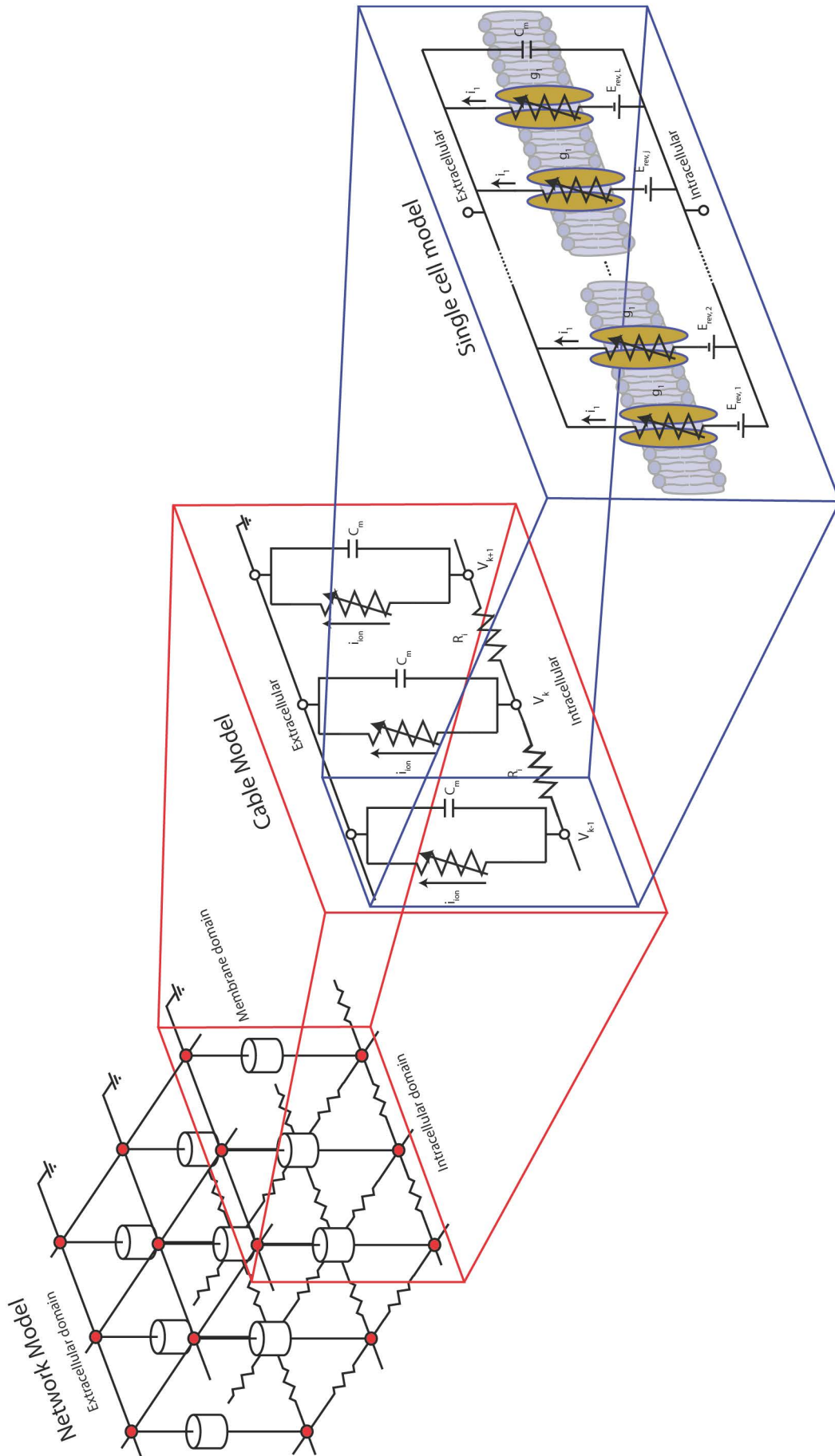


FIGURE 2.9: The transition from a single cell model (right-most pane) to the network model (left-most pane).

Chapter 3

Existing single-cell models of cardiac electrical activity

3.1 Simplified computational models

3.1.1 FitzHugh-Nagumo based models

The FitzHugh model is a simplified generic model of excitable media, derived originally by FitzHugh (1961) and expanded upon by Nagumo et al. (1962) to form the FHN model. The model is a simplification of the Hodgkin-Huxley model of the squid giant axon. The original FHN equation is given as:

$$\frac{du}{dt} = c_1 u(u - u_{th})(u - 1) + c_2 n, \quad (3.1a)$$

$$\frac{dn}{dt} = c_3(u - c_4 n), \quad (3.1b)$$

where u and n represent the normalised membrane potential and a recovery variable respectively, and c_1 - c_2 and u_{th} are model parameters. While the FHN model has been used for large-scale cardiac electrophysiological modelling, it has a number of limitations, including a lack of:

- rate dependence of AP and conduction velocity (CV) (can be remedied with modification)
- separate time scale for depolarization and repolarisation
- non-zero minimum diastolic interval

The FHN model has been frequently modified for cardiac modelling, but is not itself a cardiac specific model.

The first adaptation to the FHN model for the purposes of cardiac modelling was Van Capelle and Durrer (1980). This model consists of two variables, the membrane potential (V_m) and cell excitability (n). The formulation is as follows:

$$\frac{dV_m}{dt} = -I_{tot}, \quad (3.2a)$$

$$I_{tot} = -ni_1(V_m) - (1 - n)(i_1(V_m) + i_2(V_m)), \quad (3.2b)$$

$$\frac{dn}{dt} = -\frac{n_\infty(V_m) - n}{\tau_n(V_m)}, \quad (3.2c)$$

where n_∞ and τ_n are the steady-state value and time constant respectively for the cell excitability variable, n , and $i_1(V_m)$ and $i_2(V_m)$ are current-voltage empirical piecewise functions for defining system dynamics. Provided with appropriate parameters, both quiescent and pacemaking membrane potentials can be simulated.

Attempts to reproduce more accurate cardiac AP waveshapes led to another FHN-based model by Rogers and McCulloch (1994). This model increased the upstroke velocity of APs and removed after-hyperpolarisation characteristics by modifying Equation 3.1a to include the normalised membrane potential in the rightmost component:

$$\frac{du}{dt} = c_1u(u - u_{th})(u - 1) + c_2un \quad (3.3)$$

The Rogers-McCulloch model was used to simulate propagation through heterogeneous tissue, like seen in the ventricular wall. It is capable of reproducing basic cardiac cell electrical activity.

To model electrical activity in the sinoatrial node and its effect upon heart rate Sato et al. (1994) modified the FHN system of equations further by implementing an additional parameter, designated c_5 here, added to Equation 3.1b to produce:

$$\frac{dn}{dt} = c_3(u - c_4n - c_5), \quad (3.4)$$

where c_5 is used to adjust the nullclines of u and n such that they intersect at an unstable fixed point, resulting in autorhythmic activity similar to that seen in the cardiac pacemaker.

To study APs and cycle length dependency of 3D canine hearts the Rogers-McCulloch modified FHN equations were used by Aliev and Panfilov (1996). The model introduced anisotropic conductivity properties to the syncytia and modified the $\frac{dn}{dt}$ equation to improve simulation accuracy. The modification was in the form of a quadratic term with respect to u and n . Two-dimensional and cable models were implemented and restitution properties were found to have a significant effect upon re-entrant vortex dynamics. Vortex action potential duration (APD_{90}) was initially twice that of the linear wavefronts; however, the vortex APD_{90} settled to be approximately equivalent to the linear wavefronts. Further, a 3D model of the canine ventricles was described and re-entry simulated. After initial stimulation the re-entrant signal stabilised into a stationary vortex. The Aliev-Panfilov model faithfully simulates restitution properties of cardiomyocytes and more closely resembles features of experimental data, including AP shape, than any of the previous FHN derived models.

Even with the significant work done improving the characteristics of the FHN model, it still has serious limitations restricting its application to specific studies. FHN models typically aren't concerned with precise waveshape and tend to be popular for use in complex geometries. The lack of minimum diastolic interval

and the model's inability to account for any ionic processes has restricted the further progression of FHN-derived models.

3.1.2 Fenton-Karma based models

The Karma (1993) model, adapted from the (Noble, 1962) model, consists of two variables and was built to study the effect of alternans-based spiral wave break up. The Karma model effectively recreated oscillatory pulse dynamics (alternans), but was mathematically limited in its ability to replicate some experimental observations. Notably, the model falters when the ratio of the time scale between AP upstroke and duration approach zero. The Karma model exhibits more-realistic AP waveshapes when compared to the FHN model.

The Fenton and Karma (1998) model is a three-variable model of the cardiac action potential. It draws a number of parallels with the generic ionic model presented in Section 2.6.1. The Fenton-Karma model used a three current system; a fast inward, a slow inward and a slow outward. To represent cardiac APs, the model employs three variables, one membrane voltage and two gating variables. The parameters in the Fenton-Karma model can be adapted to alter properties such as AP duration, minimum diastolic interval, AP upstroke and restitution curves. The three-variable ODE system of the Fenton-Karma model is as follows:

$$\frac{du}{dt} = -(J_{fi}(u, v) + J_{so}(u) + J_{si}(u, w)), \quad (3.5a)$$

$$\frac{dv}{dt} = \frac{H(u_c - u)(1 - v)}{\tau_w^-(u)} - \frac{H(u - u_c)v}{\tau_v^+(u)}, \quad (3.5b)$$

$$\frac{dw}{dt} = \frac{H(u_c - u)(1 - w)}{\tau_w^-(u)} - \frac{H(u - u_c)w}{\tau_w^+(u)}, \quad (3.5c)$$

where u represents the normalised voltage, v and w gating variables, $J_{fi}(u, v)$ the fast inward current, $J_{so}(u)$ the slow outward current, $J_{si}(u, w)$ the slow inward

current, given by:

$$J_{fi}(u, v) = -\frac{v}{\tau_d} H(u - u_c)(1 - u)(u - u_c), \quad (3.6a)$$

$$J_{so}(u) = \frac{u}{\tau_0} H(u_c - u) + \frac{1}{\tau_r} H(u - u_c), \quad (3.6b)$$

$$J_{si}(u, w) = -\frac{w}{2\tau_{si}} (1 + \tanh[k(u - u_c^{si})]), \quad (3.6c)$$

and $H(x)$ the Heaviside step function given by:

$$H(x) = \begin{cases} 1 & x \geq 0 \\ 0 & x < 0 \end{cases} \quad (3.7)$$

The Fenton and Karma (1998) model implemented anisotropic conductivity properties of the ventricle, finding that rotational anisotropy alone generated chaotic electrical behaviour. Validation was performed by fitting model restitution curves to experimental data. Importantly, the Fenton-Karma model was not able to accurately reproduce AP waveshapes, instead relying on reproducing restitution curves when modelling spiral activity.

Further adaptations were made to the Fenton-Karma model to produce more accurate AP morphologies (Fenton et al., 2002, 2004). A d variable was incorporated to replace the steady state function of the slow inward current $J_{si}(u, w)$ given by $(1 + \tanh[k(u - u_c^{si})])$ with the d gating variable, producing:

$$\frac{dd}{dt} = [0.5 (1 + \tanh[k(u - u_c^{si})]) - d], \quad (3.8)$$

while $J_{si}(u, w, d)$ was given as:

$$J_{si}(u, w, d) = -\frac{wd}{\tau_{si}}, \quad (3.9)$$

where τ_x is the time constant of the respective component and k is the activation width parameter. The Fenton-Karma model, with an increased number of parameters was used to investigate the mechanisms of spiral wave break up (Fenton et al., 2002).

Another alteration was made in the Cherry and Fenton (2004) model by the addition of a y gating variable to the slow outward current in an attempt to exacerbate the effects of memory on the model by the slight adjustment of rapid delayed rectifier current K^+ current (i_{Kr}). The y gating variable is given as:

$$\frac{dy}{dt} = \frac{p(1-y)}{\tau_y^+} - \frac{(1-p)(y-0.1)}{\tau_y^-}, \quad (3.10)$$

where p is a step function, and τ_y is the time constant for the y gating variable. This adaptation led the slow outward current to take the form of:

$$I_{so}u = \frac{u(1-r)(1-vk_2)}{\tau_0} + \frac{ruy}{\tau_r}, \quad (3.11)$$

where r is a step function.

The Cherry and Fenton (2004) model investigated the effect of action potential duration (APD) restitution curves, memory and electrotonic currents in prediction of alternans and re-entrant behaviour in rabbit ventricles. The model was implemented in both two and three-dimensional geometries and found that the presence of memory and electrotonic currents, even with steep APD restitution curves, were able to suppress alternans. The Cherry and Fenton (2004) did not fit to AP waveshape, rather it focused on tissue level characteristics such as CV.

A final adaptation by Bueno-Orovio et al. (2008) led to the minimum human ventricular model, based on the four variable Fenton-Cherry model with various parameters to simulate epicardial, midmyocardial, and endocardial tissue. The model was able to replicate dynamics seen in vastly more complex computational models, including CV restitution, AP amplitude and morphology, upstroke velocities and minimum diastolic interval, all while being significantly simpler computationally.

The four variable Fenton-Karma model fulfils the ideological goals of simplified models by accurately reproducing dynamic events seen experimentally while maintaining minimal computational complexity. As a result, it has become popular for tissue-level modelling. Its popularity has so far been isolated to ventricular studies, with fewer atrial studies and no studies of the cardiac pacemaker.

3.1.3 A simplified generic ionic model

The generic ionic model is a computational model based on Hodgkin-Huxley dynamics that lies between a phenomenological formulation (FHN) and a biophysically detailed model, such as the Courtemanche et al. (1998) model (Guo et al., 2013). It is capable of fitting cardiac electrical activity and is arbitrarily extendable by the addition of currents that can each be formulated with a set of two gating variables and 12 parameters. Guo et al. (2013) used a multi-objective optimisation approach to fit central SAN, peripheral SAN, right and left atrial experimental data from intact rabbit cardiac preparations, with the ability to fit multiple datasets simultaneously. The study focused on single cell electrophysiology extracted from impaled cells in whole atrial preparations.

The generic ionic model was further optimised to model electrical activity under one-dimensional electrotonic loading (Al Abed et al., 2013). Single cell sharp electrode data from a number of intact rabbit atrial tissue was used to optimise the parameters in the presence of electrotonic load from neighbouring cells. A three-current model was utilised to replicate AP morphology and other characteristics. The central SAN, peripheral SAN, right atrium, left atrium and pulmonary veins were all represented in the 1D version. Further, the model was implemented in a complex atrial geometry based on the human visible male dataset (Spitzer and Whitlock, 1998) and maintained spontaneous electrical activity derived from the SAN.

It is useful to compare the complexity of the various published models to establish the necessary mathematical detail to reproduce experimental results. Excess

TABLE 3.1: Complexity of simplified models

Model	Variables	Parameters
FHN	2	8
Fenton-Karma	3	13
Fenton-Cherry	4	23
Generic ionic model	>5	>26

complexity leads to redundancy and extended computation times: at the tissue scale this can become a detrimental factor. Bueno-Orovio et al. (2008) were able to effectively simulate phenomena seen in more complex models while solving, in the best case, 31x faster than the least complex alternative. The simplified model should be complex enough to simulate the desired behaviour but no more complex. Herein lies one advantage of the generic ionic model, its complexity can be adapted to the experimental data that it is being reproduced. For example, Guo et al. (2013) introduced both 5 and 8 current iterations of the generic model in order to fit single cell multiple-datasets simultaneously. The generic ionic model has reproduced drug-based effects on AP waveshape, the waveshape of multiple tissue types (SAN, atrial, pulmonary vein) and electrical activity in 1D and 3D preparations (Al Abed et al., 2013, Guo et al., 2010). By comparison, FHN based models do not provide the necessary flexibility to reproduce AP waveshape, and the Fenton-Cherry derivatives are limited in their complexity although they do provide a reasonable ability to fit experimental data. The generic ionic model has a basic formulation that uses 5 variables and 26 parameters and is, unlike other models, arbitrarily extendible by the addition of currents to reproduce cardiac electrical phenomena. The complexity of all the single cell cardiac models of this section is summarised in Table 3.1, and a summary of simplified model chronology is presented in Table 3.2.

TABLE 3.2: The development of simplified/generic computational models

	Generic model	
Origin	Hodgkin and Huxley (1952)	Beeler and Reuter (1977) Luo and Rudy (1991)
Simplification	FitzHugh (1961), Nagumo et al. (1962)	Fenton and Karma (1998)
Modification	Van Capelle and Durrer (1980) Rogers and McCulloch (1994) Sato et al. (1994) Aliev and Panfilov (1996)	Cherry and Fenton (2004) Bueno-Orovio et al. (2008)
Application	General quiescent and spontaneous AP shapes Reasonable restitution properties Whole heart simulation	Well defined non-zero minimum DI Realistic quiescent AP waveform Realistic restitution properties Detailed Model-generated behaviour Re-entrant wave dynamics

3.2 Biophysically-accurate models of mouse myocytes

The first biophysically-accurate model of mouse cardiomyocytes was the Bondarenko et al. (2004) ventricular cell model. The model employed a combination of Hodgkin-Huxley and Markov dynamics to represent ion channel activity and the activity of internal structures such as the sarcoplasmic reticulum. The sodium current, i_{Na} , the L-type calcium current, $i_{Ca(L)}$ and the rapid delayed rectified potassium current, i_{Kr} were represented using Markov systems. The model employs 15 ionic currents, sodium-calcium and sodium-potassium exchangers, intracellular Ca^{2+} -handling, and transmembrane pumps. The complexity of the model led to the utilisation of data from other species to fully identify the model parameters. In total 40 ordinary differential equations and 70 parameters were used to simulate ventricular APs. This study is limited to isolated single cell electrophysiology, it does not consider the effect of interconnections between the cells in tissue. The model simulates ventricular cells found in the apex and the septal regions of the ventricle.

To study the effect of ion channel and structural manipulations on the distribution of extracellular potentials, Tranquillo et al. (2005) described a bidomain model of the mouse ventricle which was adapted from the Pandit et al. (2001) single cell rat model. This model employed a realistic geometry reconstructed from diffusion tensor magnetic resonance images that incorporated fibre organisation. The model replicated three cell types; the right ventricle, left ventricular epicardium and endocardium. The maximum conductance of the transient outward current was altered to adjust AP waveshape to better fit the mouse AP.

In order to describe the Tranquillo et al. (2005) model, it is necessary to briefly cover the structure of the Pandit et al. (2001) model. The latter simulated rat epicardial and endocardial ventricular myocytes, and was based on Hodgkin-Huxley dynamics. The model simulated the ionic processes with seven currents, two

pumps, and one exchanger. Further, the model incorporated intracellular and sarcoplasmic reticulum calcium storage and release dynamics. The model included 26 variables and 57 parameters.

The only model of the mouse SAN is the Mangoni et al. (2006) formulation which was developed to study the effect of T-type calcium current on the pacemaking capabilities of the SAN. The model used 22 variables and 17 membrane currents to simulate electrical activity in the SAN. This model was modified from the Zhang et al. (2000) rabbit SAN model by adding calcium currents. Validation of AP simulation was performed on electrophysiological data acquired in isolated mouse cells.

For completeness we cover the Zhang et al. (2000) model, a simulation of the rabbit central and peripheral SAN. This model employed 15 variables, one membrane voltage and 14 gating variables and included 14 transmembrane currents. Hodgkin-Huxley dynamics were used to simulate ionic processes and ion concentrations were taken into account.

More recently, Land et al. (2012) formulated a 3D model of the mouse ventricles to investigate the effect of excitation-contraction coupling at the cellular level on whole organ function. The electrophysiological components of the model were limited to calcium dynamics based on the modified Li et al. (2011) model. The model can replicate both single cell and whole organ behaviour at physiological temperatures and activation rates. Briefly, the Li et al. (2011) formulation simulated calcium dynamics in mouse ventricular myocytes. The model was validated against isolated ventricular myocytes, from knock out and control mice.

3.3 Optimisation of a computational model of mouse cardiac electrical activity

In this thesis we present a novel computational model of H1-1 myocytes, based on the generic ionic model of Guo et al. (2013). Optimised to fit both single

cell and tissue-level electrophysiological data. There has been limited work in the literature in modelling of electrical activity in the mouse atria and to our best knowledge, there are no computational models specifically targeting the mouse atrial cardiomyocyte.

A major limitation of the existing models reviewed in this chapter is the validation of the models. A portion of these models validated against data from other publications, occasionally requiring cross-species data to fully identify model parameters and variables. The data was typically recorded in single cell electrophysiological recordings, and was rarely fitted to tissue-level data, with the exception of the Al Abed et al. (2013) model of the rabbit atria. In this thesis, we model and optimise not only single cell electrophysiological activity, but also electrical interactions at the tissue-level in order to better represent the electrophysiological system. We map AP waveshape to single cell electrophysiological activity and use tissue-level optical imaging to quantify and fit properties of propagation and multicellular interaction.

Our model represents a platform upon which further studies in cardiac electrophysiology can be undertaken. The generic ionic model is a shift away from current trends in the literature of creating models that reproduce cardiac electrical activity by implementing a large range of ionic and cellular processes. The generic ionic model is as simple as the phenomenological models and extensible enough to recreate complex electrophysiological phenomena seen in biophysically-accurate models. Further, we provide comprehensive validation of our model by optimising parameters against experimental data in both single cell and multi-cellular cardiac preparations.

Chapter 4

Methods

4.1 HL-1 culture

HL-1 cells were received at passage 48 from Dr. William Claycomb (Louisiana State University Health Science Centre, New Orleans, LA, USA) in conjunction with Dr. Patsie Polly (Inflammation and Infection Research Centre and Department of Pathology, UNSW, Sydney, Australia).

Cell culture was performed in a tissue culture laboratory under sterile conditions. Cell maintenance, such as passaging, was completed in a biosafety cabinet. Cells were grown in fibronectin-gelatin (Sigma Aldrich, Sydney, Australia) coated T25 flasks at 37 °C in an atmosphere of 5% CO₂ and 95% air with a relative humidity of 95%. Cells were cultured in Claycomb media (Sigma Aldrich, Sydney, Australia) supplemented with 10% fetal bovine serum, 2 mM L-glutamine, 100 μM norepinephrine and 100 U/mL:100 μg/mL penicillin/streptomycin (Sigma Aldrich, Sydney, Australia). Media was refreshed every 24 hours. Cells were grown to confluence and split 1:3 twice a week. Appendix A covers our culturing protocol in detail.

4.1.1 Experimental preparation

Cells were plated on fibronectin-gelatin coated 35 mm glass coverslips (ProSciTech, Queensland, Australia) and cultured in Claycomb media under sterile conditions until fully confluent. Claycomb media is extremely light sensitive and is not ideal for experiments with constant light exposure. The base of Claycomb media is Dulbecco's modified Eagles medium (DMEM) which has no known light sensitivity but contains non-essential components, such as amino acids, for acute experiments such as our electrophysiological studies. Historically, Tyrode's solution has been used when studying the electrophysiology of HL-1s (Claycomb et al., 1998, Sartiani et al., 2002).

The use of Tyrode's is common in physiological experiments with mammalian cells, and is frequently used in experimental protocols involving HL-1 cardiomyocytes (Claycomb et al., 1998, Sartiani et al., 2002, Umapathy et al., 2008). Tyrode's provides the experimenter with a minimal salt solution for the acute maintenance of HL-1 cells and is the salt solution of choice for this work. One point worth noting is that Tyrode's must be slowly introduced to the cells. The disparity between the ionic constitution of DMEM and Tyrode's pushes the cells into isotonic or osmotic shock, and can eliminate the spontaneous nature of cell activation. They can take hours to recover and occasionally did not fully recover synchronous activity. The Tyrode's formulation used was as follows (mM): NaCl, 140; KCl, 3; MgCl₂, 2; CaCl₂, 2; HEPES, 10; glucose, 10 (pH adjusted to 7.35 with NaOH).

Tyrode's was slowly introduced to the experimental preparation by diluting the existing DMEM with fresh Tyrode's over the course of 10 minutes until Tyrode's was the sole solution. Once cells were contracting steadily in Tyrode's solution, they were quickly moved to the microscope where they were perfused with Tyrode's heated to 32 – 35 °C using a SH-27B in-line heater and TC-344B temperature controller (SDR Scientific, Castle Hill, NSW, Australia) at 1-2 mL/min. Tyrode's was gravity fed through a drip into the imaging chamber and was extracted by a

Masterflex L/S compact peristaltic pump (John Morris Scientific, Victoria, Australia) and returned to the reservoir. Cells were maintained in these conditions for the duration of the experiment.

4.2 Experimental setup

The microscope used was a LaVision TrimScope II (LaVision Biotec Asia-Pacific, South Australia, Australia), which is a heavily modified BX WI series Olympus microscope retaining only the condenser, filter wheel and trinoculars. The camera was a PCO.edge sCMOS camera (PCO AG, Kelheim, Germany). For epifluorescence an LDGI Xcite 120Q (Lumen Dynamics Group Inc., Ontario, Canada) was used. The Xcite 120Q uses a 120W mercury vapour short arc. Filter setup for optical mapping with di-4-ANEPPS was as follows: 525/50 band-pass excitation filter, 624 dichroic, 655/40 band-pass emission filters. The optical train used in the experiments is illustrated in Figure 4.1.

The LaVision system was also equipped with a Mai Tai femtosecond pulsed laser and an Insight DeepSee femtosecond laser (Newspec, SA, Australia). The Mai Tai is capable of being tuned from 690nm to 1040nm; while the Insight DeepSee could be tuned from 680nm to 1300nm. The LaVision system has a multi beam mode where the laser beam is split into 64 beamlets to sweep across a large section of the sample quickly. The above-mentioned laser scanning systems are most useful for thick samples and their results are not presented in this thesis. However, they remain relevant for future work.

Imaging with the PCO.edge was performed using a combination of Inspector Pro (LaVision Biotec, SA, Australia) and CamWare (PCO AG, Kelheim, Germany). The lasers and shutters were controlled using Inspector Pro, while CamWare was used to record time-lapse fluorescent data and single brightfield images. The three primary objectives used on the LaVision system were: a 4X Olympus XLFLUOR 0.28 NA, an Olympus LUMPLFLN 40XW 0.8 NA, and a Zeiss 20X W Plan Apochromat 1.0 NA.

For electrophysiological recordings a Multiclamp 700B, Digidata 1440A and CV-7B headstage were used in conjunction with pClamp software (Molecular devices, California, USA). A Sutter MP-225 (SDR Scientific, Castle Hill, NSW, Australia)(Sutter Instrument Co., California, USA) was used for micromanipulation of glass electrodes.

Electrical recording by glass microelectrodes was used for the confirmation of optical function and cell type. Sharp microelectrodes were used to impale cells to enable comparison between the change in fluorescence of the di-4-ANEPPS molecule with actual changes in membrane potential, V_m . A secondary purpose for the impalement was to confirm that the cell types in our cultures were in accord with those seen in the literature as well as an assurance of continued cellular electrical activity during experimentation. Cell activity was also confirmed visually by active contraction of the cardiomyocytes.

For all glass electrodes Warner premium glass capillaries (SDR Scientific, Castle Hill, NSW, Australia), fire polished and with filaments, were used. For sharp electrode work, 1.2 mm outer diameter (OD) by 0.69 mm inner diameter (ID) capillary glass was used. Glass electrodes were pulled with a P-97 Flaming/Brown microelectrode puller (SDR Scientific, Castle Hill, NSW, Australia). A pipette resistance of 50-100 M Ω was used for cell impalement.

Sharp electrodes were pulled on the day of experiments and filled with 3M KCl just prior to recordings. Resistances were between 50 and 100 M Ω . Resistances lower than 50 M Ω or tips that were compromised were discarded. Once a cell was impaled, stable recordings were taken under normal physiological conditions at 32 – 35°C. Recordings were either taken on their own or in combination with optical recordings. Electrical activity was acquired at 10-20 kHz without filtering or pre-processing. Excitation-contraction uncouplers were not used for electrical recordings, the preparation produced isolated contraction and most contraction was not strong enough to compromise the impalement or recordings. Cells that were non-contractile were given preference when impaling.

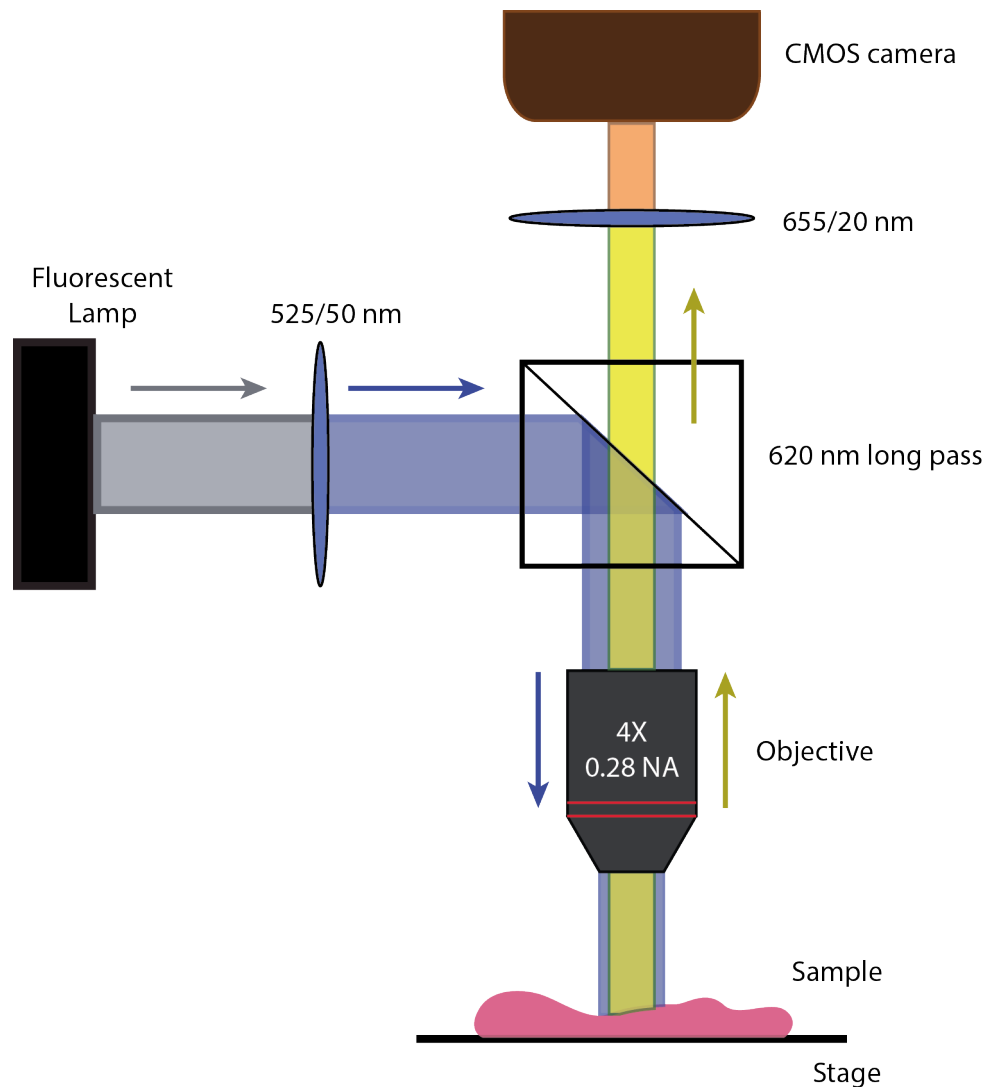


FIGURE 4.1: Diagram of optical setup used for imaging of di-4-ANEPPS in HL-1 cells. The filters are annotated with peak/full-width-half-maximum (FWHM) for bandpass filters and the edge wavelength for dichroics/long-pass filters.

4.2.1 Correlating electrical and optical activity

In order to correlate the electrical activity of the cell with changes in fluorescent intensity of the di-4-ANEPPS molecule, we performed simultaneous sharp electrode impalements with optical recording. The methods used for electrical and optical recordings are described above. First, a cell was impaled with a sharp glass microelectrode and then optical activity was recorded from the impaled cell and surrounding cells using a 40X 0.8 NA Olympus objective at around 300 Hz

frame rate. Recordings were post processed, filtered and plotted against one another to illustrate the correlation between activities. The results are presented in Section 5.2.2.

4.3 Spectral analysis

Analysis of the single photon emission spectra was performed on a Leica TCS SP5 CW STED inverted microscope using a 40X 0.75 NA air objective. HL-1 cells were plated on fibronectin-gelatin coated glass and grown to confluence before being stained with 5 μ M of di-4-ANEPPS in Claycomb's medium (final concentration) for 10 minutes, then washed 3 times with phosphate-buffered saline (PBS). Cells were incubated on the microscope at 37°C and allowed to equilibrate. The spectra was analysed over a 512 x 512 pixel section of tissue using the Lambda scan function in the Leica software. The Lamda scan function selects a particular excitation wavelength (488 nm or other) and the emission spectra is segmented into 10 nm blocks, using the acousto-optic tunable filter, and stepped through to retrieve the emission intensity curve. The emission curve was fitted with a skewed Gaussian to provide a smooth spectra using the Scipy curve fitting algorithm. This data is presented in Section 5.2.1.

4.4 Post-processing of experimental data

Tissue conduction velocity was calculated using optical mapping data by selecting two points at a distance from one another, the further apart the better. The difference in time between the peak of each AP at the points of interest were found, the time delay was divided by the physical distance between the two points to calculate conduction velocity. The beat rate was determined by calculating the difference between optical action potential (OAP) peaks at a specific point of interest. We chose to require at least three OAPs at each node to calculate the conduction velocity and beat rate. Here we define a node as a spatially averaged

point in the 2D optical imaging data. In that sense, a node represents the average of a 20 x 20 region of interest. Activation refers to the activation of the cell or cells resulting from an action potential. In this case, the activation is represented by a change in fluorescence as a result of the membrane potential sensitive dye used.

In order to quantify optically recorded and simulated wavefronts, we calculated the width of the wavefront, at a given time, that was at or above 50% of maximum activation. In the case of experimental data, we took the region that was above 50% of the maximum change in fluorescence. For modelled AP wavefronts, we isolated the area at which the AP surpassed 50% of the maximum membrane potential. We took the time at which a given node, n_1 , reached 50% AP amplitude during depolarisation t_{d,n_1} and repolarisation, t_{r,n_1} . We then found the furthest node n_2 from the initial point, n_1 , at which the AP was both depolarising and had reached at least 50% AP amplitude, at the time t_{r,n_1} . The distance between nodes n_2 and n_1 was designated the 50% wavefront width. At least three AP waveforms at each node were required to complete the comparison, each 50% wavefront width was calculated separately and then averaged.

To evaluate the shape of spiral wavefronts, recorded and simulated we determined the rotor radius against the angle of rotation. This was calculated by isolating the front-most portion of the OAP wavefront. The region of interest was selected as the most recent nodes to have passed 50% AP amplitude. The radii were calculated from the centre most node in the spiral that most recently passed 50% OAP amplitude. Distances were calculated as a function of the angle of rotation, θ , which was scaled to lie between 0° and 360° . In the case where there were multiple wavefronts from the original spiral in the image, only the inner most wavefront was taken into account: this typically only occurred in the large scale computational models.

4.5 Optimisation of the cardiomyocyte action potential

AP data were visualised post-experiment using Stimfit. APs were divided into two types dependent upon whether, or not, they displayed a slow phase 4 depolarisation. Those with slow phase 4 depolarisation were designated pacemaking and those without were labelled non-pacemaking. After sorting the microelectrode data into pacemaking and non-pacemaking, the most stable signal was selected for single cell optimisation. The signal was notch filtered with an inverted Gaussian characteristic at 50 Hz. Three to six consecutive APs were isolated and the signal was down-sampled to 1 kHz for optimisation. In this thesis we only optimised model parameters to fit non-pacemaking cells.

The optimisation code employed a curvilinear gradient method for minimising the error between the computational model and the data by locating a global minima in the parametric space (Guo et al., 2013, Lovell et al., 2004). The optimisation routine was a custom written MATLAB script (MathWorks). The ODE15s function in MATLAB was used to solve the differential equations of the generic ionic model. Figure 4.2 illustrates a simplified flow chart of the optimisation process. Here we briefly cover the steps involved:

4.5.1 Initialisation

Initial parameters necessary for optimisation include weight functions, model parameters, and initial values. Here we cover the parameters that were initialised at the beginning of each optimisation run. Note that many of these parameters had to be manually adjusted between optimisation cycles. Initial model parameters were based on previous rabbit atrial single cell models by Guo et al. (2010).

The parameters dictating the behaviour of the ionic currents and membrane potential were placed under the control of the optimisation routine and were very rarely changed manually. For this thesis, a total of 26 model parameters were

optimised using our minimisation routine. Below we list the parameters that were under the direct control of the researcher:

- Initial conditions of model variables ($V_m, p_1, p_2 \dots$)
- Parameter upper and lower limits
- Initial weight function
- Tissue conductivity

Initial conditions were set by extracting variable values from a previous optimisation iteration. Usually, these values were obtained from a location near or at the resting membrane potential and at a time long after model initiation to ensure the computation had reached steady state. Parameter limits were set initially and were not altered in this thesis: the values were selected to reflect physiological ranges (Table 4.1). The initial weight function was changed at the beginning of each optimisation routine to encourage the fitting of a region of interest such as the phase 0 upstroke or phase 4 depolarisation. Weight was allocated to a region that was most important and a lower, or zero, value was assigned to sections of lesser importance. Tissue conductivity was manually changed at the beginning of an optimisation routine. To ensure activation, we began at a low conductivity and continually optimised while increasing the conductivity up to the desired level. This desired point was selected to match the conduction velocity in the tissue-based model to experimental results.

The parameter upper and lower limits were also used to transform the constrained parameters into unconstrained ones (Lovell et al., 2004). These unconstrained parameters were then used in the minimisation method, the constrained parameters are presented in (Table 4.1). The method for converting constrained parameters to unconstrained parameters is not discussed here (Fletcher, 2013, Lucidi, 1988).

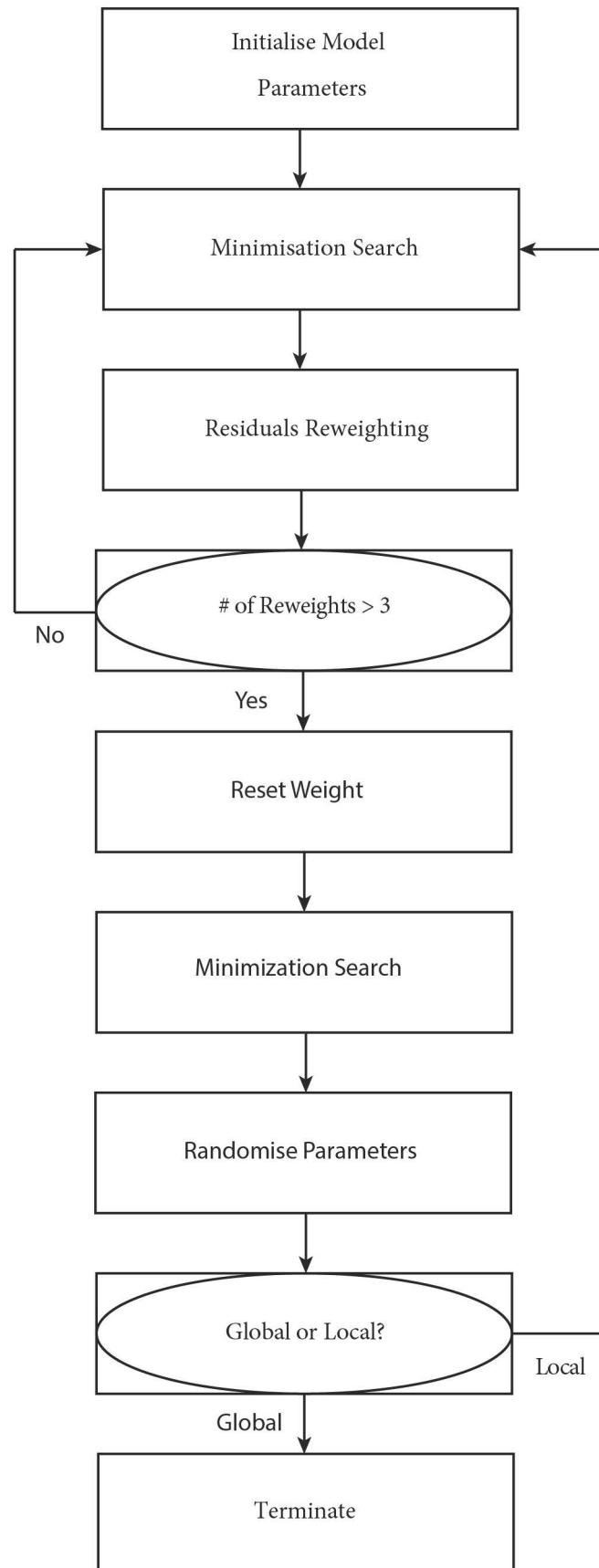


FIGURE 4.2: Flow chart for non-linear least squares optimisation.

TABLE 4.1: Upper and lower limits for model parameters

	Parameter	Current 1	Current 2	Leakage	Units
Lower limits	\bar{g}_j	0	1000	1.4	$\mu\text{S}\cdot\text{cm}^{-2}$
	$E_{rev,j}$	-100	10	-60	mV
	$k_{\alpha pj}$	0	0	NaN	s^{-1}
	$s_{\alpha pj}$	-0.2	-0.2	NaN	mV^{-1}
	$k_{\beta pj}$	0	0	NaN	s^{-1}
	$s_{\beta pj}$	0	0	NaN	mV^{-1}
	$E_{\alpha\beta pj}$	-81.3	-60	NaN	mV
	$k_{\alpha qj}$	0	0	NaN	s^{-1}
	$s_{\alpha qj}$	-0.2	0	NaN	mV^{-1}
	$k_{\beta qj}$	0	0	NaN	s^{-1}
	$s_{\beta qj}$	0	-0.2	NaN	mV^{-1}
	$E_{\alpha\beta qj}$	-81.3	-81.3	NaN	mV
Upper limits	\bar{g}_j	1000	10000	10000	$\mu\text{S}\cdot\text{cm}^{-2}$
	$E_{rev,j}$	-80	100	-10	mV
	$k_{\alpha pj}$	5000	5000	NaN	s^{-1}
	$s_{\alpha pj}$	0	0	NaN	mV^{-1}
	$k_{\beta pj}$	5000	5000	NaN	s^{-1}
	$s_{\beta pj}$	0.2	0.2	NaN	mV^{-1}
	$E_{\alpha\beta pj}$	9.6	-50	NaN	mV
	$k_{\alpha qj}$	5000	5000	NaN	s^{-1}
	$s_{\alpha qj}$	0	0.2	NaN	mV^{-1}
	$k_{\beta qj}$	5000	5000	NaN	s^{-1}
	$s_{\beta qj}$	0.2	0	NaN	mV^{-1}
	$E_{\alpha\beta qj}$	9.6	9.6	NaN	mV

4.5.2 Minimum searching and curvilinear gradient optimisation

Each iteration, the search for a local least-squares minima was based on the Brent's line minimisation method (Brent, 2013). This method provides the advantages of both the parabolic step and golden step. The curvilinear gradient routine benefits from both Newton and steepest descent methods. It has been shown to be especially beneficial among systems having a large parameter space (Lovell et al., 2004).

4.5.3 Weighted residuals

We dynamically smooth the searching surface through an iterative reweighting system to assist the optimisation routine to find the global minimum. In this way we avoided the inherent limitations of gradient-based methods, namely that they terminate upon locating a local minima. After a given number of iterations, the weighting vector was reset to its original user-defined value to determine whether the iterated weighting was beneficial or not.

4.5.4 Parameter randomisation

After resetting the weight function to its original value, the unconstrained parameter space was perturbed. This perturbation vector was a normally distributed random variable with a mean of 0 and a standard deviation, σ , with typical value $\sigma = 0.01$. The standard deviation was iteratively altered and reapplied until the objective least squares cost function was improved.

4.5.5 Condition of termination

The goal of the optimisation and minimisation protocol was to reduce the objective cost to zero. However, due to limitations such as machine precision and

numerical round-off errors it was not possible to perfectly match the model to the data. Therefore, we set a threshold value to determine when an acceptably small objective cost function had been achieved, and terminated the optimisation once this goal was met. In this thesis we define the objective cost function as the root mean square (RMS) error between the model AP and the recorded AP data. The threshold value varied with complexity and noise properties of the time series data, but overall a threshold value of 2.5-5 mV was accepted as a good fit.

4.6 Network modelling

A network model was implemented to simulate the tissue level optical recordings (Van Capelle and Durrer, 1980). The model was implemented using the method of lines whereby the spatial derivative was solved using a finite difference method and the temporal components were solved using the MATLAB ODE15s suite.

Figure 4.3 illustrates a simplified cable system for modelling the electrical activity in excitable cells. Each cell has a connection between the intracellular and extracellular space, and incorporating a number of ionic currents, collectively termed i_{ion} , passing through a variable resistance (representing the gates) and a capacitance C_m . The first cell in the figure is outlined by a red dashed box. Each cell is connected to at least two other cells by an internal resistance R_i and the extracellular space is deemed to be at the same grounded potential at all points.

From Figure 4.3 we can derive the cable equation that defines the mathematical model for the single cell and one-dimensional preparation. The equation for the membrane potential at node V_k is given by the finite difference approximation of the second spatial derivative in combination with the usual time dependent membrane potential activity. The formulation is:

$$i_m = C_m \frac{dV_{m,k}}{dt} + i_{ion}, \quad (4.1)$$

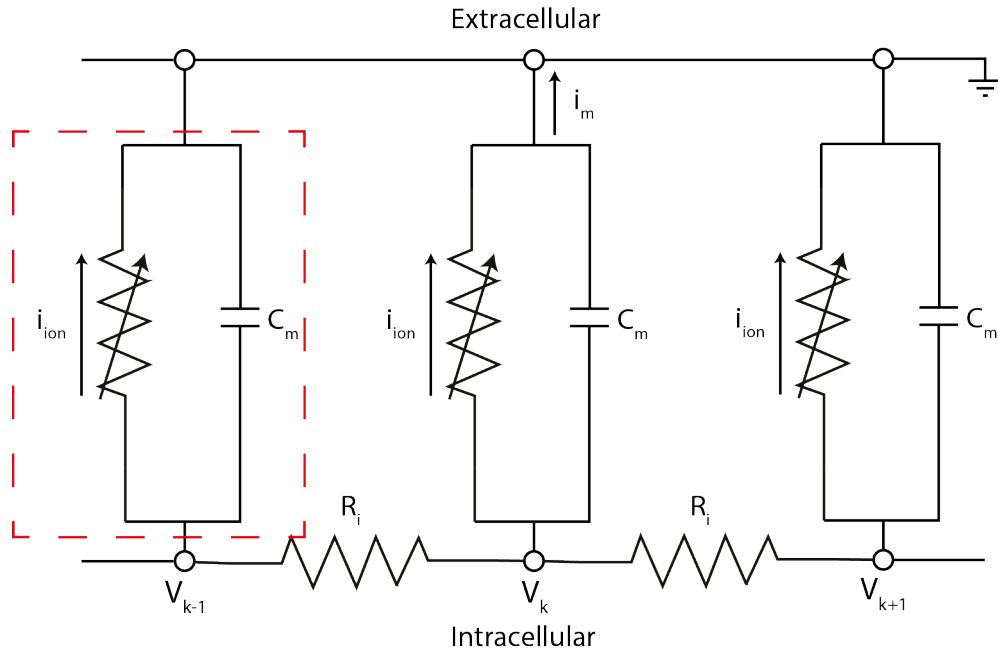


FIGURE 4.3: Simplified cable formulation for computational model

when factoring in the finite difference equivalent of the spatial derivative we obtain:

$$g_1 (V_{m,k-1} - V_{m,k}) + g_2 (V_{m,k+1} - V_{m,k}) = C_m \frac{dV_{m,k}}{dt} + i_{ion}. \quad (4.2)$$

We see the two-dimensional equivalent in Figure 4.4: in this case the node of interest has four neighbours as opposed to two with the relevant formulation is as follows:

$$g_1 (V_1 - V_{m,k}) + g_2 (V_2 - V_{m,k}) + g_3 (V_3 - V_{m,k}) + g_4 (V_4 - V_{m,k}) = C_m \cdot \frac{dV_{m,k}}{dt} + i_{ion}, \quad (4.3)$$

where C_m is the membrane capacitance, g_n is the conductivity between the n -th neighbouring node and the node of interest, and V_n is the membrane potential at the n -th node, equivalent to $V_{m,k}$ at the k -th node in this model as the extracellular space is grounded.

The network model layout is shown in Figure 4.5, where 4.5a) represents the network model used in this thesis, namely the monodomain formulation, whilst

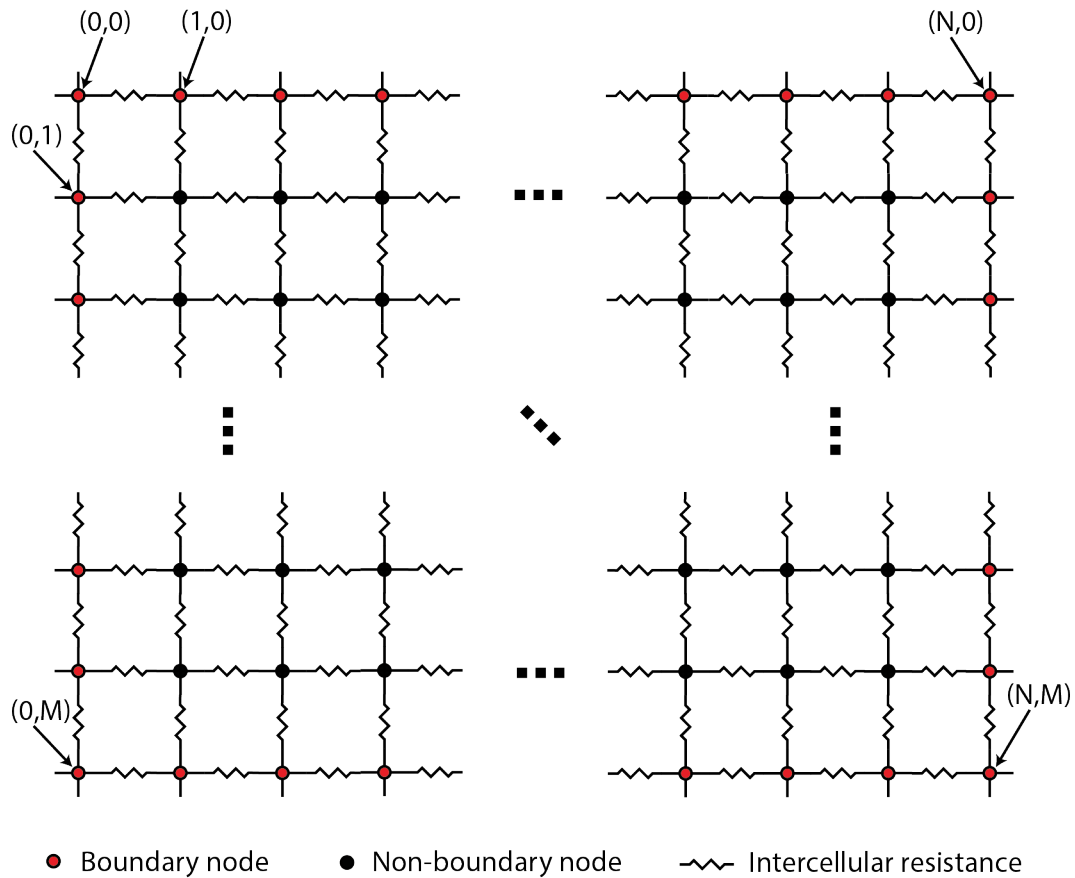


FIGURE 4.4: Model layout illustrating two-dimensional connections by intercellular resistances

4.5b) illustrates the bidomain implementation, and is included for completeness but is not used in this thesis.

4.6.1 Optimisation of tissue-based model

The two-dimensional network model optimisation used the same routine as the single-cell method. The model was optimised to fit two attributes, electrical AP waveshape and CV. We fitted model APs to non-pacemaking APs by selecting the centre most node of the 2D tissue model in order to avoid edge effects from the boundaries. The conduction velocity was manually adjusted by iteratively changing the value of the node-to-node tissue conductivity from zero to the desired value. Cell ionic parameters were further optimised for each new value of tissue conductivity to provide accurate fits to AP waveshape.

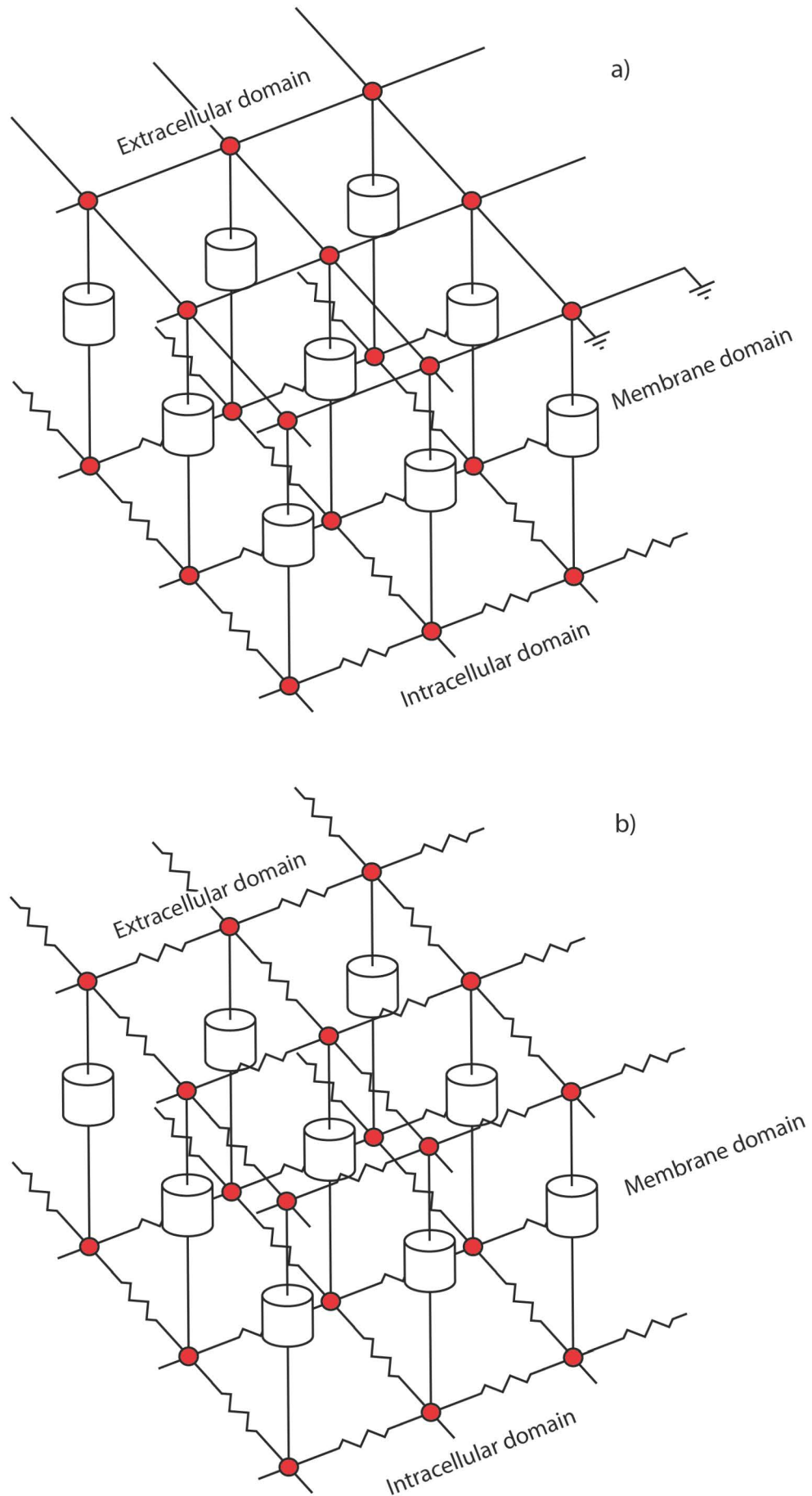


FIGURE 4.5: Simplified cable formulation illustrating the network model in three dimensions

Each model node represented a pixel of the processed spatially-averaged optical data: in this way we were able to match the 2D activity of the model to the experimental observations. Post-processing each pixel represents approximately 3.15 cells, at 4X optical magnification. Initial optimisation was performed using a smaller model of 30x20 nodes to limit the computational time. At higher node counts the finite difference method became computationally expensive and a finite element solution would be preferable. As such, initial work was completed on a subset and was confirmed in an appropriately sized preparation post-optimisation.

4.7 Programming

Two major programming languages were used in this thesis: Matlab (R2012a, The Mathworks) and Python. Python (version 2.7.5, www.python.org), NumPy (version 1.7.1, www.numpy.org), SciPy (version 0.12.0, www.scipy.org), Matplotlib (version 1.2.1, www.matplotlib.org), and TiffFile (version 2013.05.02) were all used in this thesis. Matlab was primarily used for computational modelling and optimisation, the single cell and network models were created in Matlab and solved with an in-built ODE solver (ODE15S). Python, and its counterparts, were used for experimental visualisation and analysis of electrical and optical data.

Chapter 5

HL-1 monolayer results

5.1 HL-1 cell line characteristics

The HL-1 cell line is derived from an AT-1 subcutaneous tumour removed from a C57BL/6J laboratory mouse. It has been shown to contain many of the traits of adult cardiomyocytes in culture and was the first available cell line to maintain a contractile phenotype. A HL-1 culture forms a syncytium of gap-junction connected cells that are spontaneously active, both electrically and mechanically. Cultures have been shown to contain gap junction proteins, Cx30, Cx43 and Cx45; ion currents typical of pacemaking and atrial cells, i_f , i_{Ca} , i_{Kr} ; highly-organised sarcomeric structures for contraction; as well as pacemaking and non-pacemaking cells representative of in-tact atrial tissue (Claycomb et al., 1998, Sartiani et al., 2002, White et al., 2004).

Confluent HL-1 cultures provide an approximately homogeneous cell monolayer for experimentation. This format was easy to optically image and is free from structural heterogeneity found in ex-vivo tissue samples, enabling a clearer analysis of cell-cell interaction in electrically active cardiac preparations. Further, the HL-1 cells provide a representation of both pacemaking and non-pacemaking myocytes, distinguished by the presence/absence of a phase 4 slow depolarisation, which can be investigated in isolation or as a confluent syncytium (Sartiani et al., 2002).

Finally, the HL-1 cell line is considered to have a homogeneous cell population for passages above 30 (Claycomb et al., 1998). These attributes of the HL-1 cell line allow the explicit study of interactions between pacemaking and non-pacemaking atrial cells. Overall, HL-1 cells provided a good platform for the investigation of wave interactions in a cardiac syncytium, lending itself to their modelling, in order to extract information about the fundamental drivers of arrhythmias and other physiological and pathophysiological states.

5.2 Optical analysis

Potentiometric dyes such as di-4-ANEPPS are known to have various spectral properties when exposed to different biological preparations (Loew et al., 1992). Furthermore, the maximum membrane potential sensitive spectral shift of di-4-ANEPPS is 10%, a 2-5 nm blue shift in the emission profile Bachtel et al. (2011). In order to visualise these effects, we collected the single-photon excitation spectra for di-4-ANEPPS in HL-1 cells.

5.2.1 Optical properties of di-4-ANEPPS in HL-1 cells

The emission spectra for di-4-ANEPPS was captured with a 488nm excitation laser on a Leica SP5 confocal microscope using the Lamda scan mode (Figure 5.1). As noted in Chapter 4, Lamda scan mode excites the sample at a specific wavelength while stepping through emission filter wavelengths in 5 nm intervals to provide a piecewise emission spectra. Live cells were exposed to di-4-ANEPPS solution (5 μ M) for 10 minutes and maintained in Claycomb medium throughout the process at 35–37°C. The data was fitted to a skewed Gaussian curve (Equation 5.1) using the Scipy curve fitting algorithm. Peak wavelength was 595nm. The equation describing the skew normal distribution is given by:

$$y = \frac{a}{(\sigma\sqrt{2\pi})} \exp\left(\frac{-(x-\mu)^2}{2\sigma^2}\right) \left(1 + \operatorname{erf}\left(\frac{\alpha(x-\mu)}{\sigma\sqrt{2}}\right)\right) + c \quad (5.1)$$

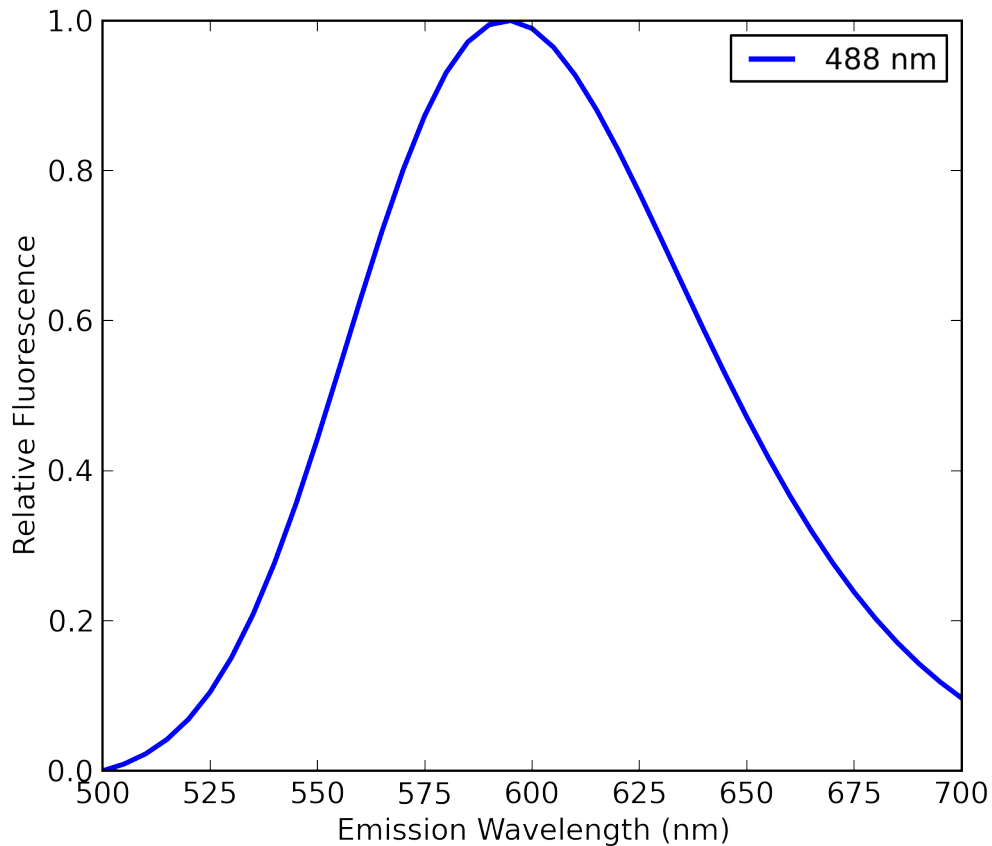


FIGURE 5.1: Emission spectra of di-4-ANEPPS in HL-1 cells with 488 nm excitation captured on a Leica SP5 in Lamda scan mode. Cells were maintained at 35 – 37°C in Claycomb medium. The spectra was normalised in the 500-700nm region.

with standard deviation $\sigma = 62$ nm, mean $\mu = 561.5$ nm, skewness variable $\alpha = 2.12$, offset value $c = 1.21$ nm and scale value $a = 1.21$.

In this study we were most interested in the red wing of the emission spectra (> 600 nm) as the optical system was unable to record ratiometric activity when using the camera for epifluorescence. Figure 5.1 presents the normalised fluorescence intensity. Increases in membrane potential blue-shift the di-4-ANEPPS emission spectra, and we therefore observed a reduction in fluorescence when recording OAPs. In this thesis, OAP data was inverted to conform with the traditional AP morphology, unless otherwise specified.

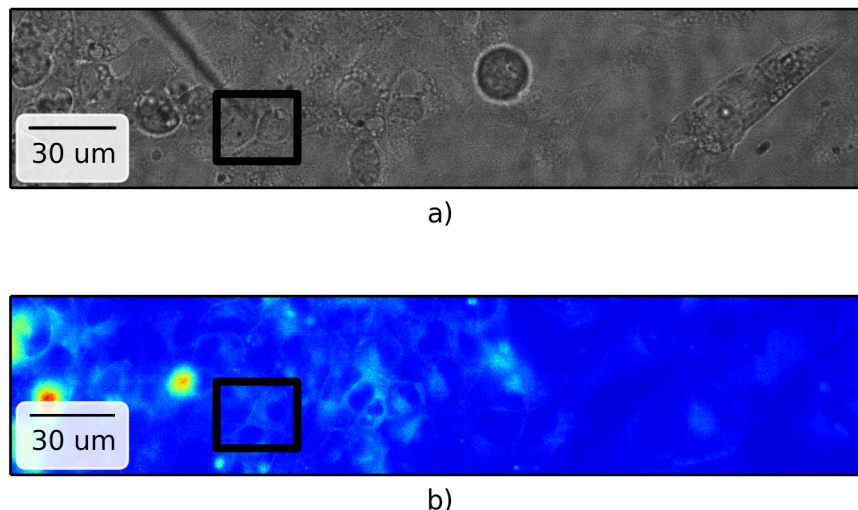


FIGURE 5.2: Images of impaled cell in a) brightfield illumination and b) fluorescent illumination. The fluorescent illumination b) was used to compare optical to electrical signals of membrane potential in Figure 5.3. The brightest parts of b) are most likely dead cells or cell debris and typically show no sensitivity to membrane potential. b) represents the unprocessed raw fluorescent data captured by the camera. The black box corresponds to the optical region of interest for electrical-optical comparison in Figure 5.3.

5.2.2 Optical-electrical equivalence of di-4-ANEPPS

We experimentally confirmed that changes in fluorescence, due to spectral shift of the di-4-ANEPPS molecule, corresponded to changes in membrane potential (Figures 5.2 and 5.3). Figure 5.2a) shows the brightfield illuminated image of HL-1 cells using a 40X water dipping Olympus objective: one cell was impaled with a 50-100 $M\Omega$ sharp micro-electrode filled with 3M KCl. The sharp micro-electrode can be seen on the left of the figure as an out of focus dark line. Figure 5.2b) presents the raw fluorescent image at a single time instant, showing the outline of some cells. The large red signals on the left of the image corresponded to electrically inactive cells or cell debris.

We saw a good correspondence between the acquired optical and electrical data (Figure 5.3). The cellular electrical activity was spontaneously driven by an initiation site at another location in the culture. The electrical recording was triggered

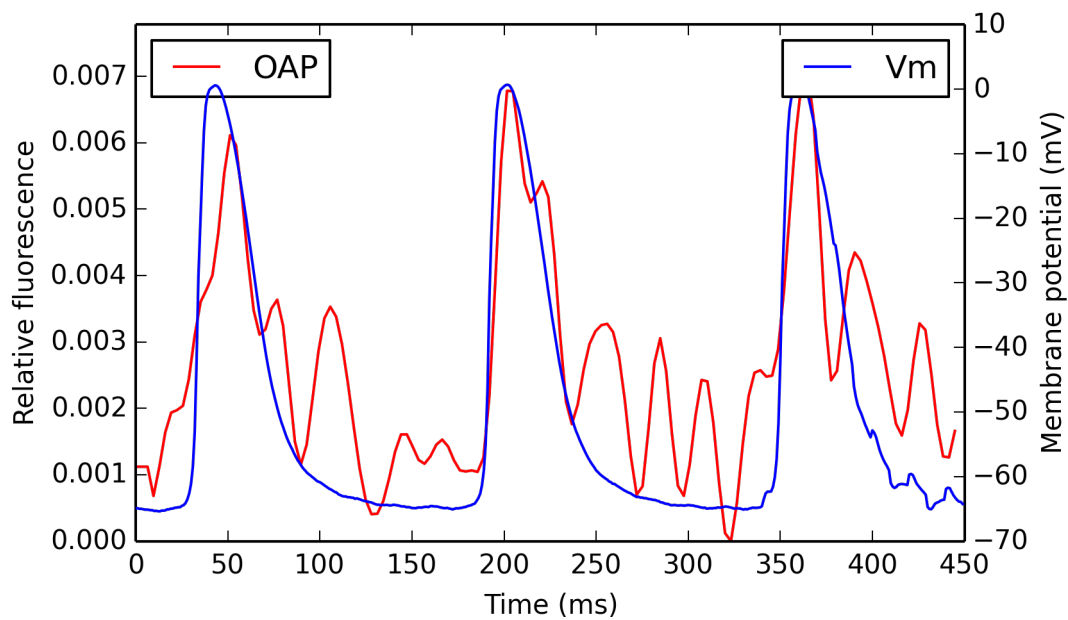


FIGURE 5.3: Optical and electrical action potential comparison in the same cell, corresponding to images captured in Figure 5.2. The OAP is represented as $\Delta F/F$. Optical data recorded at 312 FPS and electrical data at 10 kHz.

from the CMOS camera such that when the camera recording was enabled, the sharp electrode was concurrently triggered to record. The baseline was unsteady and will be further analysed in the discussion.

5.3 Electrical action potential data

We investigated the cell types present in the HL-1 culture as differentiated from characteristics of the electrically-recorded AP waveshape. For the purposes of modelling, it was important to identify the various cell types present to faithfully reproduce the activity of the cells computationally.

5.3.1 Cell types in the HL-1 cell line

Using sharp microelectrodes, APs from a number of HL-1 cells were recorded in an electrically active syncytium. The sharp microelectrodes were made from borosilicate glass pulled by a Sutter P-97 micropipette puller, and exhibited a

resistance of 50-100 M Ω when filled with 3M KCl. Cells were maintained at 32 – 35°C during experimentation and were contractile throughout.

Two cell types were identified from the characteristics of their membrane potential (V_m) wave shape (Figure 5.4).

- Type a) consisted of a baseline with a phase 4 slow depolarisation typical of pacemaking cells: this type will be known as the pacemaking type (Figure 5.4a)).
- Type b) produced a slowly repolarising phase 4 baseline that stabilises before the following AP (Figure 5.4b)). This type also exhibited a faster phase 0 depolarising upstroke than Type a). Type b) was referred to as the non-pacemaking or atrial cell type.

5.3.2 Cell distribution in the HL-1 cell line

During the course of the experiments, cells were randomly selected for sharp micro-electrode recording (N=20 over 5 experiments). Typically recordings were taken to confirm normal physiological activity; however, this data can also be used to infer cell distributions. We observed that 70% of cells exhibited phase 4 slow depolarisation (Figure 5.4a)), while the other 30% were characterised by a stable phase 4 membrane potential (Figure 5.4b)). These results suggested that a typical culture was represented by 70% pacemaking cells and 30% non pacemaking.

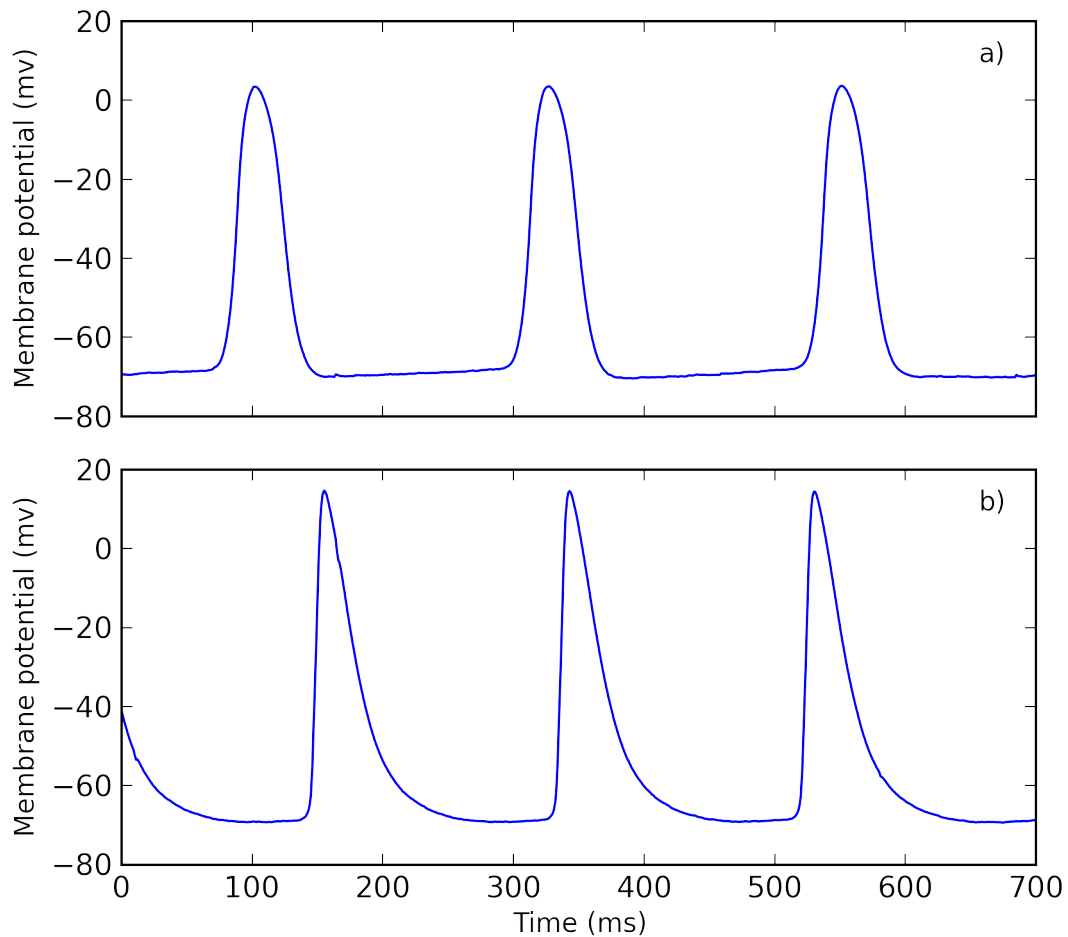


FIGURE 5.4: Sharp microelectrode recordings of two cell types found in HL-1 preparations. a) illustrates a cell with pacemaking characteristics while b) shows no pacemaking capacity. On average, contractile frequency was 4.1 ± 1.3 ($\mu \pm \text{SD}$) beats per second (BPS).

5.4 Optical action potential propagation

This section presents optical activation data acquired in healthy confluent HL-1 preparations maintained at $32 - 35^\circ\text{C}$ and superfused with Tyrode's medium. AP wavefronts and rotor systems were captured. In all circumstances, activation of the preparation was believed to be governed by a stable re-entrant rotor system. We investigated a number of characteristics of the electrical activity in order to extract information for optimisation of the computational model. All optical data was low pass Butterworth (third order) filtered at 50 Hz, unless otherwise specified.

Two-dimensional fluorescent data will be typically presented as a post-processed

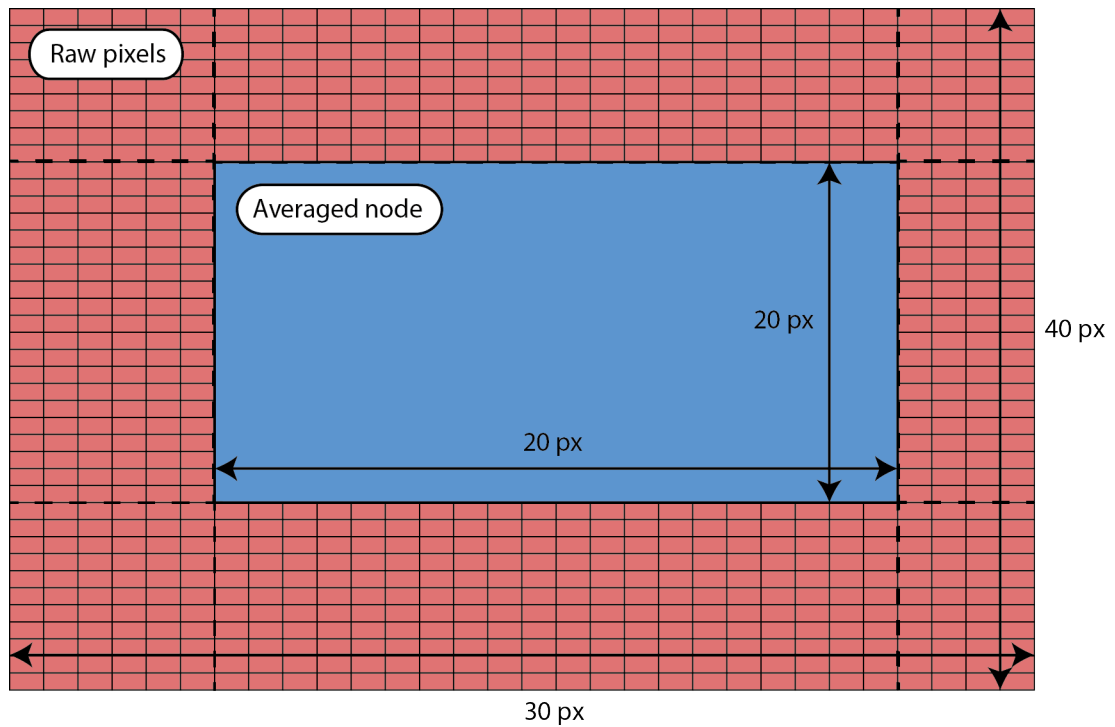


FIGURE 5.5: An illustration of spatial averaging used when processing raw optical image data. Each red box represents a raw pixel in the camera capturing optical data, the large blue box in the centre is the average of a 20x20 pixel region. Spatial averaging of 20x20 pixels is commonplace in this thesis.

TABLE 5.1: Linear wavefront 50% wave-width

Sample	Wave-width (μm)
One	378
Two	494
Three	399

spatially-averaged image. Each pixel of the spatially-averaged image represents a $X \times Y$ square of pixels in the raw data (Figure 5.5). This is equivalent to binning the data. Typically, raw data in this thesis was spatially-averaged from 20 x 20 squares of pixels, this spatial average is represented henceforth as x-y Y, where Y represents the number of pixels averaged per square. Figures 5.5, 5.6 and 5.7 illustrate x-y 20 spatially-averaged data.

TABLE 5.2: Spiral 50% wave-width

Sample	Wave-width (μm)
One	362
Two	268
Three	472

5.4.1 HL-1 OAP characteristics

Overall, experimental contractile frequency was 4.1 ± 1.3 BPS, while conduction velocity was 1.8 ± 0.7 cm/s when superfused with Tyrode's at $32 - 35^\circ\text{C}$. The contractile frequency and conduction velocity are presented as mean \pm SD. A minimum of three APs were utilised for each recording with a total of $N=26$ recordings from four different preparations. These values may be temperature dependent: contraction at up to 8 bps was recorded under warm conditions ($37 - 39^\circ\text{C}$). It is worth noting that these warm temperatures were sustained over 12 hours and did not kill the cells nor seem to deter proliferation.

5.4.2 Optically recorded wavefronts

Figure 5.6 illustrates a propagating wavefront from the right to the left of the field of view in one HL-1 preparation. The half amplitude wave-width of the OAP was $340 \mu\text{m}$. Activation frequency was 3.71 bps, with conduction velocity 1.47 cm/s. The data were captured at 272 FPS and was spatially averaged as x-y 20. The raw data was captured as a 1280×800 pixel image, and is presented as normalised $\Delta F/F$.

5.4.3 Optically recorded rotors in HL-1 monolayers

Figures 5.7 and 5.8 present fluorescent and contour maps of a rotor system captured in the same culture. The data was captured at 272 FPS and was spatially-averaged as x-y 20. At 272 FPS it was not possible to capture the entirety of

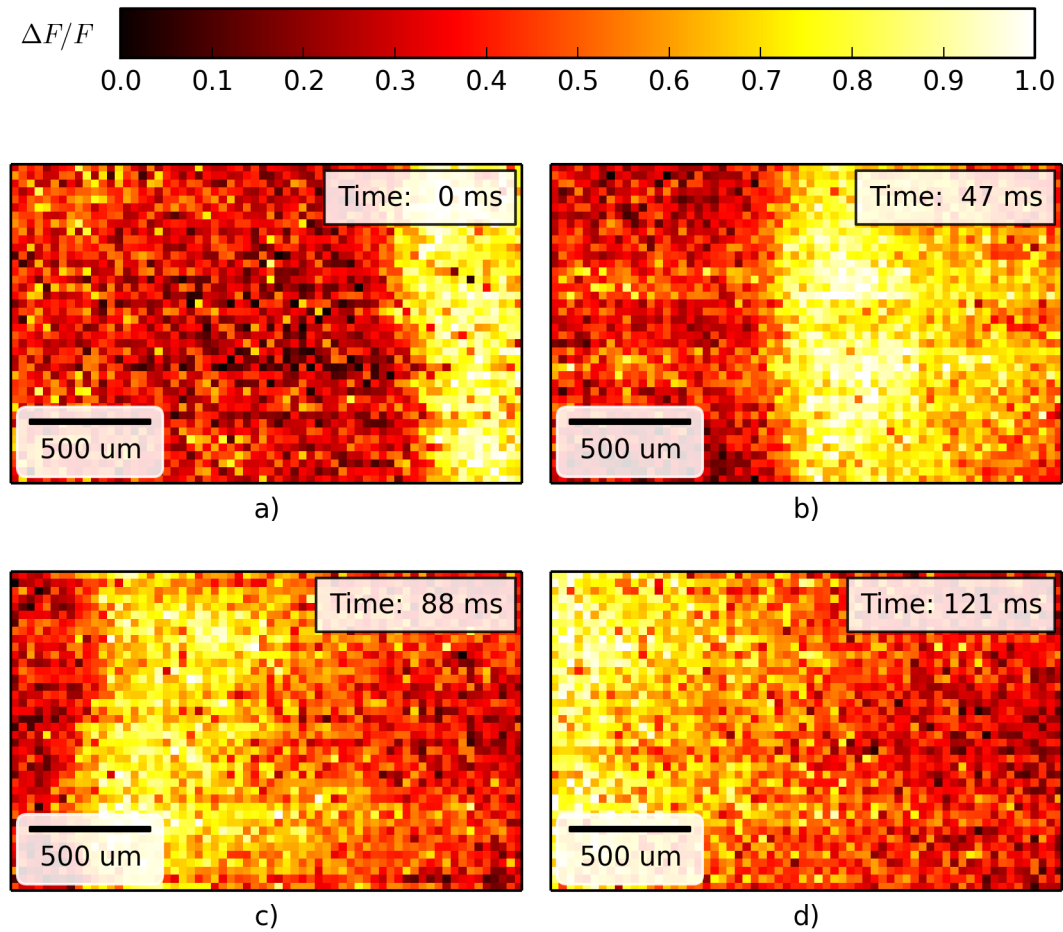


FIGURE 5.6: A propagating OAP wavefront. Time is presented in milliseconds in the top right corner of each frame. OAP wave-width was $340 \mu\text{m}$.

the rotor system because of readout and optical limitations inherent in the CMOS camera and microscope. The raw data was a 1280×800 pixel region of interest.

The rotor of Figures 5.7 and 5.8 exhibited an activation frequency of 4.1 bps and conduction velocity of 1.5 cm/s , the OAP 50% wave-width was $425 \mu\text{m}$. The spiral progression was approximately linear with respect distance from to the origin and the rotation angle, θ , as presented later in Figure 5.12 (Line 0). The rotor is not completely represented in Figure 5.7 and so the spiral activation wavefront does not extend out to 360° .

We examined activation at the approximate centre of the rotor and found a region of low optical activity, corresponding to an area of low electrical activity

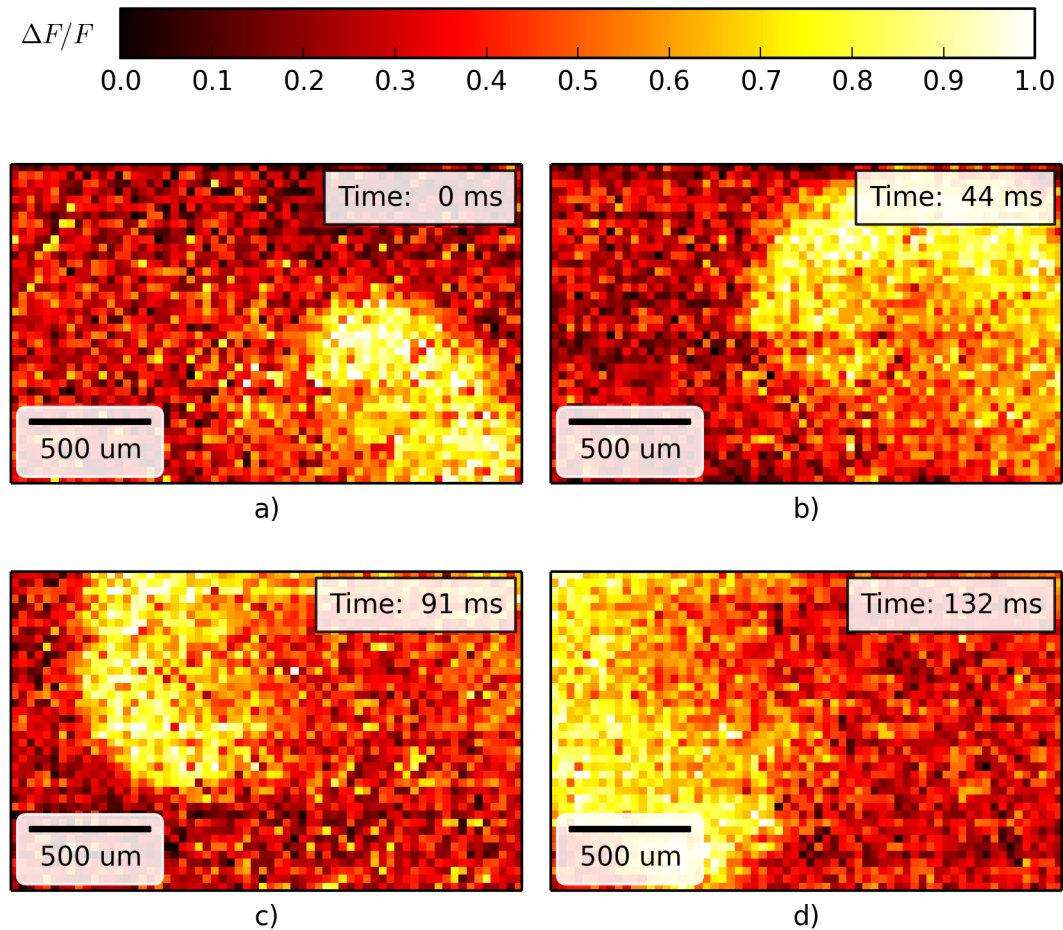


FIGURE 5.7: Fluorescent image of a rotor system in HL-1 preparation. Captured at 272 FPS. The colour bar maps blue to the lowest point in the OAP and red to the highest. Elapsed time is given in seconds in the top right of each sub-figure.

(Figure 5.9). Conversely, the outer wings of the rotor (Figure 5.10) exhibited relatively consistent OAPs typical of a region with periodic electrical activity. This trend of null activity at the centre of optically mapped rotors was a feature of all rotors visualised ($N=5$).

An example spiral activation wavefront is presented in Figure 5.11. Noise was an impediment when selecting the centre of the rotor: the centre is difficult to determine and as a result is arbitrarily selected. In all cases, we selected the centre-most point of the leading edge of the spiral wavefront. The spiral progression was calculated on three different rotors and recreated with a line of best fit of radius against rotational degrees: we then calculated the mean and standard deviation

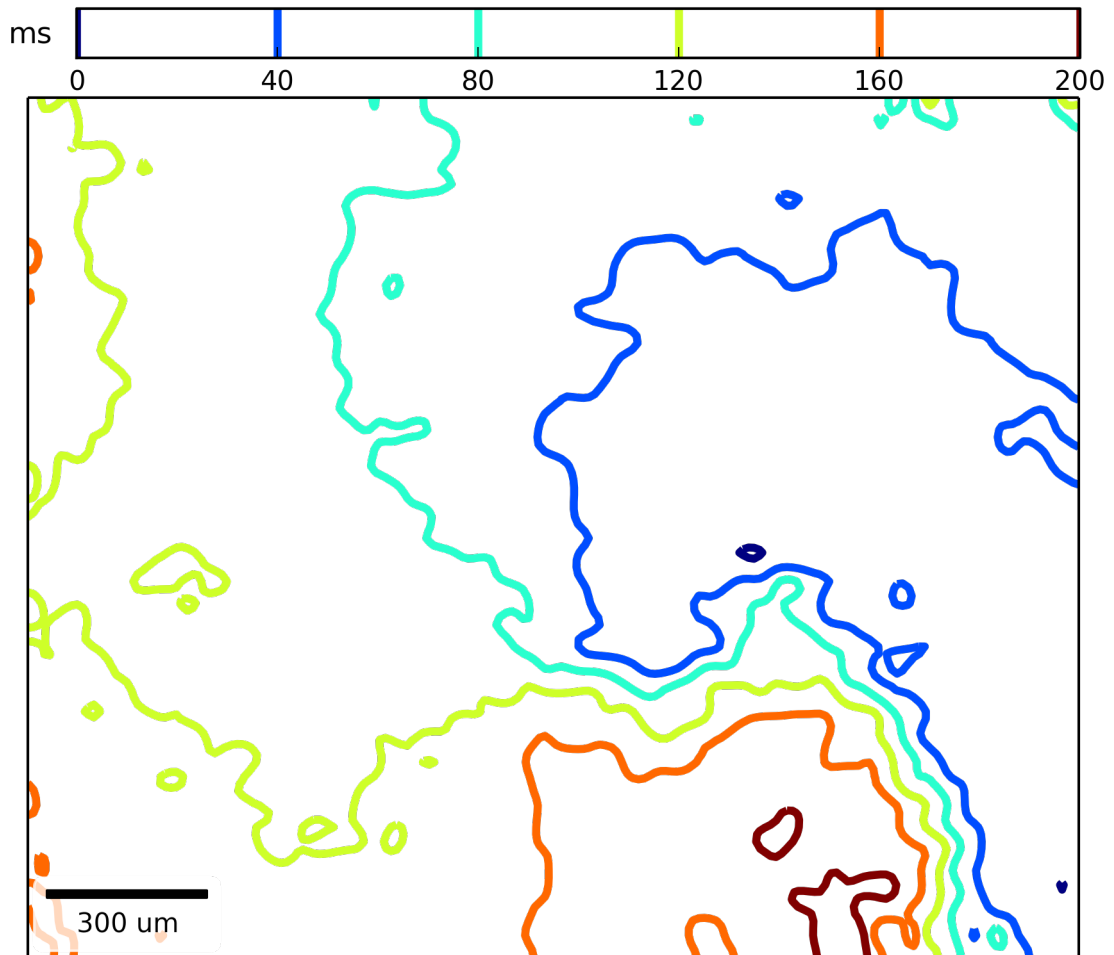


FIGURE 5.8: Contour map of a rotor system in HL-1 preparation, captured at 272 FPS, using data in Figure 5.7. The colour bar at the top of the figure maps colour to activation time, blue being the earliest and red/orange being the latest.

of the three lines of best fit to represent the mean and standard deviation of curvature values. Below we present the parameters for the lines of best fit and the RMS error:

$$r = 11.76\theta + 233.84\mu m, \quad (5.2a)$$

$$r = 10.1\theta + 91.7\mu m, \quad (5.2b)$$

$$r = 7.8\theta + 134.9\mu m, \quad (5.2c)$$

where θ is in units of degrees, RMS error for each line of best fit was: a) 32.16 μm ; b) 47.7 μm ; c) 30.5 μm . The data enabled comparison between the shape

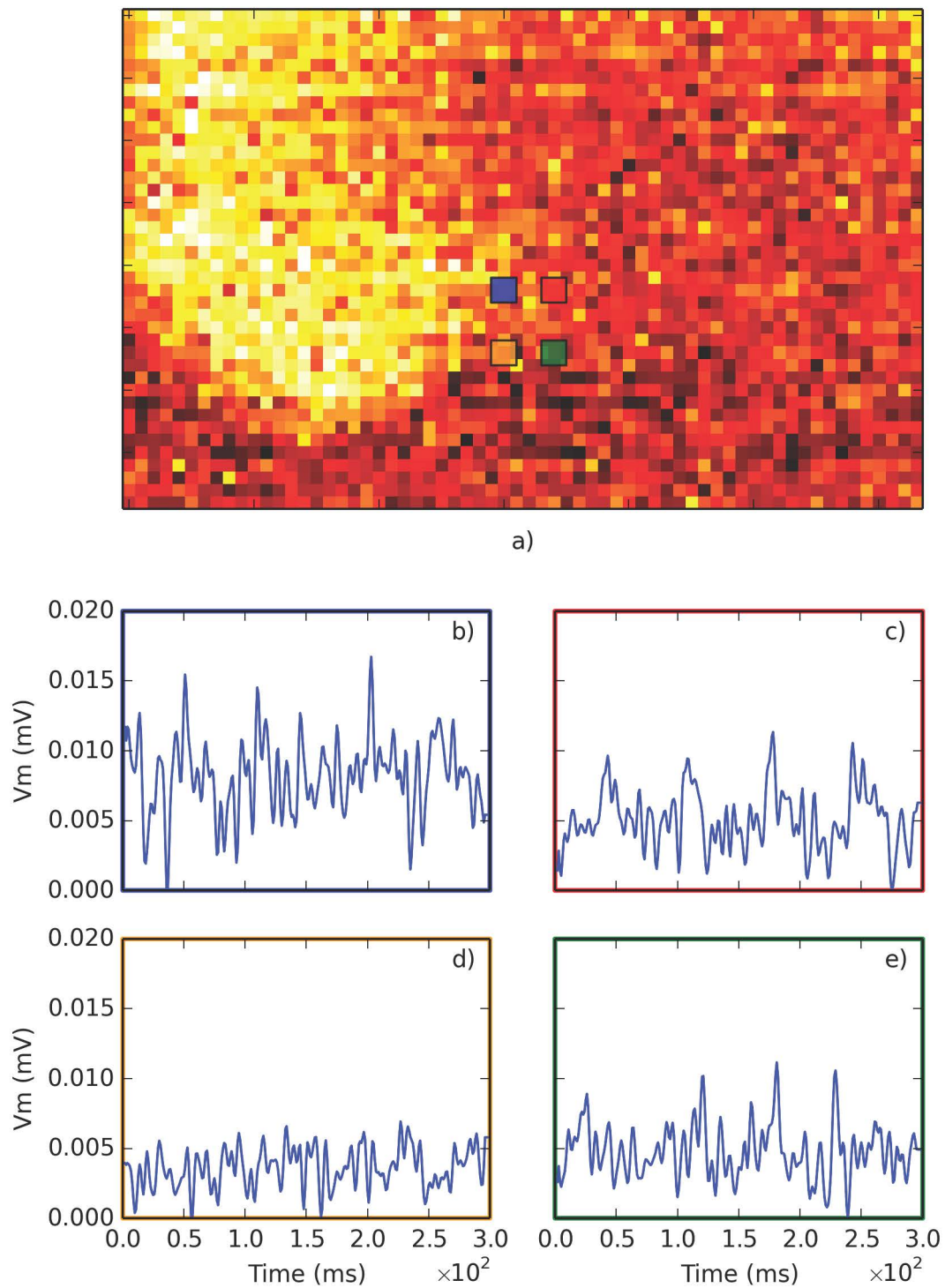


FIGURE 5.9: OAPs taken at various locations in the central-most region of the rotor. The data is presented as $\Delta F/F$ and was low pass filtered at 50 Hz. The array of points in a) correspond to the data presented in b), c), d) and e). The top-left point in a) is presented in b) and so on.

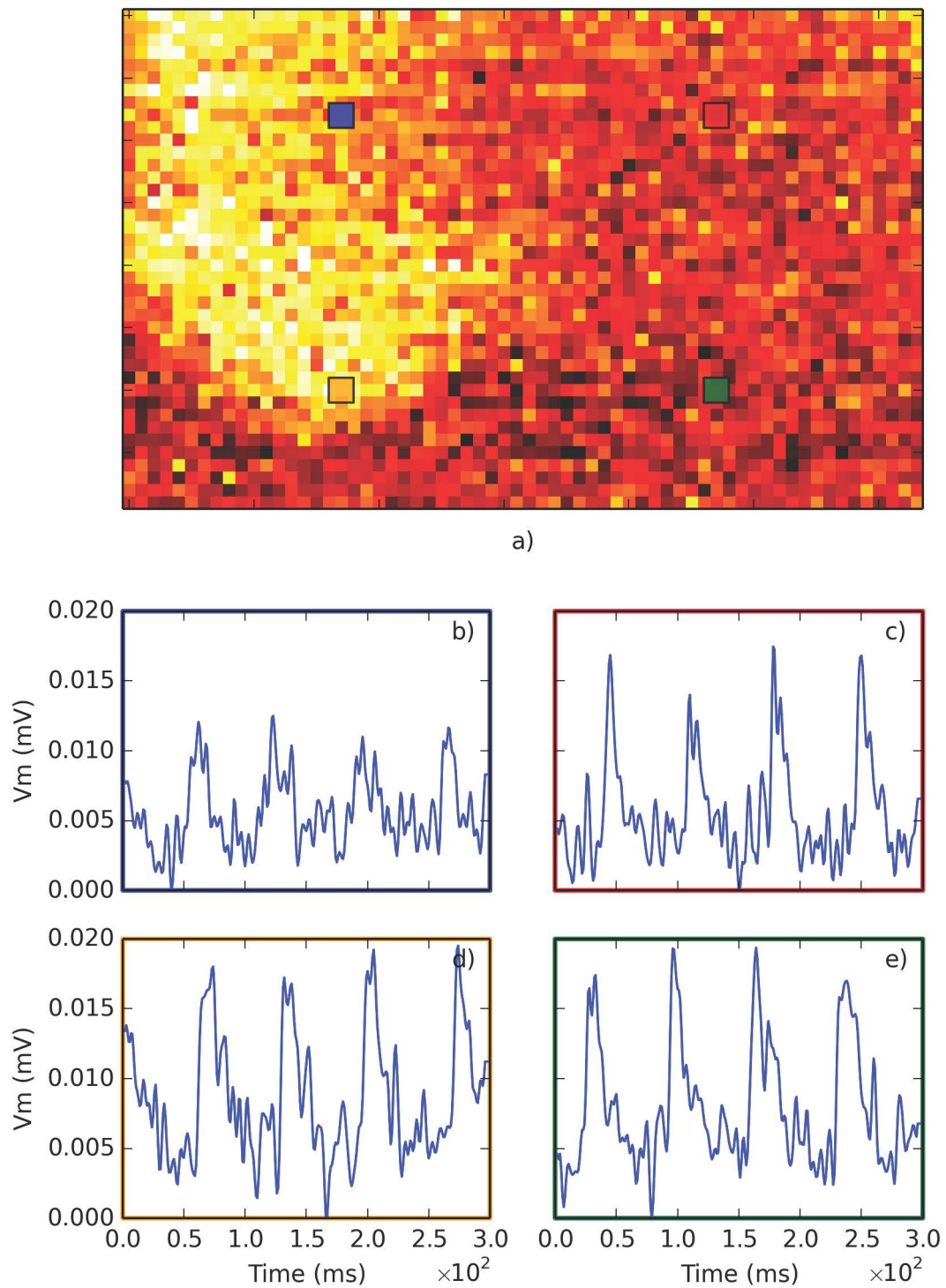


FIGURE 5.10: OAPs taken at various locations in the extremity of the rotor. The data is presented as $\Delta F/F$ and was low pass filtered at 50 Hz. The array of points in a) correspond to the data presented in b), c), d) and e). The top-left point in a) is presented in b) and so on.

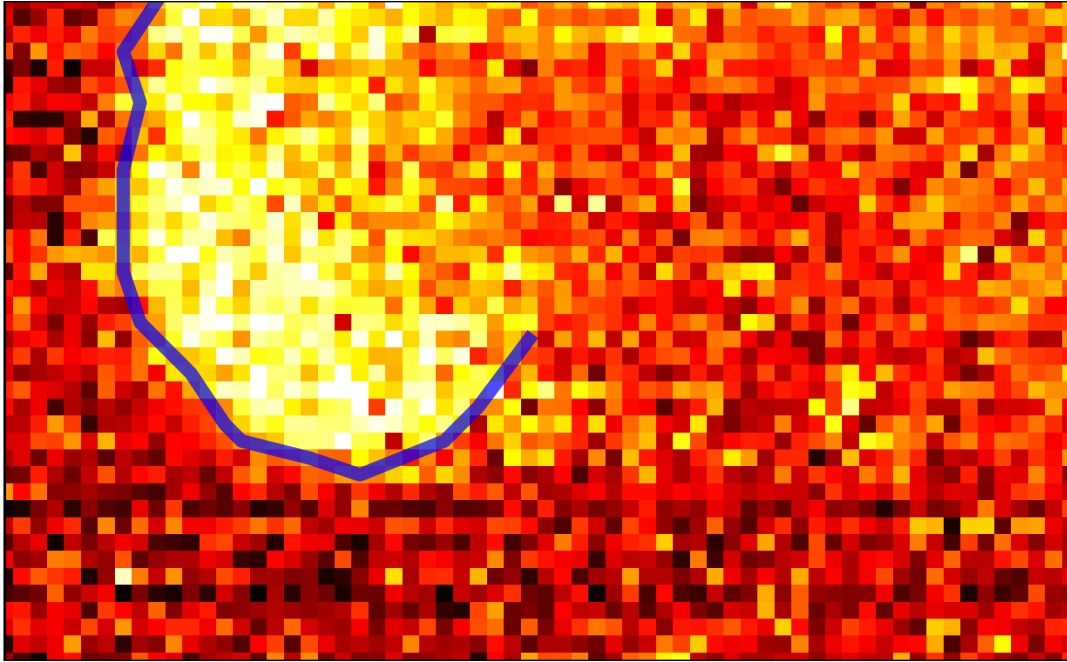


FIGURE 5.11: Rotor activity in an HL-1 monolayer with spiral progression overlaid. The blue line represents the approximate rotor activation wavefront calculated.

of the rotors found experimentally and those modelled computationally. We also examined the radius-angle relationship of three independent rotors as their mean and standard deviation (Figure 5.12), providing useful information for validation of our computational models. Further, the spiral progression provided information on the conductivity characteristics of the surrounding tissue. Namely, that the conductivity was approximately isotropic and that there weren't any structural or functional barriers to propagation in the field of view.

The HL-1 cell line has at least two distinct cell types: pacemaking and non-pacemaking cells. However, a monolayer connected as a syncytium was typically driven by an electrical rotor system akin to those seen in re-entrant arrhythmias. In all cases where the site of initiation was located ($N=5$), the source was a sustained electrical rotor, as opposed to a pacemaking region. We observed that the monolayer was highly prone to the establishment of rotors: cultures physically separated from the site of activation developed sustained rotors shortly after separation. In one such experiment, we physically separated a small sample of the monolayer in the centre of a larger sample. The original site of activation was

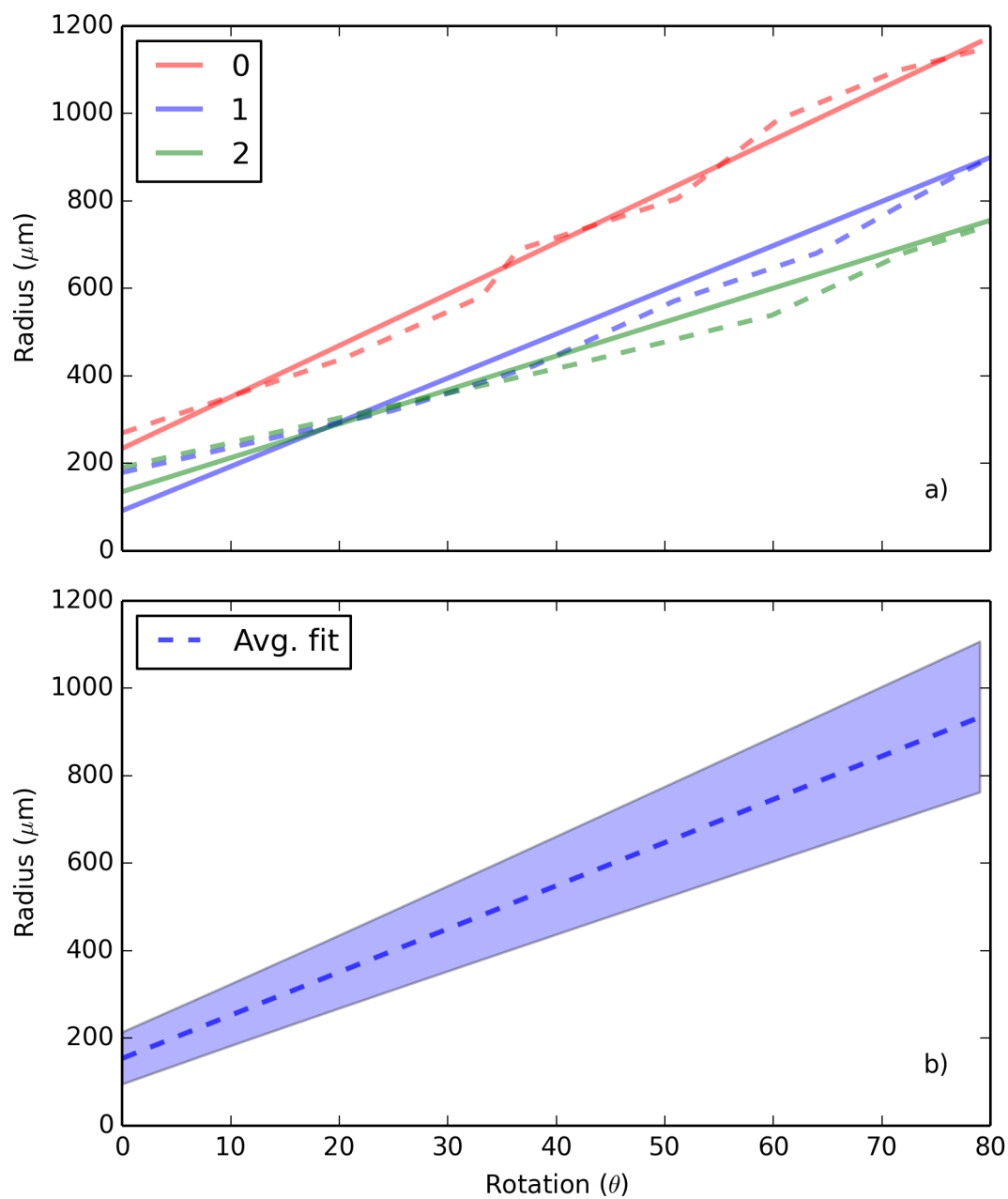


FIGURE 5.12: Radius-angle relationship of rotors seen experimentally. Radius is in μm and θ in degrees. a) presents results from three different rotors in HL-1 monolayers, with experimental data shown as dashed lines and the lines of best fit as solid lines. b) represents the mean of the three radius-angle relationships as a dashed line and the standard deviation with the shaded blue region, where the shaded area is one standard deviation.

located external to the central cell island and no electrical activity was seen inside the island. Within 30 minutes a rotor had established itself in the inner sample, independent of activity in the outer monolayer.

5.5 Discussion

5.5.1 Analysis of the emission spectra

We captured the emission spectrum for di-4-ANEPPS in HL-1 cells, which has not yet previously been reported. For validation purposes, we compared these results to published cardiac-based spectra since they have similar structure and electrophysiological properties. Furthermore, we also investigated trends in the wider literature. First, Laurita and Singal (2001) presented the emission spectra of di-4-ANEPPS in in-tact mouse hearts. They used an excitation wavelength of 515 nm and found a peak emission wavelength of 636 nm, this varied from our results but is likely due to the 515 nm excitation wavelength, we used 488 nm. Both the single- and two-photon emission spectra for rabbit ventricular tissue were presented by Dumas and Knisley (2005). Their single photon emission spectra was red-shifted, with a peak at 610 nm, compared with the HL-1 spectrum presented in Figure 5.1. Another study in rabbit ventricles found the peak emission spectrum to be approximately 640 nm for a 480 nm excitation wavelength (Knisley et al., 2000): the red-shift of peak emission compared to our results was probably due to the more negative resting potential in ventricular tissue. Further, emission spectra for resting membrane potential in various preparations tended to lie in the region between 600 and 630 nm for an excitation wavelength between 480 and 490 (Montana et al., 1989). Peak wavelength in our HL-1 preparations was 595 nm, comparable to that seen in the literature.

In our electrophysiological experiments we used a Tyrode's solution, but for capturing the emission spectrum we utilised Claycomb's media. A feature we considered was the effect of the different media on the emission spectrum. The exact

formulation of Claycomb's media in its current iteration is not known; however, a formulation published previously indicates it was based on DMEM with additional factors to assist growth (White et al., 2004). The formulations for Tyrode's and generic DMEM solution are provided below for comparison.

The Tyrode's formulation was (mM):

2 MgCl₂, 10 Glucose, 10 HEPES, 3 KCl, 2 CaCl₂ and 140 NaCl.

Typically, DMEM consists of (mM):

1.8 CaCl₂, 0.8 MgSO₄, 5.3 KCl, 44 NaHCO₃, 110 NaCl and 0.9 NaH₂PO₄ with varying amounts of Glucose.

The precise constituents of DMEM may vary between suppliers, with our formulation being from Sigma Aldrich who also supply the Claycomb media in its current iteration. We can see that the major difference lies in the concentration of NaCl, with an approximate 30 mM difference. Assuming the cells are stable, these values should not cause an appreciable shift in the resting membrane potential or the AP peak: the two major factors determining the di-4-ANEPPS potential dependent change in fluorescence. The emission spectrum captured in Figure 5.1 was a function of the time-weighted average of the peak and baseline membrane potential. The use of live cells provided us with a realistic environment in which to capture the emission spectra, but has the added complication that the spectra was continuously changing, as the cells were electrically active. A 100 mV shift in membrane potential results in a 2-5nm blue shift, or 10% change in fluorescence, in the emission spectrum (Bachtel et al., 2011). Under this assumption, and that the cells exhibit a membrane potential below -50 mV for more than half of their cycle period, we can take the emission spectra as approximately representative of the baseline emission spectra.

5.5.2 Limitations of the optical recording system

Even with a perfectly representative emission spectra, experimental acquisition is limited by filter selection: it is virtually impossible to obtain a filter/light source that exactly matches the desired wavelengths. The experimental work of this thesis was no exception: the filters used did not perfectly isolate the desired wavelengths. In our case, this resulted in a 20 nm discrepancy between achieved (with filters) spectral isolation and the blue end optimal wavelengths (600-610nm), negating the effects of inaccuracies in the captured emission spectra. The emission spectra was captured between 635-675nm: ideally the emission spectra should be maximised with a dichroic in the range of 600-630nm, and all longer wavelengths should be captured. Although this effect was not so detrimental as to prevent capture of the spectra, it certainly reduced the signal to noise ratio preventing capture of the spectra at the highest frame rates. HL-1 AP shape does not present a sharp phase 0 depolarising upstroke such as those seen in intact atrial and ventricular tissue. As a result, the higher frame rates were not necessary, but it may be relevant for future work where frame rates could approach 1 kHz, such as when imaging atrial AP upstrokes.

Analysis of the optical signal for this work was limited to the peak of the action potential, stemming from the use of a high speed camera with an unstable light source. At high speeds (200+ frames per second (FPS)) the flickering of the fluorescent lamp (Xcite 120Q) was recorded, with the lamp flickering at around 300 Hz. Flickering introduced a great deal of distortion to the OAP baseline. Typical frame rates were in the range of 270-330 FPS and utilised a rolling shutter, resulting in an interlaced aliasing effect where the flicker introduced noise at a base value of 1-10 Hz but also at higher harmonics. It was exceedingly difficult to filter out the noise without severely distorting the OAP waveform. We compromised by low pass filtering aggressively at 50 Hz, which produced a noisy baseline but reduced interference at the OAP peak. Further, single-emission capture of potentiometric dye activity can introduce a distorted baseline as a result of photobleaching. Consequently, we focused on maintaining the integrity of the OAP upstroke and peak

TABLE 5.3: Table of beat rate in the literature

	Isolated cells (BPS)	Confluent culture (BPS)
George et al. (2003)		2.5
Yang et al. (2005)		1-1.7
Sartiani et al. (2002)		1.3-5
Yang and Murray (2011)	1-1.3	2.5-3
Law et al. (2009)		1

waveform at the cost of a distorted baseline. Ideally, future experiments would use a stable high power LED based system to avoid flickering.

5.5.3 Cell types and distributions in the HL-1 cell line

We found two distinctive cell types in our HL-1 cultures, identified by the presence/absence of a slow depolarising phase 4 baseline. These findings were in agreement with the literature in these cultures, where pacemaking and non-pacemaking cells were found (Sartiani et al., 2002, Yang and Murray, 2011). Furthermore, contractile frequency was found to vary between 1-5 BPS, as summarised in Table 5.3. Typical values for contractile frequency in the literature are on par with those reported here. It is reasonable that rotors would activate at a higher rate than singular pacing sites, explaining the lower activation frequencies seen in the literature.

Reported cell distributions for the HL-1 cell line are varied in the literature: spontaneous cell activity was seen in between 30% and 68% of cells in the culture. Sartiani et al. (2002) found that 30% of cells in culture expressed the hyperpolarisation-activated i_f current which relates to the slow depolarisation phase of pacemaking cells. Conversely, Yang and Murray (2011) found that 68% of cells exhibited a slow phase 4 diastolic depolarisation characteristic of cells found

in natural pacemakers such as the SAN. These two findings are noticeably in conflict, but result from the nature of cell distribution in cultured cells. The culture of HL-1 cells requires that twice a week the cells be dissociated from one another and their culture flask to be passaged. When seeding the cells for experimental work, the same process must be undertaken. It is conceivable that two situations could have arisen: first, the continual passages could have selected for a specific cell type; second, the experimental plating process may have produced an uneven representation of the cells. Interestingly, we found the cell distribution to be 70% pacemaking/30% non-pacemaking. Our study was not comprehensive (N=20) and was not conducted for the purpose of elucidating the cell distribution; rather, we were attempting to establish the number of cell types that existed in the culture and for optical/electrical comparisons. We selected specific sites when impaling cells, so the true randomness of the dataset is questionable. These sites were usually clumps of cells chosen to provide structural support for the cell to be impaled. The impaled sites may have had a high density of pacemaking cells for other reasons. Without a more comprehensive investigation, we could not infer the exact cell distribution of the population. This work is most interested in the interactions between cells during activation as opposed to initiation (pacemaking); as such, we focused on the non-pacemaking cell type and assumed it to be the major cell type in the culture. This fed directly into our modelling work described in Chapter 6.

5.5.4 Optical imaging of electrical activity

The optical imaging of this chapter was typically captured at 200-500 FPS, with no more than 3 ms exposure time. This value was selected as a compromise between consistently capturing activation and reducing the effects of distortion from the rolling shutter effect. We found that using exposure times less than 3ms would give good results initially, but as photobleaching took effect, the flickering of the lamp began to dominate the OAP signals. Further, we found that with the 4X objective we did not observe any benefit in the clarity of activation mapping by decreasing the exposure time. In other words, at 3 ms there was no apparent rolling shutter

effect. At higher magnifications, 20X or 40X, decreasing the exposure time was reasonable, and we were able to discriminate the AP of a single cell at 1 kHz frame rate with 1 ms exposure time.

The radius-angle relationship of the observed rotors exhibited a linear characteristic (Figure 5.12), akin to an Archimedean spiral. The cell monolayer has isotropic intercellular conductivity, so it is expected that the activation wavefront would spread in a radially-symmetric manner. Further, the linear nature of the radius-angle relationship suggested that the conductivity was the same everywhere in the HL-1 monolayer and so the conduction velocity was identical in all locations. Once again, the flickering of the lamp caused some distortion of the apparent spiral progression but the data acquired represented a good approximation of the expected trend for a rotor wavefront.

Preparations in which we captured the source of excitation were driven by rotor systems, though this is not a new finding (Umapathy et al., 2008). We have already confirmed the presence of pacemaking cells in our HL-1 culture, leading us to hypothesize that there could be multiple sites of pacemaker-derived excitation. However, rotor-based excitation appears to be the primary mechanism in maintaining long-term electrical activity in these cultures. The preference for rotor systems could stem from multiple ectopic activation sites in the cell culture monolayer. Multiple sites of activation would result in wave collisions that could create self-maintaining rotors. When mechanically separating the rotor from a section of the monolayer by damaging the tissue with a pipette to create a cell island with no apparent electrical activity, we found that after a given time the isolated island of cells created a secondary rotor system, independent of the original rotor, without any additional stimulation. This indicates that electrical activity in these cultures is initiated by an event, such as depolarisation of pacemaking cells, but quickly settles into a rotor reliant system. In order for the rotor to take control of the culture, it must activate at a faster rate than the original pacing sites. Given that the rotor is most likely activating as fast as the refractory period of the cells will allow it, it is feasible that the rotor will eventually quench the initial sites of pacemaking and establish itself as the dominant source of electrical activation.

We observed wave collisions during the experiments, suggesting that there were two or more pacing systems present in the culture, as seen previously (Umaphathy et al., 2008). Wave collisions were observed rarely, and the optics made the process difficult to visualise, as we were required to mosaic large portions of tissue to attempt to uncover the origins of the two sources. In this work, we focused on isolating a single rotor, and typically this was the only obvious source of electrical activity in our experiments. The lack of visualised wave collisions may result from optical limitations, or from the state of the culture. We cultured the monolayer to be extremely confluent: in parts the culture was 2-3 cells thick. However the culture was not uniformly 2-3 cells thick: rather it varied between single cell valleys and multi-cell peaks. This anisotropy may have lent itself to the generation of rotors and the detriment of multi-site rotor-based activation.

We observed that rotors were stable if the environment was stable. Rotors would maintain electrical activity for hours, even during multiple staining cycles. Large disturbances, by either mechanical or temperature-based events, would tend to disturb this stability and the site of rotor-based initiation would reappear in a new location, occasionally quite a distance from the original source. Specifically, we found that sudden drops in temperature to $< 30^{\circ}\text{C}$ could cause the driving rotor to change location. It is not surprising that the electrical activity was perturbed by low temperatures, but the shift in spatial location of the initiator suggested that the culture had no fixed stable site of excitation: rather it presented multiple sites in which a source could appear. Unlike with our physical isolation experiment, the new site of excitation would appear within minutes, often between two optical recordings.

Optical activity at the centre of the rotors was found to be minimal (Figures 5.9 and 5.10). This phenomenon could result from an intrinsic electrophysiological properties of the HL-1 cells, or from the physical interconnections between neighbouring cells. The rapid activation of tissue at the centre of the rotor may have caused the inner most cells to enter a refractory period that was continually sustained by the rotor. Alternately, there may be some physical property of the interconnecting cells at the centre of the rotor that creates the arrhythmia-like

activity. This could be a specific pattern of conduction or no conductivity at all. It is difficult to know the exact activity taking place in the rotor centre, as our baseline signal was noisy. However, computational modelling could shed further light on electrical activity at the centre of our observed rotors.

5.6 Conclusion

In this chapter we acquired basic characteristics of the HL-1 cell culture and its underlying electrical activity. We have for the first time established an emission spectrum for di-4-ANEPPS in live HL-1 cells, confirming the two major cell types and optical-electrical equivalence of OAPs. We investigated the underlying electrical activity and found that the primary source of excitation was arrhythmia-like rotor systems. Further, we extracted data from the optical mapping including conduction velocity and OAP wave-width.

In order to effectively model the HL-1 monolayer we require information on electrical activity in the constituent cells. This chapter provides vital information for our computational modelling, described in the next chapter. Once such a model has been established, we can begin to ask questions about the governing mechanisms of activity such as the tendency for rotor-based initiation in the HL-1 monolayer.

Chapter 6

Modelling electrical activity in the HL-1 cell line

6.1 Single cell modelling

6.1.1 Single cell AP fitting

Using experimental sharp electrode data of membrane potentials in the HL-1 non-pacemaking cells, we were able to fit a three-current generic ionic model. As confirmed by the results in Figure 6.1a), the model membrane potential for a single cell stimulated at 5 Hz matches our recorded single cell data. The fit in phase 4 of the AP was visibly poor, a result of the unstable baseline eliciting late onset phase 4 slow depolarisation (Figure 6.1a)).

The model is fitted to the single cell HL-1 AP data with an RMS error of 3.42 mV (Figure 6.1). The baseline of the sharp electrode data has a slight diastolic depolarisation that we did not attempt to fit with the model. Evidence suggested the diastolic depolarisation was not a characteristic of the single cell AP, but rather a manifestation of the electrically active cellular syncytium. Cells were not stimulated during recording and any activation was auto-rhythmic in nature. It is hypothesised that the late onset slow depolarisation in the AP results from

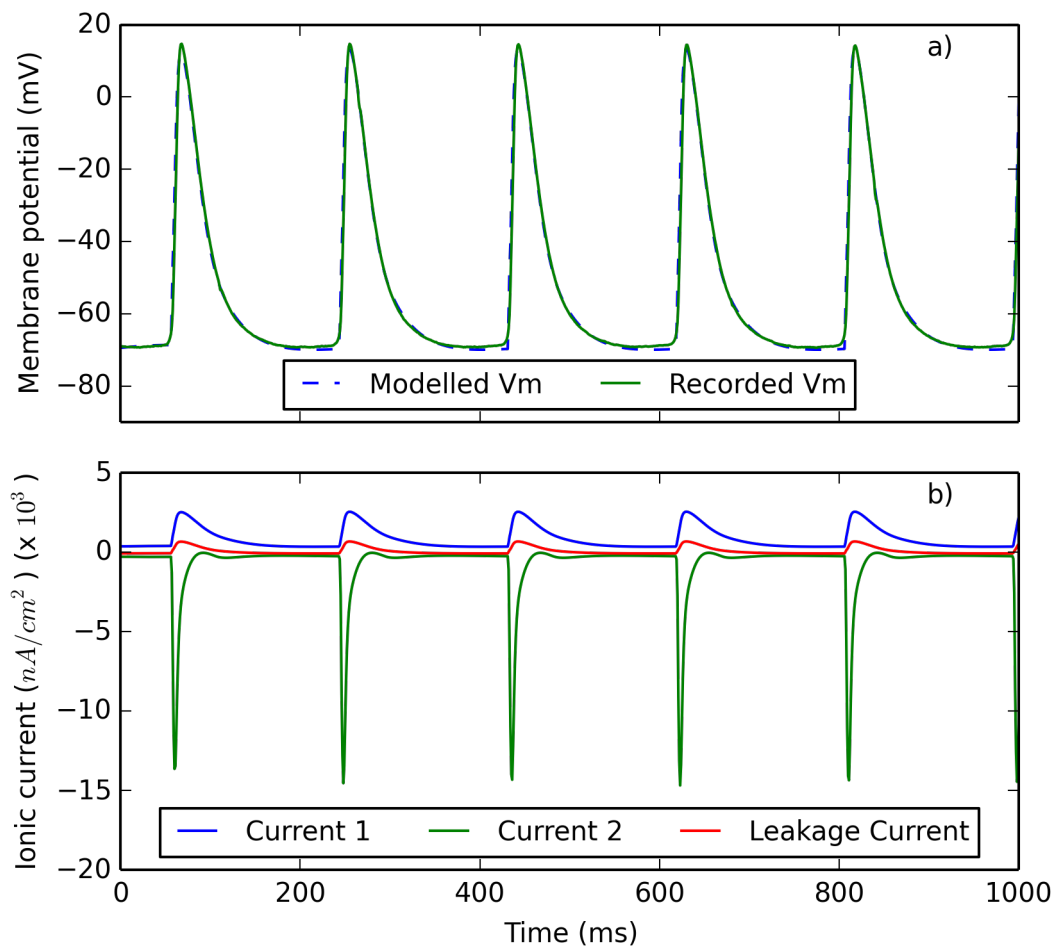


FIGURE 6.1: a) Membrane potential for single cell optimised AP in the three current generic ionic model. The model was stimulated at 5 Hz. The recorded data (green) was overlaid with the optimised waveform from the single cell model (dashed blue). Resting membrane potential was -69 mV. b) Ionic currents for optimised single cell AP. The model used contains three currents presented in nA/cm^2 . The currents presented in b) correspond to the membrane potential given in a).

intercellular current brought about by the impending AP wavefront. Further, AP waveshapes of isolated non-pacemaking HL-1 cells in the literature exhibited steady baselines (Sartiani et al., 2002).

6.1.2 The generic ionic model structure

We employed a three-current generic ionic model to represent APs in HL-1 cells, this number of currents was found to be the minimum required to reproduce reasonable HL-1 APs. More currents may be introduced, but are only necessary when the dynamics of the AP data reach a certain complexity, i.e. randomised pacing typically required more currents to fit (Guo et al., 2013). The model used three currents: an inward time-dependent, outward time-dependent and a leakage current (Figure 6.1b)). These membrane currents did not represent any channel specific dynamics, such as i_{Na} ; rather, they embody the culmination of currents necessary to reproduce electrical phenomena in excitable cells. The time-dependent outward current, Current 1 in Figure 6.1b), was an i_K -like current that sustained the AP for its duration. The time-dependent inward current, Current 2 in Figure 6.1b), represented an i_{Na} -like current that initiated the rapid depolarisation of the cell. Finally, the leakage current was an outward current that assisted with maintaining electrical stability. The closest analogue for the leakage current would be the background pumps and exchangers typically found in excitable cells.

6.1.3 The optimisation routine

Recall from Section 4.5 that the optimisation procedure represented an iterative least-square reduction of the objective cost function, defined as the weighted sum of squares difference between the electrically recorded membrane potential and the membrane potential simulated by the model. At initiation of the optimisation routine the weight function is under the control of the user. Choice of weight function was very important for fitting specific features of the HL-1 AP. In the case of single cell optimisation to fit the non-pacemaking AP we increased the weighting on the upstroke. The late onset slow depolarisation in the electrical AP data tended to manifest itself in the model as phase 4 pacemaking, such that the model would elicit an AP event without stimulation. To quench this activation, we ran a second optimisation routine with uniform weighting and no stimulation

to force the model to remove its pacemaking properties: as such the baseline of the optimised single cell modelled AP does not possess a late onset slow depolarisation phase. The selection of an appropriate weight function is important to prevent the optimisation routine from wandering into an undesirable region of the parameter space.

6.1.4 Single cell model parameters

Table 6.1 presents the optimised parameters for the single cell model. The model is based on Hodgkin-Huxley dynamics and represents ionic and dynamic properties in standardised units. It is important to note that each current represents the culminated effect of a number of currents as opposed to a singular current like i_{Na} . For example, $E_{rev,1}$ has a value of -99 mV which does not correspond to the reversal potential of any specific ion. We present the initial values for the optimised single cell model of non-pacemaking cells in Table 6.2.

The parameters presented in Table 6.1 were under the automated control of the optimisation code, manual adjustment of these parameters was rare. Conversely, the initial values were manually set at the beginning of the optimisation routine. Initial values were updated if the steady state behaviour of the model was considerably different to initial behaviour. In this case, initial values were extracted from the model at its resting membrane potential when it had reached steady state.

TABLE 6.1: Single cell optimised parameters used in Equations 2.5- 2.10

Designation	Current 1	Current 2	Leakage current	Units	Description
\bar{g}_j	22.4	$9.94 \times 10^{+03}$	9.05	$\mu\text{S}\cdot\text{cm}^{-2}$	max. membrane conductance
$E_{rev,j}$	-99.8	26.4	-60	mV	reversal potential of I_j
$k_{\alpha pj}$	$1.91 \times 10^{+03}$	147	NaN	s^{-1}	maximum of α_{pj}
$s_{\alpha pj}$	-0.144	-0.2	NaN	mV^{-1}	slope of α_{pj}
$k_{\beta pj}$	$3.19 \times 10^{+03}$	$4.28 \times 10^{+03}$	NaN	s^{-1}	maximum of β_{pj}
$s_{\beta pj}$	0.101	0.102	NaN	mV^{-1}	slope of β_{pj}
$E_{\alpha\beta pj}$	-80.4	-50.1	NaN	mV	E_{50} for α_{pj} and β_{pj}
$k_{\alpha qj}$	750	15.8	NaN	s^{-1}	maximum of α_{qj}
$s_{\alpha qj}$	-0.0918	0.189	NaN	mV^{-1}	slope of α_{qj}
$k_{\beta qj}$	$1.01 \times 10^{+03}$	231	NaN	s^{-1}	maximum of β_{qj}
$s_{\beta qj}$	0.184	-0.156	NaN	mV^{-1}	slope of β_{qj}
$E_{\alpha\beta qj}$	-78.7	-56.4	NaN	mV	E_{50} for α_{qj} and β_{qj}

Note: j refers to the j -th current

TABLE 6.2: Initial values for parameter-optimised single cell model

V_m (mV)	p_1	p_2	q_1	q_2
-69.4	0.6357	8.044×10^{-4}	0.8228	0.3815

6.2 Network model of the HL-1 monolayer

6.2.1 Tissue-based optimisation

Once the model was optimised to fit to experimentally recorded APs of non-pacemaking HL-1 cells, we introduced the single cell parameters into our network model to simulate electrical interactions between HL-1 cardiomyocytes in a syncytium. Here we present the optimisation of the network model and network parameters such as tissue conductivity.

Application of the single cell parameters directly to the network model resulted in the quenching of AP propagation. A manually applied increase in the maximum conductivity of the inward and outward time-dependent currents in a 1.5:1 ratio enabled propagation of APs in the network model. Henceforth, control of dynamic parameters was given to the optimisation routine.

Tissue optimisation required monitoring of action potential shape and propagation speed. The model AP waveshape was again fitted to the single cell electrical data of a non-pacemaking HL-1 cardiomyocyte. Conduction velocities calculated from our experimental OAP data were used to select the tissue conductivity. The AP waveshape was fitted automatically by allowing the optimisation routine to control the generic ionic model parameters. Table 6.3 lists values for the optimised parameters of the 2D network model of electrical activation. These parameters represent a three-current ionic model based on Hodgkin-Huxley dynamics that were optimised in the presence of a homogeneous network of cells. Initial conditions, inter-node spacing and tissue conductivity were controlled manually. Initial conditions and tissue parameters are given in Tables 6.4 and 6.5.

We selected the point most central in the network for fitting AP waveshape of the model to the electrical data in order to avoid any edge effects of the network model. Conductivity was calculated using a planar wave of activation (Figure 6.3) at as great a distance as possible between the two points. The tissue conductivity was manually adjusted iteratively until the network model exhibited conduction velocities acceptably close to those seen experimentally.

Much like in Chapter 5, the initial values were selected from the resting membrane potential of the tissue-based model once it had reached steady state. The initial values were retained as long as they faithfully reproduced the experimental data.

TABLE 6.3: Tissue-level parameters used in Equations 2.5- 2.10

Designation	Current 1	Current 2	Leakage current	Units	Description
\bar{g}_j	28.9	$1 \times 10^{+04}$	9.07	$\mu\text{S}\cdot\text{cm}^{-2}$	max. membrane conductance
$E_{rev,j}$	-99.7	42.4	-60	mV	reversal potential of I_j
$k_{\alpha pj}$	$1.51 \times 10^{+03}$	164	NaN	s^{-1}	maximum of α_{pj}
$s_{\alpha pj}$	-0.16	-0.2	NaN	mV^{-1}	slope of α_{pj}
$k_{\beta pj}$	$1.93 \times 10^{+03}$	$4.23 \times 10^{+03}$	NaN	s^{-1}	maximum of β_{pj}
$s_{\beta pj}$	0.0912	0.146	NaN	mV^{-1}	slope of β_{pj}
$E_{\alpha\beta pj}$	-79.6	-50.3	NaN	mV	E_{50} for α_{pj} and β_{pj}
$k_{\alpha qj}$	465	11.7	NaN	s^{-1}	maximum of α_{qj}
$s_{\alpha qj}$	-0.0875	0.193	NaN	mV^{-1}	slope of α_{qj}
$k_{\beta qj}$	$1.01 \times 10^{+03}$	241	NaN	s^{-1}	maximum of β_{qj}
$s_{\beta qj}$	0.177	-0.116	NaN	mV^{-1}	slope of β_{qj}
$E_{\alpha\beta qj}$	-76	-52.8	NaN	mV	E_{50} for α_{qj} and β_{qj}

Note: j refers to the j -th current

TABLE 6.4: Initial values for parameter-optimised tissue-based model

V _m (mV)	p_1	p_2	q_1	q_2
-69.3	0.7035	8.892×10^{-4}	0.5665	0.3085

TABLE 6.5: Conductivity and scale values for MATLAB-based 2D finite difference approximation

Variable	Value	Units
Inter-node interval	0.00315	cm
Conductivity	1.7	$\mu S/cm$

In Table 6.5, we list the value for the inter-node interval, which is the node to node distance in the x and the y directions: the finite difference approximation of the network model assumes that the x and y separation of each node is identical.

The weight function used for optimisation of the tissue-based model was iteratively adjusted to encourage fitting of the model to the electrical data. Typically, we would focus an optimisation run on fitting either the baseline or the peak of the AP. We found a uniform weight function resulted in poor fits, and that a poorly chosen weight function would cause the optimisation routine to wander aimlessly through the parameter space. We would commonly have to reset parameters and adjust the weight function to produce desirable results.

After optimisation, stimulation of the model evoked a conduction velocity of 1.82 cm/s at 5.3 BPS and the model waveshape was matched to the data. The RMS error of the fit was 2.9 mV for the unweighted calculation. Weighted error is not presented as the model was fitted in all regions of the AP. Unlike the single cell optimisation, the baseline fit is improved in the tissue-based model, as such the error is lower. The optimised model did not exhibit spontaneous electrical activity. The fit of the baseline is believed to stem from intercellular (node-to-node) current flow. The 50% AP wave-width of the model was 472 μm .

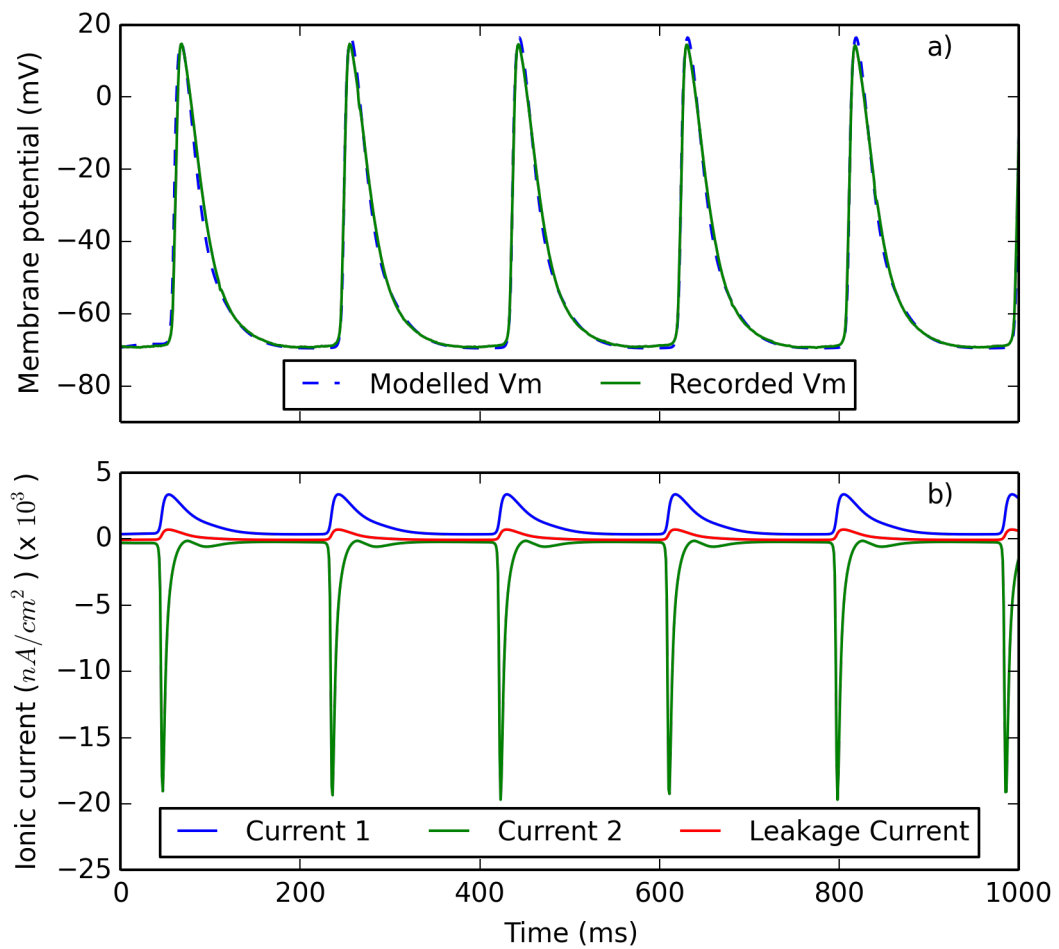


FIGURE 6.2: Optimised AP waveforms in the presence of other cells. Modelling results were extracted from the same node. a) Modelled membrane potential and recorded membrane potential of non-pacemaking cell. b) Waveshape of three ionic currents from the model.

The optimised tissue-based model AP is compared with the electrical data from the non-pacemaking cell in Figure 6.2a), while the ionic currents for the model are shown in Figure 6.2b). We observed that the model fitted well to the data, and that the ionic currents followed physiologically-reasonable patterns, with similar characteristics to those seen in the single cell model. Figures 6.3 to 6.4 demonstrate propagation of the optimised planar AP.

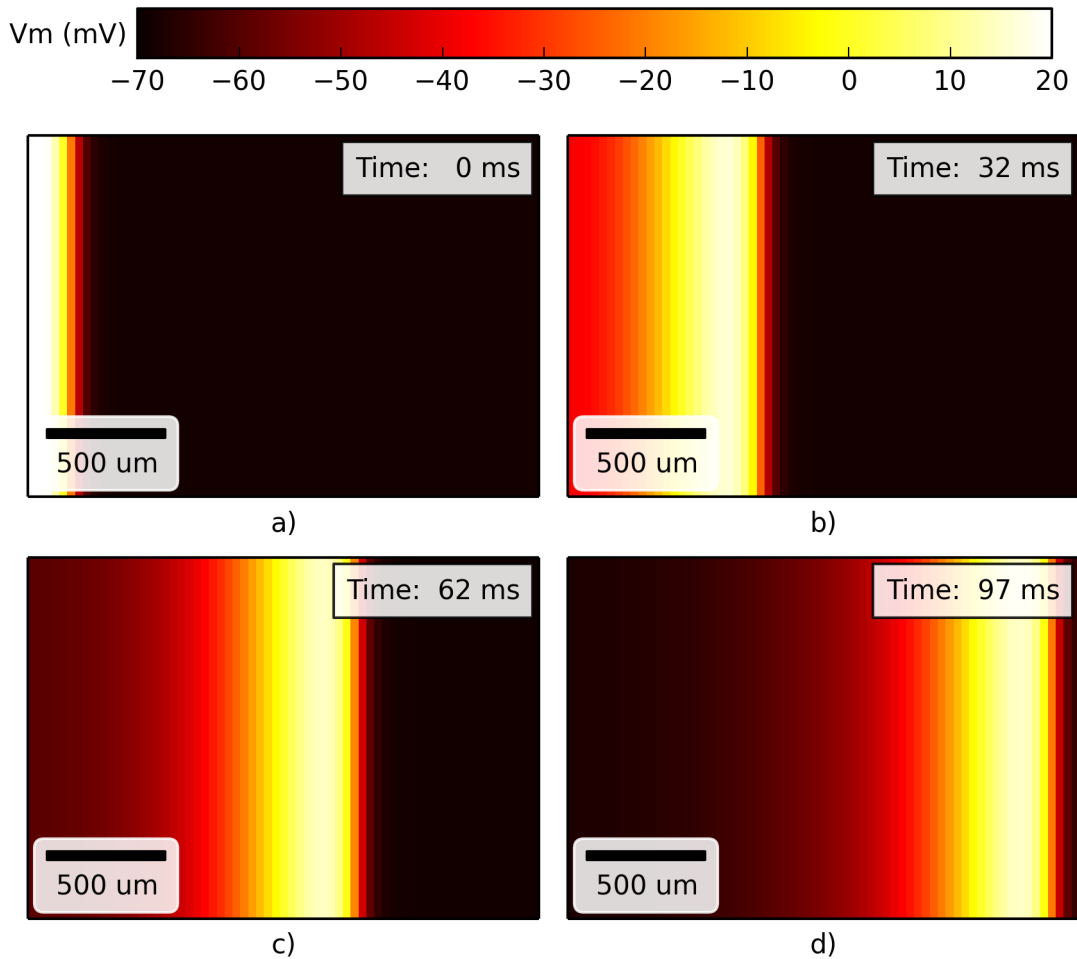


FIGURE 6.3: Linear wavefront propagating from left to right. This wavefront is the type seen at a distance from the pacemaking source.

6.2.2 Self-maintaining AP rotors

After optimising the model parameters to fit the experimental data, we initiated rotors in the 2D tissue to replicate rotor activity visualised in the HL-1 preparations (Figure 6.5). Briefly, a stimulus was applied to the left-most boundary of the model and after a short delay, a second stimulus was initiated on the upper boundary, producing a self-maintaining spiral that rotated about a point in the network. The contour activation map is given in Figure 6.6 to provide more detailed timing information for the rotor system. Note that the rotor activity was modelled using the same parameters as the linear wavefront, we simply altered the stimulation protocol to elicit a rotor. The model was not fitted to the experimentally acquired rotor data.

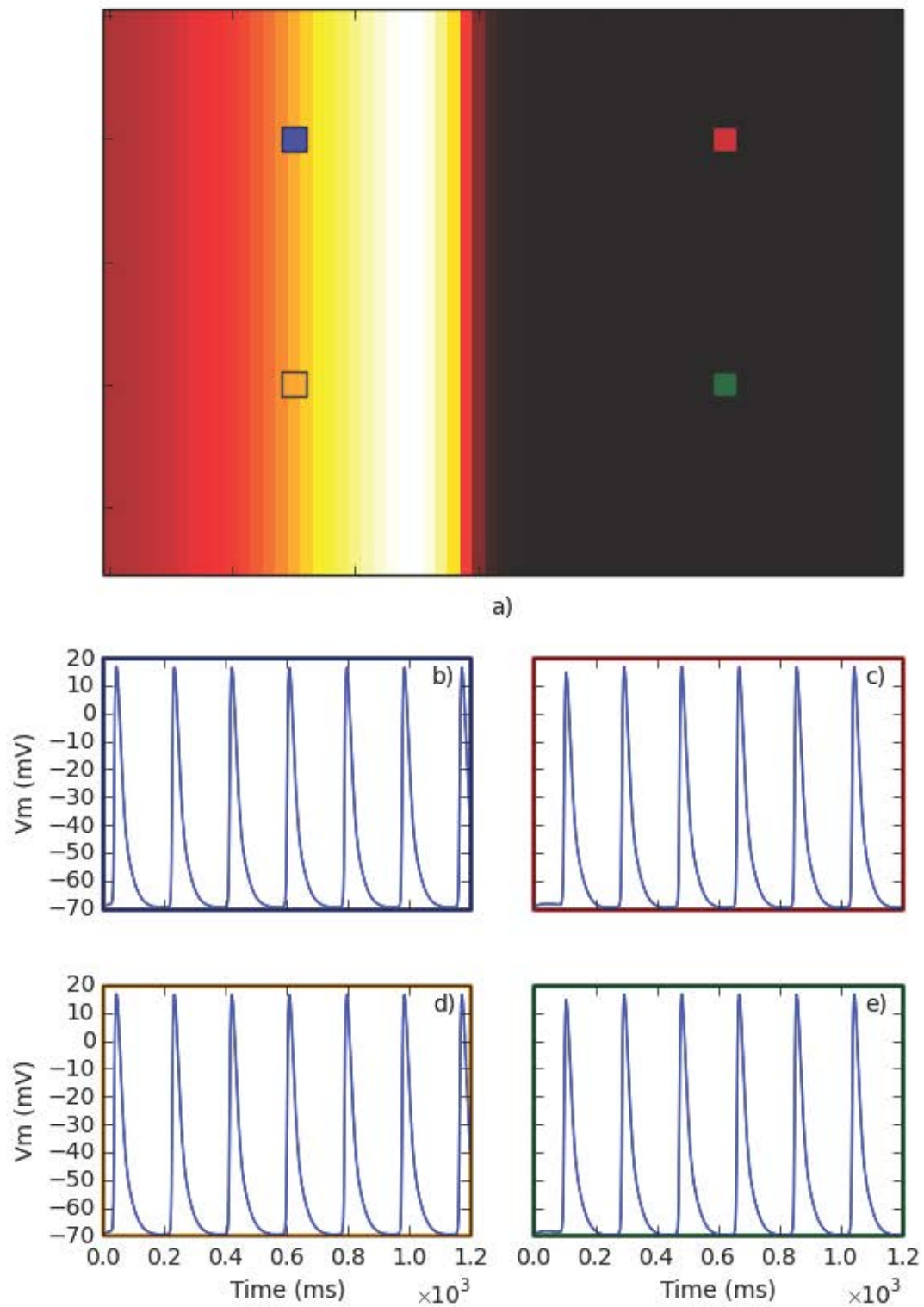


FIGURE 6.4: Simulated wavefront with APs at given nodes. We observed that the linear wavefront exhibited a homogeneous waveshape across multiple points in the tissue.

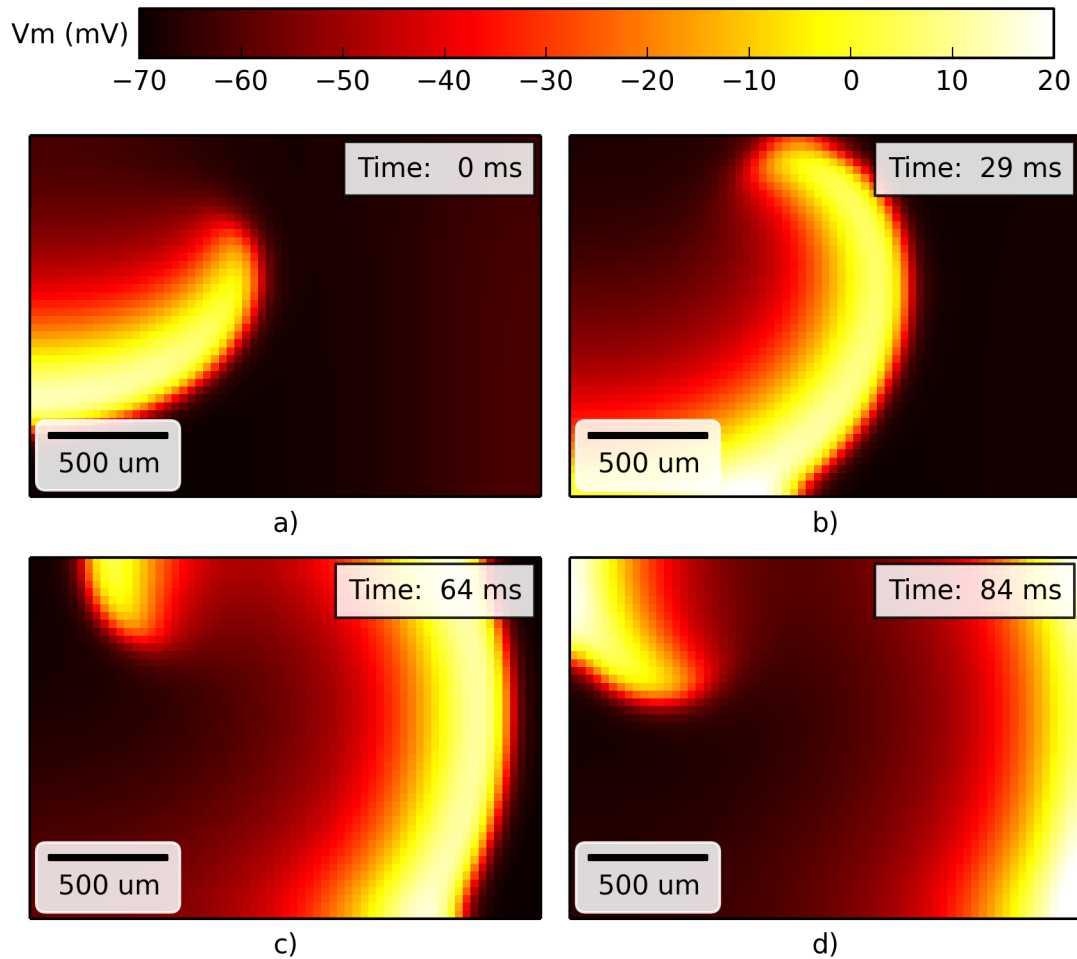


FIGURE 6.5: Simulated self-maintaining rotor system in the network model. The sample was stimulated once with two wavefronts, one delayed slightly, to initiate the rotor.

We presented the modelled rotor membrane potential against the electrically recorded non-pacemaking AP data in Figure 6.7. The conductivity properties of the rotor system are identical to those presented in Figure 6.5; however, the beat rate is different between the two preparations. The rotor exhibited 8 BPS compared with 5.3 BPS in our linear wavefront and experimental data (both rotor and linear wavefronts). However, the current profiles for both preparations were very similar.

We visualised electrical activity in the rotor at specific nodes (Figures 6.8 and 6.9). There was a clear absence of APs in the core of the rotor (Figure 6.8). Electrical activity tended to oscillate around -50 to -60 mV. Further from the centre of the rotor APs were more consistently produced (Figure 6.9). AP peak at all nodes

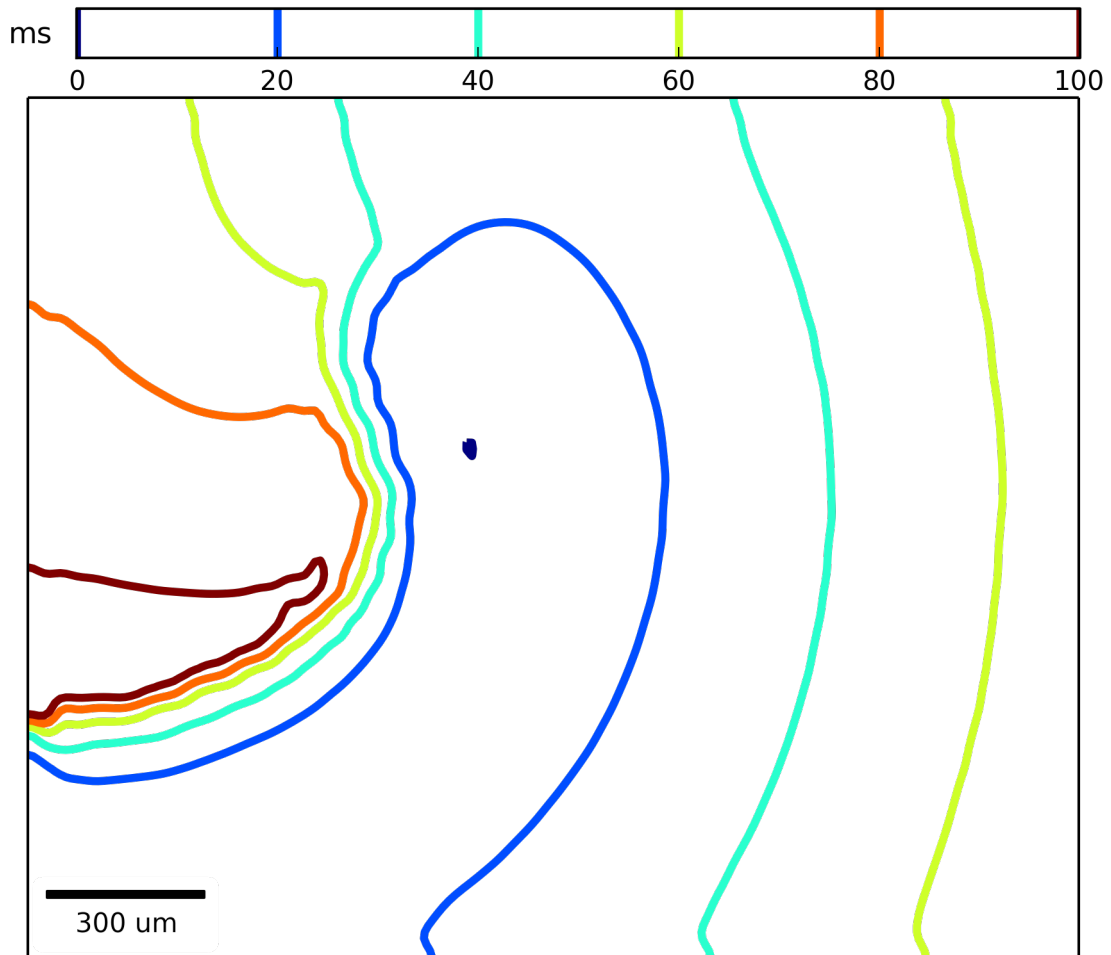


FIGURE 6.6: Contour map of the rotor system given in Figure 6.5

was between 0 and 10 mV and the minimum diastolic potential was -69 mV. The re-entrant rotor lacked an interval of diastolic quiescence: the rotor rapidly activated the tissue once the AP had reached approximately -69 mV such that the AP did not settle to its resting membrane potential for any significant period of time. AP 50% width was $441 \mu\text{m}$, beat rate was 8 Hz and conduction velocity was 1.66 cm/s.

We calculated the radius-angle relationship for the simulated rotor, as shown in Figure 6.11. The radial coordinate was calculated on a simulated rotor with a field of view selected to replicate our experiments. We felt this would provide the most accurate representation of the rotor in our network model and provide a basis for comparison with the experimental data.

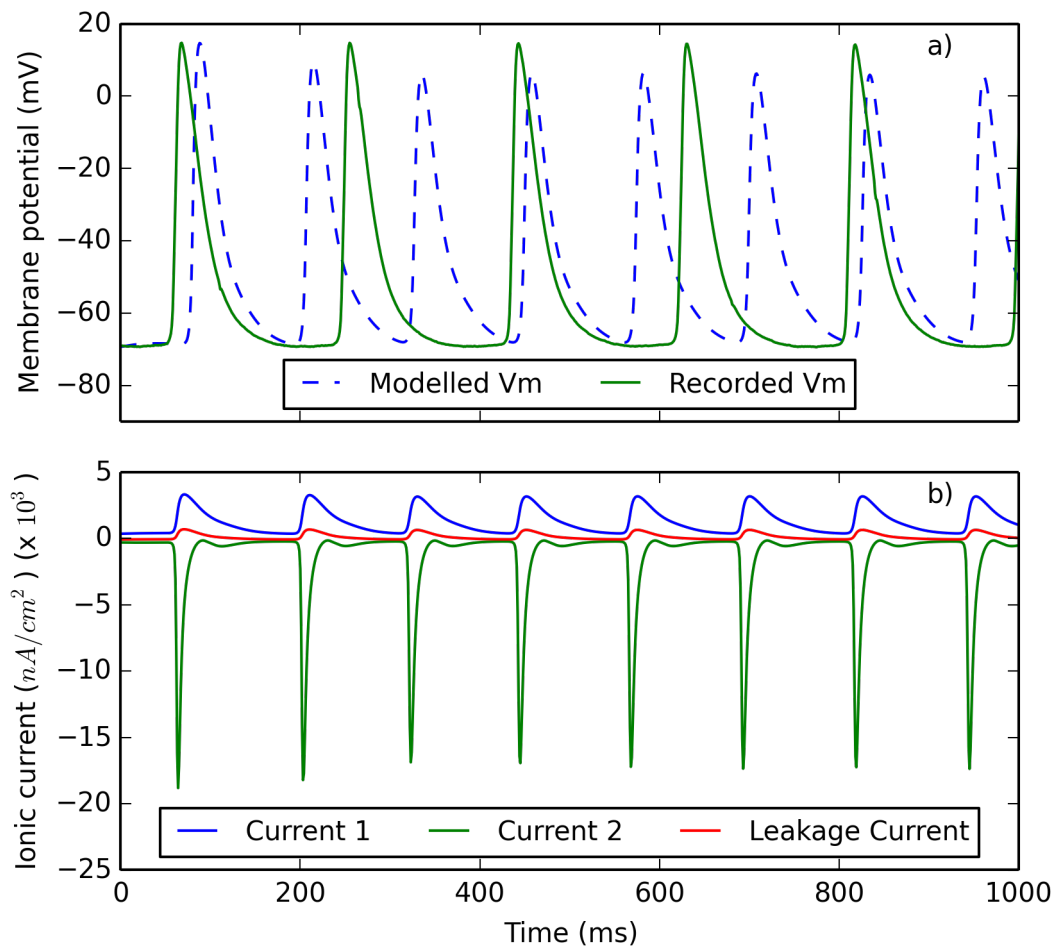


FIGURE 6.7: Electrical activation of model in the presence of a re-entrant rotor compared to recorded data. a) Modelled membrane potential vs. recorded membrane potential. b) Ionic currents simulated by the mathematical model.

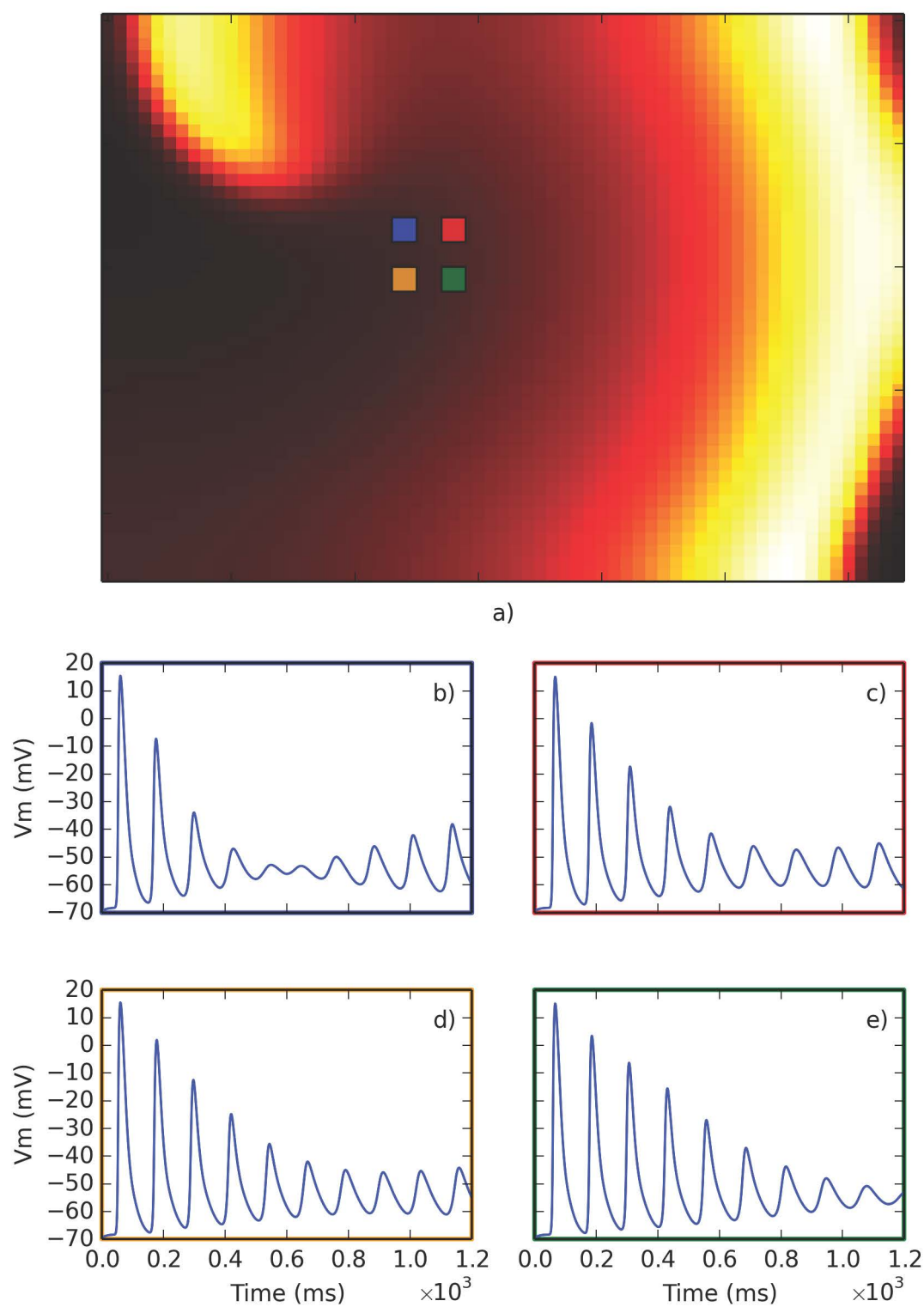


FIGURE 6.8: APs at specific points in the core of the simulated rotor system. Each point is shown by a coloured box that corresponds to a colour-outlined AP figure below the rotor image. That is, the blue rectangle in a) corresponds to the AP in b) which is surrounded by a blue box.

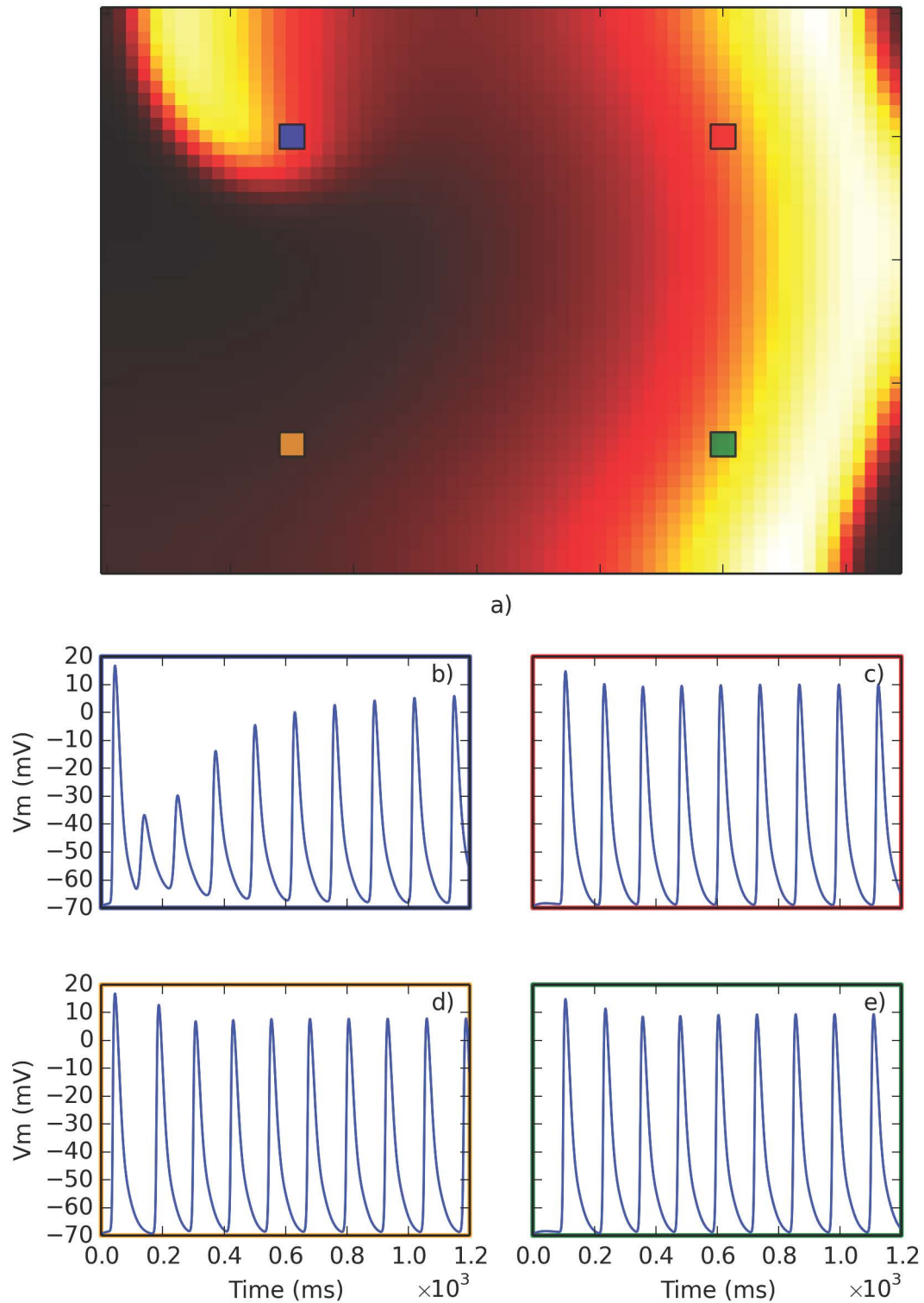


FIGURE 6.9: APs at a specific points far from the core of the simulated rotor. The AP waveforms are colour coded to illustrate their location in the 2D rotor.

6.3 Discussion

6.3.1 Cell selection for modelling

We confirmed in Chapter 5 that the HL-1 culture contains cells with pacemaking and non-pacemaking characteristics. For the purpose of modelling tissue electrical activity, we selected only the non-pacemaking cells to model AP initiation and propagation in the presence of other cells. The reasons for this are twofold: to simplify the model; and because the conflicting data in the literature on the exact distribution of cells in the HL-1 culture.

It has been reported variously in the literature that spontaneous cell activity is exhibited between 30% and 68% of cells in the culture. Sartiani et al. (2002) found 30% of cells in HL-1 cultures expressed the i_f 'funny' current, typically believed to play a part in the slow depolarisation phase of pacemaking cells. Conversely, Yang and Murray (2011) reported that 68% of cells elicited the slow phase 4 diastolic depolarisation characteristic of cells found in natural pacemakers such as the SAN. In Section 5.3.2, we presented our findings for the cell distribution as 70% pacemaking and 30% non-pacemaking.

A major limitation of the experimental work conducted in Chapter 5 was the lack of a stable baseline caused by a flickering fluorescent light source. We were unable to evaluate experimentally if any specific node is dominated by non-pacemaking or pacemaking cells, raising concerns about which cell-type we should model. In our experiments, we did not capture any pacemaking activity as is typically seen in natural pacemakers. Our data were limited to planar wavefronts at a distance from the source of initiation or the source was located and seen to be a rotor.

Our current work is most concerned with modelling electrical activity in stimulated and interconnected cardiomyocyte cultures. We were not able to experimentally visualise pacemaking activity, such as the phase 4 slow depolarisation. Further, this study was not intended to investigate interactions between pacemaking and

non-pacemaking cells. For these reasons we selected to model and fit only the non-pacemaking data. An interesting question is whether the presence of pacemaking cell types lends itself to initiation of rotors: our model provides the option to test this hypothesis.

We observed that the HL-1 cells were approximately $10\mu\text{m}$ in diameter when dissociated from their culture flask. This value can be used to estimate their footprint when plated onto an apparatus, providing greater detail about our experimental optical imaging and how best to relate it to the modelling work. Each pixel of the camera, under our 4X objective, corresponds to a pixel image size of $1.575\mu\text{m}$. Assuming an experimental spatial average of 20×20 pixels, the number of cells per model node is:

$$C = \frac{(20 \times 1.575 \times 10^{-6})^2}{\pi(10 \times 10^{-6})^2}, \quad (6.1)$$

which is approximately 3.2 cells per node.

Our model replicated electrical activity at each node, each node represents a section $31.5^2\mu\text{m}^2$, an area containing approximately 3.2 cells per node. To make sense of modelling a particular node, we would have to assign that node (and the three cells it contains) to one cell type, a non-pacemaking cell.

6.3.2 Single cell and tissue-based modelling

The single-cell and tissue-based ionic currents had noticeable variations (Figure 6.10). Current 1, i_1 , and Current 2, i_2 , correspond to generic outward and inward currents, presented differences in peak current and current-waveform width. Current 1 saw an increase in peak current from 2.5×10^3 nA/cm² (single-cell) to 3.35×10^3 nA/cm² (tissue-based), a 35% increase. Current 2 shifted from a peak of -1.47×10^4 nA/cm² (single-cell) to -1.97×10^4 nA/cm² (tissue based), a 34% increase. Current 1 exhibited a single cell half amplitude current-width of 35 ms, the corresponding tissue-based half amplitude width was 32 ms. Current 2 single

TABLE 6.6: Comparison between single cell and tissue-based model ionic currents

Current	Single cell (nA/cm^2)	Tissue-based (nA/cm^2)	% difference
Current 1	2.5×10^3	3.35×10^3	35% increase
Current 2	-1.47×10^4	-1.97×10^4	34% increase
Leakage current	662	693	5% increase

cell half-amplitude was 6 ms, with tissue-based half-amplitude also being 6 ms. By comparison, i_L peak current changed from 662 nA/cm^2 (single-cell) to 693 nA/cm^2 (tissue-based), a 5% increase. The 50% width of i_L was identical in the single cell and network models. These values are summarised in Table 6.7.

The increased peak current likely resulted from a combination two mechanisms: neighbouring ionic currents, or loading from neighbouring cells. First, the interconnection between nodes in the network model would result in flow of current from currently active cells to neighbouring inactive cells that could cause a boost in total current flow across the membrane. Second, electrotonic loading from neighbouring nodes may have required a larger current flux from the cells in order to evoke an AP of the same magnitude as the single cell variant.

6.3.3 Radius-angle relationship

We compared the radius-angle relationship of rotors in experimental optical data to the simulations of the network model in Figure 6.11. The radii were compared only in a single optical field of view: both the optical (spatially averaged) and modelling data were visualised over 60 (width) x 40 nodes/pixels (height) to allow a direct comparison. The limited optical field of view restricted insight into the spiral progression as large angles of rotation (θ) were not achievable. The experimental radius-angle relationship is presented as mean \pm SD and is overlaid with the radius of curvature from the rotor initiated in the network model. We observe from Figure 6.11 that the rotor progression for the network model is within one

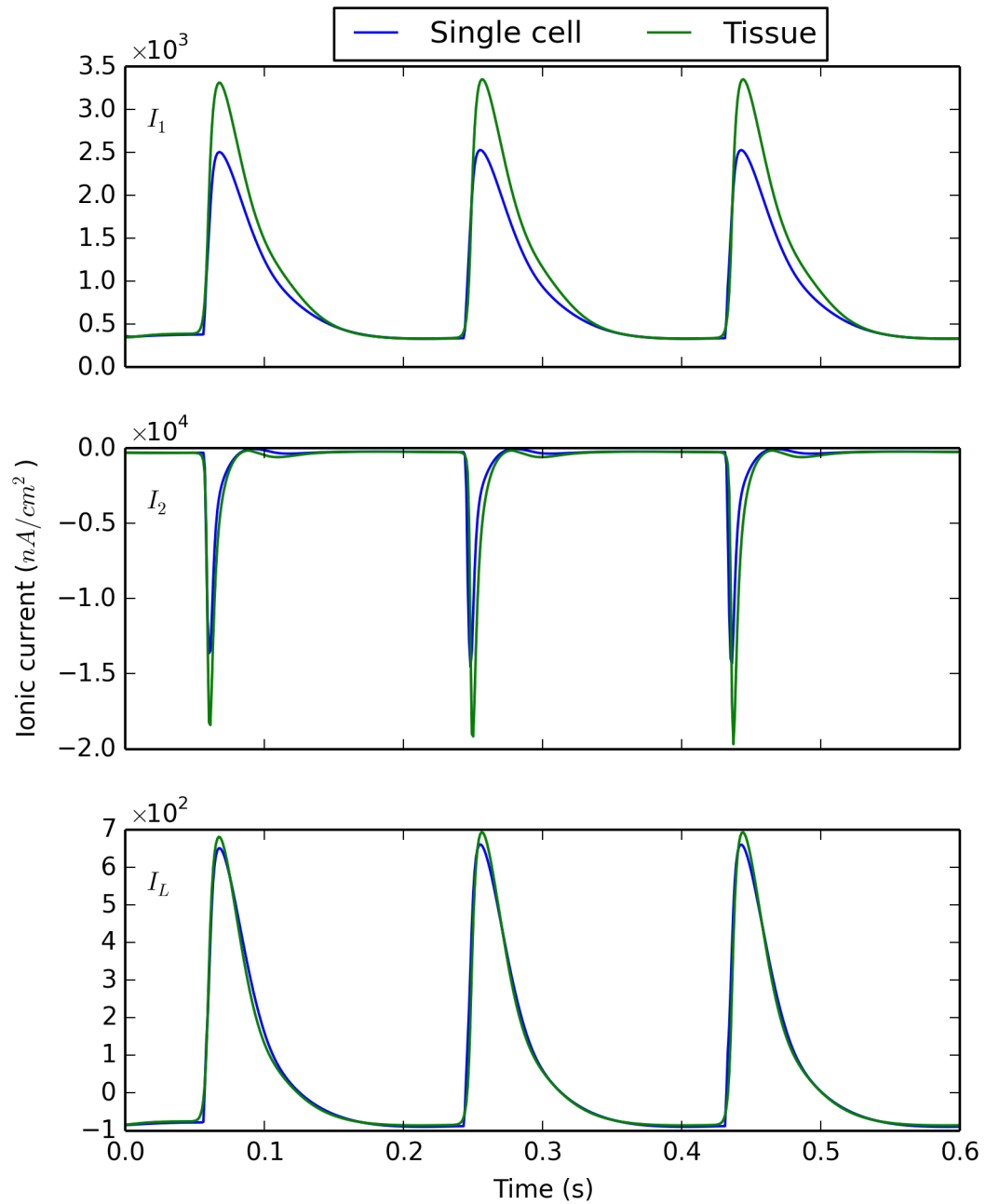


FIGURE 6.10: Comparison of ionic currents in optimised single-cell model vs. optimised network model. From top-most axis to lowest: Current 1 (i_1), Current 2 (i_2), and Leakage current (i_L). Data for tissue-based ionic currents are taken from the node in the centre of the network.

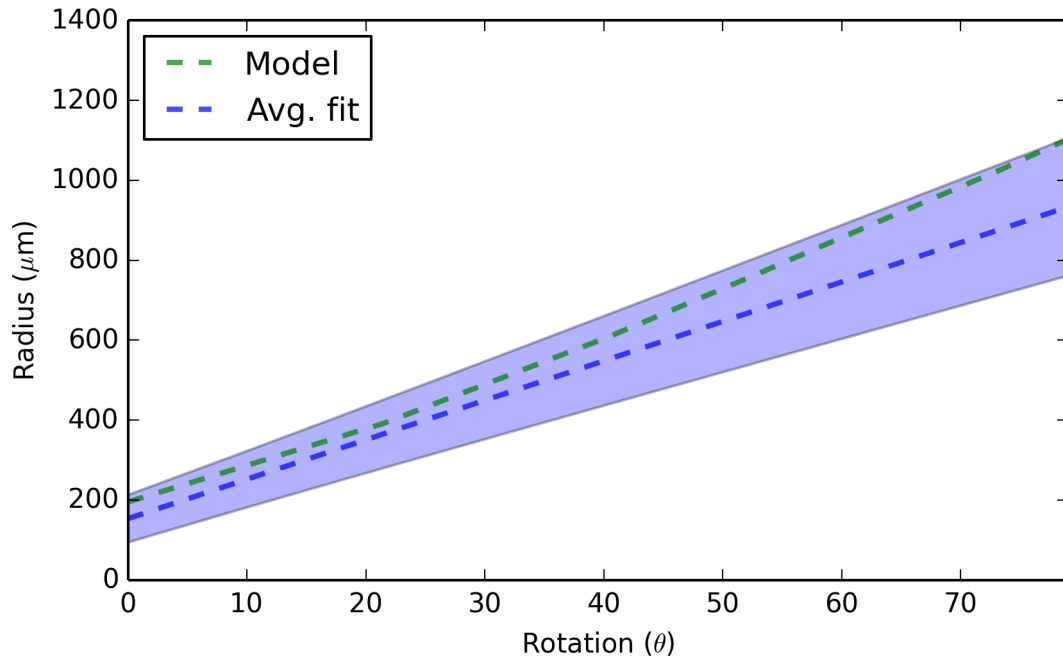


FIGURE 6.11: Comparison of rotor radius-angle relationship between simulation and experiment.

TABLE 6.7: Half-amplitude OAP width comparison

	Experimental (μm)	Modelling (μm)
Wavefront	424 ± 50	425
Rotor	367 ± 63	441

standard deviation of the experimental data up to 80° of rotation. The radial coordinate in the model appeared to diverge at around 70° of rotation, but we did not have the corresponding optical data to compare with this trend.

A point of concern for the analysis of rotor radius-angle relationship was the noisy nature of the optical data. The noise introduced experimentally from lamp flicker (Section 5.5.2) dramatically altered the baseline optical signal but can also cause distortion in the OAP peak, resulting in a more or less broad wavefront at any given time point. Further, the selection of rotor origin was arbitrary in the optical data, since the rotor profile did not readily provide a clear point of origin, unlike in the modelled wavefront. As such, we expected the experimental radius-angle characteristic to have a similar but parallel trend with the modelled characteristic.

6.3.4 Waveshape characteristics of experimental and modelled activation

We calculated half-amplitude AP, AP₅₀, width for the optical and modelling data presented in Chapters 5 and 6, repeated in Table 6.7. We present a single representative sample in Table 6.7. We did not fit to AP₅₀ and so we did not expect the correspondence to be accurate. Factoring in the noise that impeded optical imaging, like lamp flicker, we believe that the initial results are promising. We observed that the modelling was more consistent in its AP₅₀ than the experimental results.

6.3.5 Justification for the generic ionic model

The generic ionic model was designed to faithfully reproduce electrical phenomena in excitable tissues while limiting the computational toll of the modelling process. With improved techniques for imaging and reconstructing complex tissue structures, computation times have increased dramatically. The generic ionic model seeks to remedy this shift toward increased time of computation by providing as much detail as is necessary, and no more, to reproduce the electrical phenomena of interest.

We selected the three-current generic model as it contains the minimum amount of detail required to reproduce the /glsap characteristics of the HL-1 cells. The three-current variant contains five variables; namely, the membrane potential (V_m), p gating variable for current 1 (p_1), p gating variable for current 2 (p_2), q gating variable for current 1 (q_1) and the q gating variable for current 2 (q_2). However, this does not mean that the model is limited to three currents. The generic ionic model enables the addition of an arbitrary amount of membrane currents with each current adding two variables, (p_j and q_j for current i_j). In this way the generic ionic model is able to arbitrarily increase or decrease in complexity to reproduce detailed electrical activity.

6.3.6 An analysis of the rotor

One interesting characteristic of the rotor systems is the lack of activity at the core (Figure 6.8). The nature of the cell monolayer would suggest that the core is inactive because of a lack of homogeneous conductivity, but the modelling results disputed this hypothesis by illustrating that continuous conductivity can still support rotors with similar characteristics to those seen experimentally (Figures 5.9 and 6.8). Heterogeneous conductivity may well play a role, but these results suggest it is not critical for the maintenance of the rotor.

6.4 Conclusion

In this chapter we presented the fitting of a generic ionic model to both single cell and tissue-based electrophysiological data. We illustrated good fitting between experimentally acquired HL-1 non-pacemaking sharp electrode data and the single cell generic ionic model. The single cell parameters were then applied to and optimised for a network model where cells were interconnected to four neighbours. The network model was fitted to both electrical AP waveshape and optically-derived conduction velocity. A rotor was simulated in the network model and found to have good correspondence with experimental data without fitting. It was found that the null activity at the centre of the rotor is not a direct result of heterogeneous conductivity properties of the cell monolayer.

This network model serves as the basis for future work on the interaction between electrically connected cardiomyocytes. The control afforded by the HL-1 cell culture for experimental preparation and the versatility of the generic ionic model were a powerful combination for future studies on the underlying mechanisms of cardiac electrical activity.

Chapter 7

Conclusions and future work

7.1 Concluding remarks

For the first time, a computational model of the electrophysiology of the mouse atrial cardiomyocyte was developed. Experimentally acquired single cell and multicellular electrophysiological data was employed in the formulation and optimisation of the model to produce an accurate representation of the electrical phenomena in HL-1 mouse atrial myocytes.

To facilitate the development and optimisation of a robust computational model experiments were completed to characterise the HL-1 cell line both electrically and optically when exposed to potentiometric dyes, namely di-4-ANEPPS.

To our best knowledge, we presented the first emission spectra of di-4-ANEPPS in the HL-1 cell culture. Further, we found good correspondence between our results and the literature.

To ensure optical/electrical equivalence, concurrent optical and sharp electrode recordings were undertaken in spontaneously active confluent HL-1 cultures. The optical signal was found to follow the membrane potential, but noise from the fluorescent source impeded accurate optical mapping of the AP baseline.

Through sharp electrode studies, we confirmed the presence of two cell types, pacemaking and non-pacemaking, in the HL-1 culture and their distribution. The literature presented confounding results as to the distribution of cell types in HL-1 cultures. In this study, we found that approximately 70% of cells exhibited pacemaking characteristics.

Mapping electrical activity in the HL-1 atrial syncytium used a potentiometric dye: di-4-ANEPPS. Optical techniques enabled the visualisation of tissue-level interactions between electrically connected cells. Arrhythmia-like electrical rotors were common in cultures: they were found to be the most common source of spontaneous initiation. Experimental results provided vital information for the creation and optimisation of our ionic model.

A three-current generic ionic model was formulated for the non-pacemaking atrial myocytes found in the HL-1 culture. Its three constituent membrane currents were: an outward time-dependent (i_1), an inward time-dependent current (i_2), and a leakage current (i_L). The dynamic parameters of the model were iteratively adapted to fit the single cell model to sharp electrode experimental recordings. A good match between experimental and modelled AP was produced with an RMS error of 3.42 mV.

The single cell parameters were then applied to a network model and further optimised to reproduce tissue-scale behaviour seen experimentally. The network model was successfully fitted to the single cell AP waveshape and the experimentally observed conduction velocity. The AP waveshape of the model was fitted to the data with an RMS error of 2.9 mV. Further, without additional optimisation, we simulated the behaviour of a re-entrant rotor in the network model. Basic properties of the rotor, such as its linear radius-angle spiral shape, were found to match well with experimental data.

The generic ionic model embodies a new direction in computational modelling, with a complexity between simplified phenomenological and biophysically accurate models. The generic ionic model is also robust in that it can be arbitrarily

extended. Additional ionic currents enable modelling of more complex electrophysiological phenomena, but are only added as needed. Thus the generic ionic model allows the computationally simplest model to be implemented for a given data.

This thesis presents a platform for the experimental and computational study of mouse atrial cardiomyocytes connected in a syncytium. The HL-1 cell line provides a controllable medium through which we can experimentally test hypotheses. In combination with the generic ionic model, we have the versatility to reproduce physiological and pathophysiological conditions in cardiac preparations to extract information on the underlying ionic mechanisms.

7.2 Future work

The work outlined in this thesis can be extended in future through the following:

- Optimisation of generic model parameters to fit pacemaking cells in the HL-1 culture
- Investigation of influence of pacemaking cells on overall behaviour
- Application of ionic model to higher order geometries by the introduction of structural heterogeneities
- Investigation of the effects of long term culture in the presence of an electrical rotor.
- Co-culturing of fibroblasts and HL-1s to investigate electrotonic interactions and the effect of cellular heterogeneity.

Appendices

Appendix A

On the culture of the HL-1 cell line

A.1 Introduction

This appendix covers the culture of HL-1 cells, providing best practices and information that may not be widely available about this cell line.

A.2 Reagents

HL-1 cells have strict requirements for a number of reagents. It is important to adhere to these requirements to obtain healthy and functional HL-1 cells. HL-1 myocytes require a special medium known as Claycomb's medium and will lose their contractile phenotype if not cultured in a particular batch of fetal bovine serum (FBS). The reagents necessary for culturing HL-1 cells are given in Table A.1.

Claycomb media is an enhanced variant of Dulbecco's modified Eagle's medium (White et al., 2004). The Sigma-Aldrich variant of Claycomb media is proprietary and so

TABLE A.1: Reagents for HL-1 culture

Reagent	Vendor	Catalog #
Claycomb medium	Sigma-Aldrich	51800C
Fetal bovine serum	Sigma-Aldrich	12103C
Penicillin-Streptomycin (10^4 U/ml P and 10^4 μ g/ml S)	Sigma-Aldrich	P4333
Norepinephrine [(\pm)-Arterenol]	Sigma-Aldrich	A0937
L-Ascorbic Acid, Sodium Salt	Sigma-Aldrich	A7506
L-Glutamine, 200 mM	Sigma-Aldrich	G7513
Trypsin-EDTA (0.05% trypsin in 0.02% EDTA-Na)	Sigma-Aldrich	T3924
Trypsin Inhibitor Type I-S, Soybean	Sigma-Aldrich	T6522
Dulbecco's PBS (Ca^{2+} -free and Mg^{2+} -free)	Sigma-Aldrich	D8537
Fibronectin (1 mg/mL)	Sigma-Aldrich	F-1141
Gelatin from bovine skin	Sigma-Aldrich	G9391
OR Bacto Gelatin	Fisher Scientific	DF0143-17-9
Distilled Water, cell culture grade	Sigma-Aldrich	W3500
Cryovials, 2m mL round bottom	Corning	430289
Sterile Acrodisc syringe filters, 0.2 μ m	Gelman Sciences	4192
Freezing container	Nalgene	7-5100-0001

may have some additional reagents, but there appears to be no reason for those interested to make their own culture media.

The FBS suitable for culture of the HL-1 cell line has been tested by the Claycomb laboratory and should be the only FBS used. Using other serums can cause the cells to lose their contractile phenotype.

We used Gelatin from bovine skin as opposed to Bacto Gelatin. Further, reverse osmosis and double syringe filtered water was used, as well as our own PBS without noticeable effect on cell health.

TABLE A.2: Supplemented Claycomb's media

Reagent	Volume (mL)	Final concentration
Claycomb medium	87	
Fetal bovine serum (FBS)	10	10%
Penicillin/Streptomycin	1	100 U/mL:100 μ g/mL
Norepinephrine (10 mM stock)	1	0.1 mM
L-Glutamine (200mM stock)	1	2 mM

TABLE A.3: Formulation for wash medium

Reagent	Volume (mL)	Final concentration
Claycomb medium	94	
Fetal bovine serum (FBS)	5	5%
Penicillin/Streptomycin	1	100 U/mL:100 μ g/mL

Supplemented Claycomb Medium

Supplemented Claycomb medium is the formulation of Claycomb's media used to culture the HL-1 cells, containing extra reagents such as L-Glutamine. Its ingredients are given in Table A.2.

Claycomb medium usually comes in 500 mL bottles sealed in a light impermeant bag. The media is light sensitive and should be covered with aluminium foil as much as possible. After two weeks the L-Glutamine will have degraded to a point where it will require replenishment.

Wash medium

Wash medium is a variant of supplemented Claycomb media used for de-activating the Trypsin-Ethylenediaminetetraacetic acid (EDTA) solution after cell dissociation. It is summarised in Table A.3.

Norepinephrine [(±)-arterenol]

- Norepinephrine was formulated in 30 mM ascorbic acid (5.9mg/mL)
- Norepinephrine was added to 30mM ascorbic acid in a concentration of 3.2 mg/mL which makes up 10 mM stock.
- This working stock was sterile filtered and stored in sterile tubes at -20°C.
- Norepinephrine can only be stored for a month. We typically made fresh norepinephrine every time we made new media. As such, only the amount that was necessary was created. This equated to 7-10 mL of stock norepinephrine prior to sterile filtering. The filtering process results in about 1 mL of loss. The end volume was 5 mL for 500 mL of Claycomb medium.
- Norepinephrine is **toxic** and should be treated with care. The authors only handled the lyophilised powder inside a fume hood. The high air flow inside the fume hood presented its own issues, so a small chamber that could be surrounded by a large plastic snap lock bag was constructed. Norepinephrine was handled inside the containment, and once finished the plastic bag was sealed and disposed of appropriately.

Freezing medium

- Freezing medium was made up of 95% FBS/5% dimethyl-sulfoxide (DMSO)
- Can be stored for up to a month. We typically made freezing medium on the day that cells were frozen down.

Soybean Trypsin Inhibitor

- Soybean trypsin inhibitor was made at a concentration of 0.25 mg/mL in PBS.

- After sterile filtering, the trypsin inhibitor can be stored for up to a month at 4°C.

Gelatin/Fibronectin

- Weigh 0.1g and place it in a glass bottle with 500 mL cell culture grade water.
- Autoclave the solution at 121°C so that the gelatin will dissolve: the concentration is 0.02% gelatin.
- Dilute 1 mL fibronectin in 199 mL 0.02% gelatin and mix gently.
- The resulting gelatin/fibronectin should be stored at -20°C.

A.3 Culture

Coating flasks

- Tissue culture flasks were coated with gelatin/fibronectin by adding 2-3 mL to a T25 flask (4-6 mL for a T75). We coated the flasks overnight at 4°C. We initially had issues with smaller volumes of gelatin/fibronectin evaporating. As a result, we would occasionally leave the flask in a box with a wet tissue to prevent evaporation.
- The flasks can also be coated in the incubator (37°C) for an hour.
- Excess gelatin/fibronectin was removed immediately before the introduction of cells.

Feeding cells

- Cultures were fed (5 mL/T25 flask) with supplemented Claycomb medium every weekday.

- On weekends the cells can be fed 10 mL (T25 flask) and refreshed on Monday morning. We typically passaged on Tuesdays and Fridays, so feeding 10 mL for the duration of the weekend is a reasonable measure. As one would expect, the cells metabolic requirements are far less when newly passaged as compared to fully confluent. We found that HL-1 cells needed the most consistent refreshment of media when contraction began culture-wide.

Receipt of cells

Cells were received in T25 flasks at passage 48, with sealed lids, filled to the brim with Claycomb media. In our experience, the flasks were Corning T25s for which we had no filtered lids. The media was refreshed upon receipt and the cells were incubated until they reached confluence. The cells were slow to reach confluence but with daily media changes, there seemed to be enough gaseous exchange and nutrients for the cells grow to confluence. The first passage typically saw the cells reluctant to come off the flask after trypsinisation. Firmly rapping the flask with the base of your palm should release the majority of the cells. We were not able to remove all cells from the flask.

Cells recovered from the T25 were split 1:2 and placed into two T75 flasks. The cells were recursively split 1:2 into T75 flasks once they had reached confluence until 8 T75 flasks were available for freezing. Seven confluent T75 flasks were frozen down and the final flask was maintained as a working culture. From this point, the working T75 was either split into T25s or kept as a T75 depending upon the number of cells required for experiments. In the early stages of this work, we performed 1:2 splits when passaging to keep the cell number up until growth had steadied. In this way, all frozen cells were at the same passage number (P53) and so all future work would begin at the same point in cell life.

The Claycomb protocol recommends freezing down four fully confluent T75s of HL-1 cells into cryovials. We recommend freezing down at least eight, as our

experience has shown the lifetime of the cells to be far less than reported. Maintaining more than eight T75 flasks at one time can become quite cumbersome, and so we felt this to be a good compromise between the number of frozen vials and the time taken to culture.

Freezing

- The entirety of one T75 flask was frozen into one cryovial as recommended in the Claycomb protocol.
- The T75 flask was rinsed with 5 mL PBS warmed to 37°C before aspiration of the PBS.
- Transfer 3 mL of 0.05% trypsin/EDTA to the flask.
- Incubate the flask at 37°C for 1 minute.
- Remove Trypsin/EDTA from the flask, and replace with 2-3 mL of fresh 0.05% trypsin/EDTA.
- Incubate at 37°C for 2-3 minutes.
- At this point the cells should come away from the flask by swirling the trypsin/EDTA around inside and gently tapping the flask on the base of your palm.
- Add equal amounts soybean trypsin inhibitor to the existing trypsin. Namely, 3 mL inhibitor for 3mL trypsin in the flask.
- Add 3 mL wash medium to the flask and ensure as many cells have dissociated from the flask as possible by washing the bottom of the flask with the pipette. Move the contents of the flask to a centrifuge tube. Note: up to 6 mL media can be added to the flask, but we typically added equal amounts with respect to the trypsin inhibitor. This guaranteed that the centrifuge tube was not overfilled, which would make it tedious to handle.
- Centrifuge at 500×g for 5 minutes.

- Remove wash medium by aspiration.
- Gently resuspend the pellet in 1.5 mL of freezing medium (95% FBS, 5% DMSO).
- Pipette resuspended cells into cryovial. Place the cryovial into a Nalgene freezing jar (which should contain fresh room temperature isopropanol).
- Place in -80°C freezer for 12-24 hours and then move to liquid nitrogen for long term storage.

A.4 End of life

An event unreported in the literature is the end of life signals for the HL-1 cells. In our experience, we found that the cells permanently changed their behaviour at passage 65-67. This period is easiest recognised by a sudden difficulty to remove cells from the tissue culture flask. In our experience, this lasted for about 4 passages before the cells once again became easy to dissociate. After this event, the cells are fundamentally altered in their function. There are three signs henceforth that warn of this: the development of vacuoles in the cells, a reduction in cell density, and sensitivity to certain chemicals.

We saw the cell population produce vacuoles in more cells at later passages (Figures A.1 and A.2). Overall, we also observed the culture morphology change to become less tightly packed. In general, this is a subjective indicator, so instead we suggest the careful monitoring of cell counts. A healthy culture would regularly produce between 8 and 12 million cells in a fully confluent T25 flask. Later passages (after approximately 65) would have noticeably lower cell counts. After the end of life event, the cells became sensitive to di-4-ANEPPS. Exposure to di-4-ANEPPS for any period of time would cause an immediate cessation of electrical activity in the culture. The culture would take 1-2 hours to recover but occasionally would not recover at all.

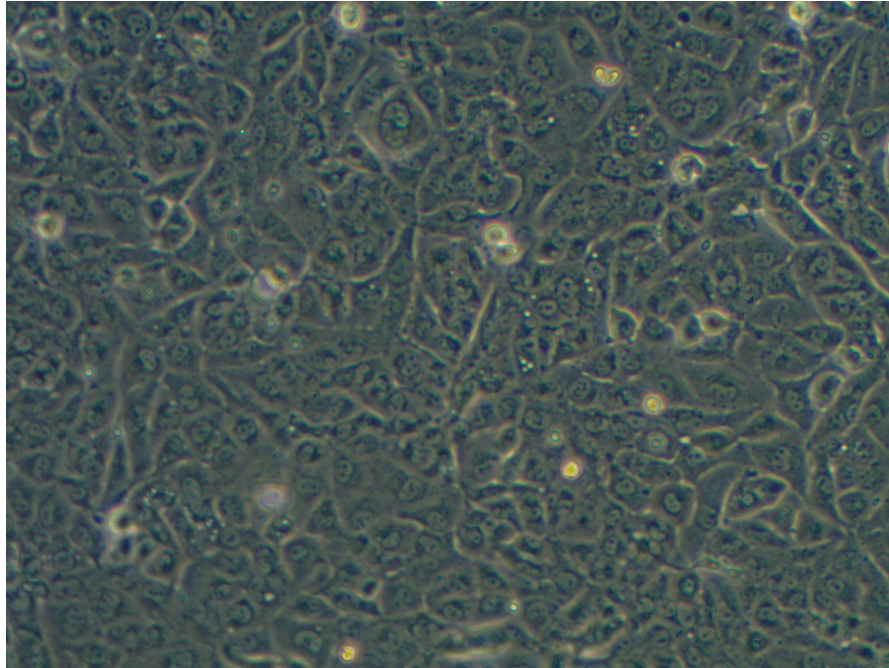


FIGURE A.1: Healthy HL-1 cells taken at passage 64 with a 10X objective and phase contrast.

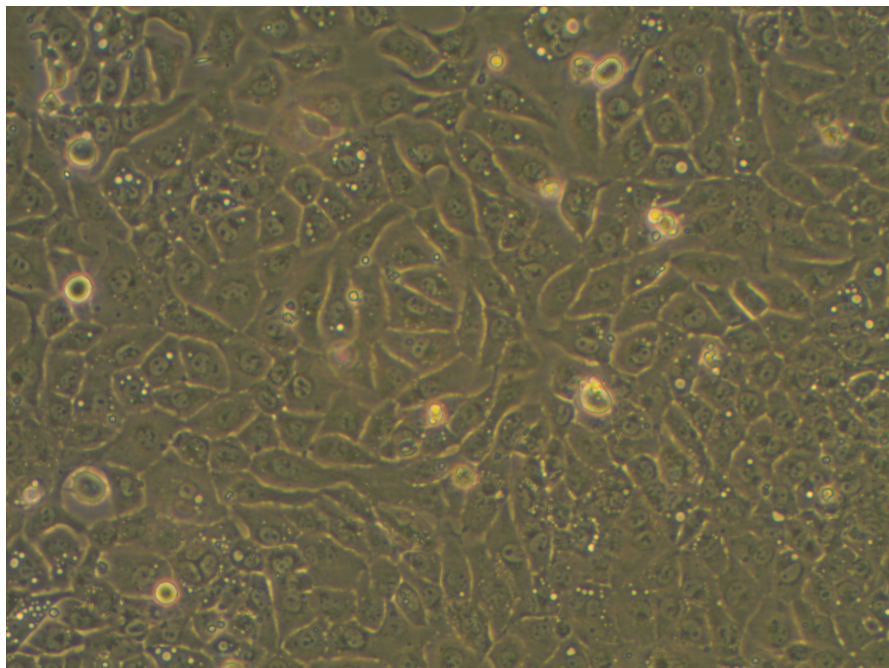


FIGURE A.2: Unhealthy HL-1 cells taken at passage 72 with a 10X objective and phase contrast.

If the researcher notices any of the aforementioned behaviours in their HL-1 cultures, it is strongly recommended that they dispose of their current batch and bring up fresh cells. It should be noted that we do not believe passage 65 to be the end of life for all HL-1 cultures; however, this was a consistent passage number for misbehaviour in our batch.

Bibliography

- Al Abed, A., Guo, T., Lovell, N. H., and Dokos, S. (2011). Tissue-based optimization of a sino-atrial node disc model. In *Engineering in Medicine and Biology Society, EMBC, 2011 Annual International Conference of the IEEE*, pages 1375–1378. IEEE.
- Al Abed, A., Guo, T., Lovell, N. H., and Dokos, S. (2013). Optimisation of ionic models to fit tissue action potentials: Application to 3d atrial modelling. *Computational and mathematical methods in medicine*, 2013.
- Aliev, R. R. and Panfilov, A. V. (1996). A simple two-variable model of cardiac excitation. *Chaos, Solitons & Fractals*, 7(3):293–301.
- Bachtel, A. D., Gray, R. A., Stohlman, J. M., Bourgeois, E. B., Pollard, A. E., and Rogers, J. M. (2011). A novel approach to dual excitation ratiometric optical mapping of cardiac action potentials with di-4-aneppts using pulsed led excitation. *Biomedical Engineering, IEEE Transactions on*, 58(7):2120–2126.
- Beeler, G. W. and Reuter, H. (1977). Reconstruction of the action potential of ventricular myocardial fibres. *The Journal of physiology*, 268(1):177–210.
- Bondarenko, V. E., Szigeti, G. P., Bett, G. C., Kim, S.-J., and Rasmusson, R. L. (2004). Computer model of action potential of mouse ventricular myocytes. *American Journal of Physiology-Heart and Circulatory Physiology*, 287(3):H1378–H1403.
- Boyett, M., Inada, S., Yoo, S., Li, J., Liu, J., Tellez, J., Greener, I., Honjo, H., Billeter, R., Lei, M., et al. (2006). Connexins in the sinoatrial and atrioventricular nodes.

- Brent, R. P. (2013). *Algorithms for minimization without derivatives*. Courier Dover Publications.
- Bueno-Orovio, A., Cherry, E. M., and Fenton, F. H. (2008). Minimal model for human ventricular action potentials in tissue. *Journal of Theoretical Biology*, 253(3):544–560.
- Burns, N. (2013). Cardiovascular physiology.
- Carmeliet, E. and Vereecke, J. (2002). *Cardiac cellular electrophysiology*, volume 9. Springer.
- Cherry, E. M. and Fenton, F. H. (2004). Suppression of alternans and conduction blocks despite steep apd restitution: electrotonic, memory, and conduction velocity restitution effects. *American Journal of Physiology-Heart and Circulatory Physiology*, 55(6):H2332.
- Claycomb, W., Lanson, N., Stallworth, B., Egeland, D., Delcarpio, J., Bahinski, A., and Izzo, N. (1998). H1-1 cells: a cardiac muscle cell line that contracts and retains phenotypic characteristics of the adult cardiomyocyte. *Proceedings of the National Academy of Sciences*, 95(6):2979–2984.
- Courtemanche, M., Ramirez, R. J., and Nattel, S. (1998). Ionic mechanisms underlying human atrial action potential properties: insights from a mathematical model. *American Journal of Physiology-Heart and Circulatory Physiology*, 44(1):H301.
- Cox, G. (2012). *Optical imaging techniques in cell biology*. CRC Press.
- DeMello, W. C. (1977). Electrical phenomena in the heart. *Journal of Clinical Engineering*, 2(1):86.
- Dhein, S. (2006). *Cardiovascular Gap Junctions*, volume 42. Karger Medical and Scientific Publishers.
- Dumas, J. and Knisley, S. (2005). Two-photon excitation of di-4-anepys for optical recording of action potentials in rabbit heart. *Annals of Biomedical Engineering*, 33:1802–1807. 10.1007/s10439-005-8466-9.

- Efimov, I. R., Nikolski, V. P., and Salama, G. (2004). Optical imaging of the heart. *Circulation Research*, 95(1):21–33.
- Elshrif, M. M. and Cherry, E. M. (2014). A quantitative comparison of the behavior of human ventricular cardiac electrophysiology models in tissue. *PloS one*, 9(1):e84401.
- Fenton, F. and Karma, A. (1998). Vortex dynamics in three-dimensional continuous myocardium with fiber rotation: filament instability and fibrillation. *Chaos*, 8(1):20–47.
- Fenton, F. H., Cherry, E. M., Hastings, H. M., and Evans, S. J. (2002). Multiple mechanisms of spiral wave breakup in a model of cardiac electrical activity. *Chaos: An Interdisciplinary Journal of Nonlinear Science*, 12(3):852–892.
- Fenton, H., Cherry, E., Ehrlich, J., Nattel, S., and Evans, S. (2004). A simulation study of atrial fibrillation initiation: Differences in resting membrane potential can produce spontaneous activations at the pulmonary vein-left atrial junction. *Heart Rhythm*, 1:S187–S188.
- FitzHugh, R. (1961). Impulses and physiological states in theoretical models of nerve membrane. *Biophysical journal*, 1(6):445–466.
- Fletcher, R. (2013). *Practical methods of optimization*. John Wiley & Sons.
- George, C., Higgs, G., and Lai, F. (2003). Ryanodine receptor mutations associated with stress-induced ventricular tachycardia mediate increased calcium release in stimulated cardiomyocytes. *Circulation research*, 93(6):531–540.
- Guo, T., Abed, A. A., Lovell, N. H., and Dokos, S. (2010). A generic ionic model of cardiac action potentials. In *Engineering in Medicine and Biology Society (EMBC), 2010 Annual International Conference of the IEEE*, pages 1465–1468. IEEE.
- Guo, T., Abed, A. A., Lovell, N. H., and Dokos, S. (2011). Parameter fitting using multiple datasets in cardiac action potential modeling. In *Engineering in*

- Medicine and Biology Society, EMBC, 2011 Annual International Conference of the IEEE*, pages 158–161.
- Guo, T., Al Abed, A., Lovell, N. H., and Dokos, S. (2013). Optimisation of a generic ionic model of cardiac myocyte electrical activity. *Computational and mathematical methods in medicine*, 2013.
- Hodgkin, A. L. and Huxley, A. F. (1952). A quantitative description of membrane current and its application to conduction and excitation in nerve. *The Journal of physiology*, 117(4):500.
- Hunter, P. J., Pullan, A. J., and Smaill, B. H. (2003). Modeling total heart function. *Annual review of biomedical engineering*, 5(1):147–177.
- Jalife, J., Delmar, M., Anumonwo, J., Berenfeld, O., and Kalifa, J. (2011). *Basic cardiac electrophysiology for the clinician*. John Wiley & Sons.
- Karma, A. (1993). Spiral breakup in model equations of action potential propagation in cardiac tissue. *Physical review letters*, 71:1103–1106.
- Knisley, S., Justice, R., Kong, W., and Johnson, P. (2000). Ratiometry of transmembrane voltage-sensitive fluorescent dye emission in hearts. *American Journal of Physiology-Heart and Circulatory Physiology*, 279(3):H1421–H1433.
- Lakowicz, J. R. (2007). *Principles of fluorescence spectroscopy*. Springer.
- Land, S., Niederer, S. A., Aronsen, J. M., Espe, E. K., Zhang, L., Louch, W. E., Sjaastad, I., Sejersted, O. M., and Smith, N. P. (2012). An analysis of deformation-dependent electromechanical coupling in the mouse heart. *The Journal of physiology*, 590(18):4553–4569.
- Laurita, K. R. and Singal, A. (2001). Mapping action potentials and calcium transients simultaneously from the intact heart. *American Journal of Physiology-Heart and Circulatory Physiology*, 280(5):H2053–H2060.
- Law, J., Yeung, C., Hofmann, B., Ingebrandt, S., Rudd, J., Offenhäusser, A., and Chan, M. (2009). The use of microelectrode array (mea) to study the

- protective effects of potassium channel openers on metabolically compromised hl-1 cardiomyocytes. *Physiological measurement*, 30(2):155.
- Li, L., Louch, W., Niederer, S., Andersson, K., Christensen, G., Sejersted, O., and Smith, N. (2011). Calcium dynamics in the ventricular myocytes of serca2 knockout mice: A modeling study. *Biophysical journal*, 100(2):322–331.
- Liang, R. (2013). Biomedical optical imaging technologies. *Biomedical Optical Imaging Technologies: Design and Applications, Biological and Medical Physics, Biomedical Engineering*. ISBN 978-3-642-28390-1. Springer-Verlag Berlin Heidelberg, 2013, 1.
- Lines, G. T. and Nielsen, B. F. (2007). *Computing the electrical activity in the heart*, volume 1. Springer.
- Loew, L., Cohen, L., Dix, J., Fluhler, E., Montana, V., Salama, G., and Jianyoung, W. (1992). A naphthyl analog of the aminostyryl pyridinium class of potentiometric membrane dyes shows consistent sensitivity in a variety of tissue, cell, and model membrane preparations. *Journal of Membrane Biology*, 130:1–10. 10.1007/BF00233734.
- Loew, L. M. (1996). Potentiometric dyes: Imaging electrical activity of cell membranes. *Pure and Applied Chemistry*, 68(7):1405–1409.
- Lovell, N. H., Cloherty, S. L., Celler, B. G., and Dokos, S. (2004). A gradient model of cardiac pacemaker myocytes. *Progress in Biophysics and Molecular Biology*, 85(2–3):301 – 323. Modelling Cellular and Tissue Function.
- Lucidi, S. (1988). New results on a class of exact augmented lagrangians. *Journal of Optimization Theory and Applications*, 58(2):259–282.
- Luo, C.-h. and Rudy, Y. (1991). A model of the ventricular cardiac action potential. depolarization, repolarization, and their interaction. *Circulation research*, 68(6):1501–1526.
- Mangoni, M. E., Traboulsie, A., Leoni, A.-L., Couette, B., Marger, L., Le Quang, K., Kupfer, E., Cohen-Solal, A., Vilar, J., Shin, H.-S., et al. (2006). Bradycardia

- and slowing of the atrioventricular conduction in mice lacking *cav3.1/α1g* t-type calcium channels. *Circulation research*, 98(11):1422–1430.
- McCulloch, A., Bassingthwaite, J., Hunter, P., Noble, D., Blundell, T., and Pawson, T. (1998). *Computational biology of the heart: from structure to function*. Elsevier Science.
- Montana, V., Farkas, D. L., and Loew, L. M. (1989). Dual-wavelength ratiometric fluorescence measurements of membrane potential. *Biochemistry*, 28(11):4536–4539.
- Nagumo, J., Arimoto, S., and Yoshizawa, S. (1962). An active pulse transmission line simulating nerve axon. *Proceedings of the IRE*, 50(10):2061–2070.
- Nattel, S. (2002). New ideas about atrial fibrillation 50 years on. *Nature*, 415(6868):219–226.
- Nattel, S. and Li, D. (2000). Ionic remodeling in the heart pathophysiological significance and new therapeutic opportunities for atrial fibrillation. *Circulation research*, 87(6):440–447.
- Netter, F. H. and Colacino, S. (1989). *Atlas of human anatomy*. Ciba-Geigy Corporation.
- Noble, D. (1962). A modification of the hodgkin—huxley equations applicable to purkinje fibre action and pacemaker potentials. *The Journal of Physiology*, 160(2):317–352.
- Noble, D. (1984). The surprising heart: a review of recent progress in cardiac electrophysiology. *The Journal of physiology*, 353:1.
- Pandit, S. V., Clark, R. B., Giles, W. R., and Demir, S. S. (2001). A mathematical model of action potential heterogeneity in adult rat left ventricular myocytes. *Biophysical Journal*, 81(6):3029–3051.
- Pandit, S. V. and Jalife, J. (2013). Rotors and the dynamics of cardiac fibrillation. *Circulation research*, 112(5):849–862.

- Podrid, P. J. and Kowey, P. R. (2001). *Cardiac arrhythmia: mechanisms, diagnosis, and management*. Lippincott Williams & Wilkins.
- Qu, Z., Garfinkel, A., Chen, P.-S., and Weiss, J. N. (2000). Mechanisms of discordant alternans and induction of reentry in simulated cardiac tissue. *Circulation*, 102(14):1664–1670.
- Rogers, J. M. and McCulloch, A. D. (1994). A collocation-galerkin finite element model of cardiac action potential propagation. *Biomedical Engineering, IEEE Transactions on*, 41(8):743–757.
- Rosenbaum, D. and Jalife, J. (2001). *Optical mapping of cardiac excitation and arrhythmias*. Wiley-Blackwell.
- Sartiani, L., Bochet, P., Cerbai, E., Mugelli, A., and Fischmeister, R. (2002). Functional expression of the hyperpolarization-activated, non-selective cation current if in immortalized hl-1 cardiomyocytes. *The Journal of physiology*, 545(1):81–92.
- Sato, S., Doi, S., and Nomura, T. (1994). Bonhoeffer-van der pol oscillator model of the sino-atrial node: a possible mechanism of heart rate regulation. *Methods of information in medicine*, 33(1):116.
- Shenasa, M., Hindricks, G., Borggrefe, M., and Breithardt, G. (2009). *Cardiac mapping*. John Wiley & Sons.
- Sigg, D. C., Iaizzo, P. A., Xiao, Y.-F., and He, B. (2010). *Cardiac electrophysiology methods and models*. Springer.
- Smaill, B. H., Zhao, J., and Trew, M. L. (2013). Three-dimensional impulse propagation in myocardium arrhythmogenic mechanisms at the tissue level. *Circulation research*, 112(5):834–848.
- Sperelakis, N., Kurachi, Y., Terzic, A., and Cohen, M. V. (2000). *Heart physiology and pathophysiology*. Academic Press.
- Spitzer, V. M. and Whitlock, D. G. (1998). The visible human dataset: the anatomical platform for human simulation. *The anatomical record*, 253(2):49–57.

- Tranquillo, J. V., Hlavacek, J., and Henriquez, C. S. (2005). An integrative model of mouse cardiac electrophysiology from cell to torso. *Europace*, 7(s2):S56–S70.
- Umapathy, K., Masse, S., Kolodziejaska, K., Veenhuyzen, G. D., Chauhan, V. S., Husain, M., Farid, T., Downar, E., Sevaptsidis, E., and Nanthakumar, K. (2008). Electrogram fractionation in murine hl-1 atrial monolayer model. *Heart Rhythm*, 5(7):1029–1035.
- Van Capelle, F. and Durrer, D. (1980). Computer simulation of arrhythmias in a network of coupled excitable elements. *Circulation research*, 47(3):454–466.
- van Rijen, H., Van Veen, T., Gros, D., Wilders, R., and De Bakker, J. (2006). Connexins and cardiac arrhythmias.
- Weiss, J. N., Chen, P.-S., Qu, Z., Karagueuzian, H. S., and Garfinkel, A. (2000). Ventricular fibrillation how do we stop the waves from breaking? *Circulation Research*, 87(12):1103–1107.
- White, S., Constantin, P., and Claycomb, W. (2004). Cardiac physiology at the cellular level: use of cultured hl-1 cardiomyocytes for studies of cardiac muscle cell structure and function. *American Journal of Physiology-Heart and Circulatory Physiology*, 286(3):H823–H829.
- Williams, D. A., Bowser, D. N., and Petrou, S. (1999). Confocal ca²⁺ imaging of organelles, cells, tissues and organs. In Conn, P. M., editor, *Confocal Microscopy*, volume 307 of *Methods in Enzymology*, pages 441 – 469. Academic Press.
- Windhorst, U. and Johansson, H. (1999). *Modern Techniques in Neuroscience Research*. Springer.
- Xie, F., Qu, Z., Garfinkel, A., and Weiss, J. N. (2002). Electrical refractory period restitution and spiral wave reentry in simulated cardiac tissue. *American Journal of Physiology-Heart and Circulatory Physiology*, 283(1):H448–H460.
- Yang, Z. and Murray, K. (2011). Ionic mechanisms of pacemaker activity in spontaneously-contracting atrial hl-1 cells. *Journal of cardiovascular pharmacology*, 57(1):28.

- Yang, Z., Shen, W., Rottman, J. N., Wikswo, J. P., and Murray, K. T. (2005). Rapid stimulation causes electrical remodeling in cultured atrial myocytes. *Journal of molecular and cellular cardiology*, 38(2):299–308.
- Zecevic, D. and Canepari, M. (2010). *Membrane potential imaging in the nervous system: methods and applications*. Springer.
- Zhang, H., Holden, A. V., Kodama, I., Honjo, H., Lei, M., Varghese, T., and Boyett, M. R. (2000). Mathematical models of action potentials in the periphery and center of the rabbit sinoatrial node. *American Journal of Physiology - Heart and Circulatory Physiology*, 279(1):H397–H421.